Characterization and passive control of the wake behind a square-back Ahmed body at yaw

By

Adriaan Booysen

A thesis submitted in partial fulfillment of the requirements for the degree of

Master of Science

Department of Mechanical Engineering

University of Alberta

Abstract

The near wake behind the Ahmed body at zero-yaw has been extensively studied in the past, but comparatively little is known about the changes in the wake flow patterns during crossflow. Measurements of the near wake of a square-back Ahmed body were obtained at a Reynolds Number of $Re_H = 9.2\times10^4$ for three yaw angles of β = 0°, 5°, and 10° using large-scale volumetric particle tracking velocimetry within a 350 mm × 300 mm × 180 mm volume that utilizes an innovative helium-filled soap bubble seeding system. The helium-filled bubble system integrated 48 nozzles into a streamlined, modular housing structure that was located before the wind tunnel contraction. It successfully maintained a seeding density of 0.02 particles per pixel at a 10 m/s freestream velocity which was critical to the measurement quality.

With increasing yaw angle, the recirculating region on the leeward side grew in strength, shifting the separation bubble towards the windward side. The downwash motion from the top-edge and the spanwise motion from the leeward edge of rear-face also strengthened. Time-averaged vortex structures were identified within the mean flow showing a vortex ring that forms tangent to the separation bubble. At yaw, the vortex ring became skewed and four additional streamwise vortex structures developed. Spectral analysis showed that the overall energy of oscillations increased with yaw while the Strouhal numbers of the spanwise and wall-normal flow motions remained the same. The majority of the energy within the yawed wakes was found on the windward side of the wake. Proper orthogonal decomposition of the velocity field showed that the first spatial mode contained 32.8% of the total kinetic energy for the zero-yaw case, while the energy reduced to approximately 10% for the β = 5° and 10° wakes. The large drop in energy within the yawed wake first modes implied the suppression of the bi-stability phenomenon at these yaw angles.

A supplementary study measured the aerodynamic loads acting on the same square-back Ahmed body geometry at a higher Reynolds number of $Re_H = 2.7\times10^5$ across a yaw range of $-12.5° \leq \beta \leq 12.5°$. The aerodynamics loads were analyzed to assess the effect of yaw. As yaw increased it was shown that the drag forces, side forces, roll moments, and yaw moments all increased. The latter three all had an approximately linear anti-symmetric distribution about zero-yaw. The increase in drag was attributed to an induced drag term which was found to be proportional to the side force. The force and moment components of the baseline case were also compared to those of four different geometry modifications, with the goal being drag reduction and reduced aerodynamic loading. The four geometries were a boat tail consisting of four inclined panels at the rear edges, a vertical splitter plate centered on the rear face, cylindrical protrusions on the side edges of the rear face, and a dual fan configuration with downward facing fans positioned at the top two corners. The boat tail was the most effective geometry modification. It resulted in a drag reduction of 26.8% and a side force reduction of 12.3%. The boat tail did however also correspond to the largest increase in yaw moment (41.7%).

Preface

This thesis is an original work by Adriaan Booysen. Some figures in Chapter 2 have been previously published but are shared with permission, either through open access rights or with the publishing permissions provided in Appendix A. No other parts of this thesis have been previously published. The collection of all of the data presented within this thesis along with the corresponding analysis was primarily completed by Adriaan Booysen. Assistance was provided when required, during the data collection and data analysis stages, by members of the Author's research group. Some of the MATLAB code used for the data analysis was based on code provided by members of the Author's research group.

The contents of Chapter 4 have been submitted to be published but a decision regarding its acceptance has not been reached yet.

Acknowledgements

The research that comprises this thesis was only made possible by the support of many individuals. First, I would like to thank Professor Sina Ghaemi for taking me on as a student and extending himself by allowing me to choose a project related to my personal interests. His guidance and support was fundamental to the growth experienced during the time that underlies this thesis. Thanks are also due to Prashant Das who was always willing to go out of his way to lend advice and entertain unorthodox ideas. Lastly, thanks to Sen Wang who gave up a large amount of his time to make a success out of a very challenging measurement campaign.

Thanks also needs to be given to family and friends who supported me in my pursuits along the way. Without them, this research would have been much less successful and quite possibly would not have happened.

Table of Contents

List of Figures

List of Tables

Nomenclature

Symbol	Definition
$\langle ... \rangle$	Time-averaged quantity of enclosed parameter
Re	Reynolds number
St	Strouhal number
u	Fluctuating streamwise velocity component
v	Fluctuating spanwise velocity component
w	Fluctuating wall-normal velocity component
U	Instantaneous streamwise velocity component
V	Instantaneous spanwise velocity component
W	Instantaneous wall-normal velocity component
x	Streamwise axis
y	Spanwise axis
z	Wall-normal axis
C_d	Coefficient of drag
C_{Bx}	Streamwise body-indexed force coefficient
C_{By}	Spanwise body-indexed force coefficient
C_{MBx}	Streamwise body-indexed moment coefficient
C_{MBy}	Spanwise body-indexed moment coefficient
C_{MBz}	Wall-normal body-indexed moment coefficient
C_{Wx}	Streamwise wind-indexed force coefficient
C_{Wy}	Spanwise wind-indexed force coefficient
C_{MWx}	Streamwise wind-indexed moment coefficient
C_{MWy}	Spanwise wind-indexed moment coefficient
C_{MWz}	Wall-normal wind-indexed moment coefficient
β	Yaw angle
U_∞	Freestream speed
f	Focal Length

ρ	Density
F_B	Body-indexed force components
F_C	System correction force components
F_L	Load cell measured force components
F_W	Wind-indexed force components
M_B	Body-indexed moment components
M_C	System correction moment components
M_L	Load cell measured moment components
M_W	Wind-indexed moment components
H	Body Height
W	Body Width
L	Body Length
A	Frontal Area
L_V	Load cell origin to coordinate system origin vertical distance
RV	Ring Vortex
SV	Streamwise Vortex

Chapter 1: Introduction

1.1 Motivation

The aerodynamic performance of a motor vehicle is a central factor in its ability to meet modern safety and efficiency requirements. Recent emissions regulations as well as proposed emission outlooks (Rules and Regulations 2012) are pressuring manufacturers to focus on the aerodynamic efficiency of vehicles since aerodynamic drag is a primary source of inefficiency. Automotive bodies are generally bluff bodies that share the aerodynamic characteristics of large, separated wakes that generate significant pressure drag. The pressure drag has been found to account for up to 90% of automotive body drag for some vehicle geometries (National Research Council Canada 2012). Focusing on the vehicle wake, its topology, and the mechanisms that exacerbate the corresponding pressure differentials therefore becomes the first steps in minimizing drag. Fully defining the wake topology sets the foundation for identifying the primary drag inducing mechanisms and forming the subsequent strategies to reduce the effect of pressure drag.

The progression of characterizing the topology of a vehicle's wake is doing so at non-ideal wind angles. Atmospheric winds and crossflows are a reality for real-world driving. Therefore, the aerodynamic characteristics of vehicles may not be properly assessed or optimized within the design window of zero-yaw conditions. The understanding of the wake topology within crosswind conditions and how it changes with varying crosswind angles becomes arguably as important as the zero-yaw understanding in the context of real-world aerodynamic efficiency.

Another critical aspect of a vehicle's aerodynamic performance is the distribution of aerodynamic forces and moments and the corresponding impact on vehicle handling and stability. Crosswinds introduce forces that are not aligned with the vehicle's direction of travel and complex loading of suspension and handling components can follow, leading to safety concerns if they are not properly understood and integrated into the vehicle dynamics systems. A wholistic understanding of the wake topology at yaw along with the resulting aerodynamic forces then

becomes the best-case scenario for improving both aerodynamic efficiency and aerodynamic stability.

1.2 Thesis Outline

To effectively study the wake topology and resulting aerodynamic forces of an automotive body at yaw, a representative aerodynamic research model will be used as the subject of this thesis. This thesis will first summarize the findings of relevant automotive aerodynamic research in Chapter 2: Literature Review. The literature review covers research related to square and flat backed automotive bodies at various degrees of yaw, followed by the current understanding of the corresponding aerodynamic forces and their control. The theory underlying several measurement and data analysis techniques are also summarized.

The experimental setup and data collection methods will be discussed in detail in Chapter 3. Descriptions are given for the 2D-PIV, 3D-PTV, and load measurements that were completed for this thesis.

Chapter 4 characterizes the wake for the square-back Ahmed body, comparing results at zero-yaw with two yawed cases. The time-averaged wake topologies are discussed along with some temporal characteristics.

Chapter 5 will investigate the resulting aerodynamic forces for the square-back Ahmed body at yaw. Four separate geometry modifications will also be evaluated in terms of force and moment reduction at yaw. The geometry modifications consist of a boat tail, a vertical splitter, cylinder rakes, and dual fans and are all attached to the rear face of the Ahmed body.

Finally, Chapter 6 contains conclusions for both Chapters 4 and 5 as well as some discussion of future research possibilities.

Chapter 2: Background

Chapter 2 will first review the current literature focusing on automotive bluff body model aerodynamics. The various bluff body models that exist within automotive aerodynamics research are introduced. The research findings regarding the mean flow characteristics of simplified flat backed bluff bodies at zero-yaw and yawed flows are then summarized. Current research regarding the spectral properties of these flows as well as the results of several proper orthogonal decomposition (POD) analyses of the wake are reviewed. Finally, the current understanding of the aerodynamic forces and moments acting on these bodies at various yaw angles are summarized, including the effects of geometry changes and passive flow control devices.

The remainder of Chapter 2 will focus on the background theory of the measurement and analysis techniques used within this thesis. First the principals of particle image velocimetry (PIV) and 3D particle tracking velocimetry (3D PTV) are discussed. The theory and procedures for vortex filament identification, Q-criterion, power spectral density analysis, and POD follows.

2.1 Automotive Bluff Bodies

The selection of an appropriate model sets the basis for researching the fundamental aerodynamic performance of vehicles. Several bluff bodies have been created with the purpose of representing automotive flows at a fundamental level. The level of detail included in the models have varied over time but two primary groups have emerged: simple bluff bodies and more detailed vehicle models (Le Good et al. 2004). Selection of the appropriate model is dependent on many factors, but the degree of model detail is usually inversely related to the generality of the results. Increasing the model detail to more closely mimic actual road vehicles improves the correlation and transferability of the results but decreases the breadth of vehicle geometries that observations are applicable to. Simplified bluff bodies are more common in academic research for these reasons, since the fundamental flow physics are the primary concern and unnecessary details can interfere with observations. The complex flow fields have also proven useful in secondary applications

where these bluff bodies have been used as reference models in computational studies or as correlation models to compare and adjust experimental results across wind tunnel facilities.

Several simplified bluff bodies have been devised, consisting of block-shaped bodies with variable traits that allow for the modeling of basic automotive configurations (Le Good et al. 2004). The simplifications remove features such as front apertures, HVAC systems, and wheels. The Ahmed body was one of the first models conceived for studying automotive aerodynamics, proposed by Ahmed et al. (1984). It consists of a large frontal area to displace the flow, a long mid-section to allow any separated flow to reattach, and bluff afterbody which creates a large and defined wake. The body sits on four posts lifting it off the ground to approximate the influence of the tires and the vehicle's proximity to the roadway. A slant is included at the top rear section of the body with a variable decline angle in order to replicate the flow over multiple configurations. This rear decline is commonly referred to as the backlight. The Ahmed body slant or backlight angle ranges from 0° to 40° and the aspect ratio of the slanted section is kept constant. When this angle is set to 0°, the model becomes what is known as the square-back variant of the Ahmed body, approximating the flow over boxier, square-backed vehicles such as transport trucks and delivery vehicles.

Another commonly used fundamental model is the Windsor model (also named the Rover model) (Le Good et al. 2004; Howell et al. 2008) which differs from the Ahmed body with the inclusion of large sloped forebody. The sloped front is meant to better reproduce the flow around vehicles with inclined leading edges. The rear section also has a fixed aspect ratio backlight with the angle again ranging between 0° to 40°. Slight variations to these two bodies also exist as the NRCC/SAE model, the Davis Model, and the Docton model as well as in automotive manufacturer bluff models used by Ford, GM, and Chrysler (Le Good et al. 2004). More recently, a new model was introduced, named the Willy model; it was conceived to better suit studies focusing on unsteady flows and yawed flows over bluff body geometries (Chometon et al. 2005). The body holds no pronounced edges aside from those forming the flat rear face. This unique feature removes fixed separation points along the midsection of the body. The square-back Ahmed body, Windsor body, and Willy body models can be seen in Figure 1 to give insight into the general features of these aerodynamic models. The front sides of the bodies are facing towards the lower left corner. Figure 1(a) also shows the body axes along which the body length (L), width (W), and height (H) are measured.

More detailed reference models also exist and have been used to varying degrees in academic and industrial research. These models include the Motor Industry Research Association (MIRA) reference car, several manufacturer models, and recently the DrivAer model (Le Good et al. 2004; Heft et al. 2012). These models will however be disregarded for the purposes of this thesis as the focus will be on more fundamental aspects of automotive and bluff body flow physics. The following sections will focus primarily on square-backed iterations of simple bluff bodies to allow for a comprehensive review of current literature.

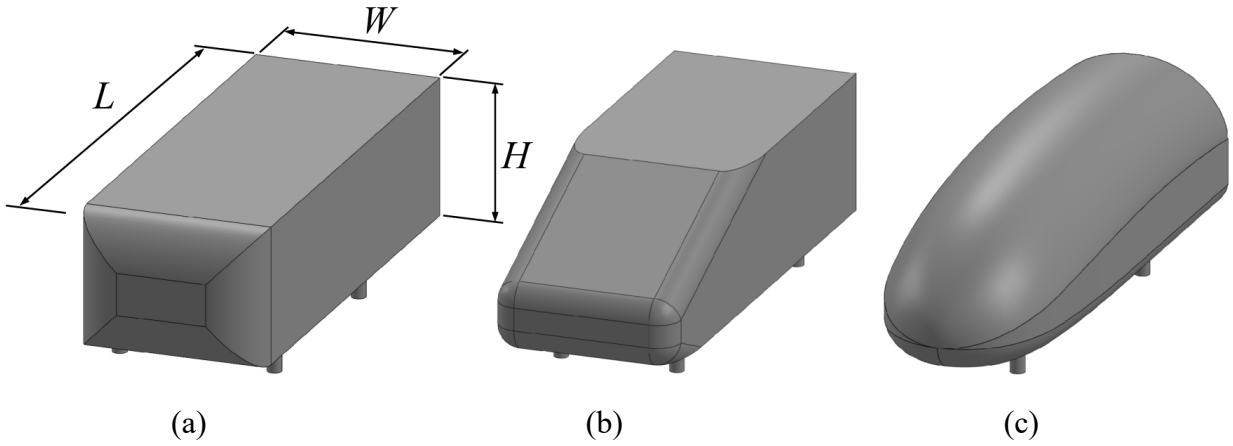

Figure 1: Illustrations of three different simplified automotive aerodynamic models: the (a) square-back Ahmed body, (b) Windsor body, and (c) Willy body models.

2.2 The Zero-Yaw Wake Topology

2.2.1 Time-Averaged Wake Features

Seminal automotive bluff body research was carried out by Ahmed et al. (1984) with the introduction of the Ahmed body and the corresponding investigation into the zero-yaw time-averaged wake. The yaw angle is defined by rotation of the body from the flow aligned state, along a plane that is parallel to the length and width of the body. The zero-yaw condition therefore refers to the case where the body's length is aligned with the direction of airflow. Their research of this geometry mostly involved the slanted backlight configurations; the backlight referring to a sloped

top rear face which had the angle of the slope (slant angle) varied to form different configurations. Some common trends for the body shape were however still identified. Using experimental force and pressure measurements along the body surface at a height-based Reynolds number of $Re_H = 4.3\times10^6$. The Reynolds number is defined as $Re = \rho UH/\mu$, where ρ is the density, U is the flow speed, H is the body height (characteristic length), and μ is the dynamic viscosity. They found that the pressure drag from the rearward facing surfaces made the greatest contribution to total body drag. The drag from the forward-facing section also remained constant across multiple rear slant configurations leading to the conclusion that direct interaction between the forebody and afterbody flow was minimal. The measured drag coefficient for the square-back configuration was $C_D = 0.25$ wherefrom the drag reduced with backlight angle until an inflection point was reached at a slant angle of 12.5°. The square-back drag coefficient was surpassed when the backlight angle was greater than 20°.

Duell et al. (1999) carried out a study focusing solely on a geometry that closely resembled the square-back Ahmed body. Using anemometers at $Re_L = 7.5\times10^5$, they found that the wake mean-flow topology consisted of a large separated region that formed behind the rear face. Within the wake, two large recirculating vortices were also identified along the body width midplane. The recirculating vortices were later identified within both body symmetry planes which suggested the existence of a large recirculating vortex ring that formed behind the rear face (Khalighi et al. 2001; 2012; Krajnović et al. 2003; Grandemange et al. 2013b). Experimental and numerical studies by Khalighi et al. (2001) further analyzed the wake of a square-backed bluff body geometry at $Re_H = 1.7\times10^5$, adding that the time-averaged recirculating region was symmetric across the spanwise plane but slightly asymmetric across the wall-normal plane due the vicinity of the ground plane. The length of the separation bubble was measured to be $x/H = 1.6$ relative to the rear face. Recent studies have measured values closer to $x/H = 1.5$ (Grandemange et al. 2013b; Volpe et al. 2015; Lorite-Díez et al. 2020). Reynolds stresses were also measured and found to be largest at the edges of the rear face, consistent with the shear layers that formed within the wake. A pair of counter rotating streamwise vortices were identified downstream of the separation bubble by Krajnović et al. (2003) with large-eddy simulations (LES) at $Re_H = 2.1\times10^5$. They were distributed symmetrically across the span and their rotation advected flow downwards along the vertical symmetry plane.

An investigation by Grandemange et al. (2013b) measured velocity, force, and pressure to in the wake of a square-back Ahmed body at $Re_H = 9.2\times10^4$ and found that the flow separates at the leading edge of the body, reattaches along the mid-section and then becomes fully turbulent before reaching the rear face. Figure 2 shows the time-averaged results based on the PIV measurements from the Grandemange et al. (2013b) investigation. All values within Figure 2 that are marked with an asterisk are non-dimensionalized quantities based on the body base height H, the freestream velocity U_∞, and the density ρ. Figure 2(a) shows the velocity field along the body's spanwise mid-plane with overlayed streamlines. The leading-edge separation and time-averaged recirculation bubble are evident within the streamlines. Figure 2(b) shows the near wake streamwise velocity field at $z^* = 0.6$ which shows the lateral symmetry of the recirculation bubble. Lastly, Figure 2(c) and (d) show the velocity field along planes at $x^* = 1, 2$ respectively. Figure 2(a) and (b) are oriented with flow from the left to the right. Figure 2(c) and (d) show upstream perspectives of the wake.

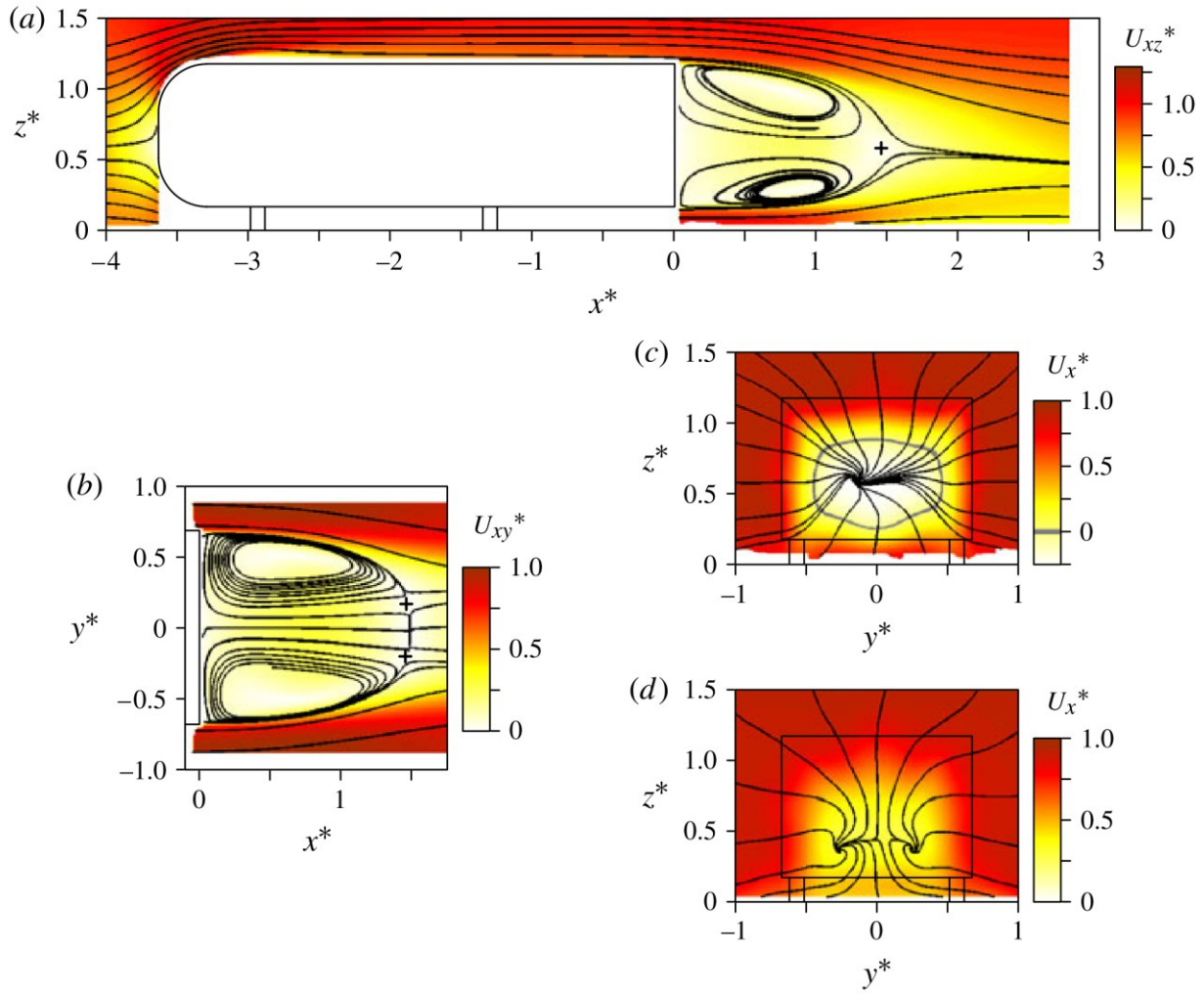

Figure 2: Time-averaged velocity measurments of the square-back Ahmed body flow field along (a) the lateral symmetry plane of the body, (b) the body height symmetry plane in the near wake, and two stream-normal planes at (c) $x^* = 1$ and (d) $x^* = 2$ (Grandemange et al. (2013b).

2.2.2 Instabilities within the Zero-Yaw Wake

These time-averaged wake descriptions were thought to fully describe the general topological features of flat backed bluff body geometries until the research by Grandemange et al. (2012; 2013b) significantly advanced the understanding by finding evidence of a symmetry breaking, bi-stability phenomenon within the instantaneous flow field. Grandemange et al. (2013b) measured velocity, force, and pressure in the wake of a square-back Ahmed body at $Re_H = 9.2\times10^4$ and found that the bi-stability phenomenon consisted of two equiprobable states that imposed an

asymmetric recirculation pattern across the span of the near wake. These two states switched randomly with the average characteristic time period of the switches being $T_S U_\infty / H = 1500$. This was three orders of magnitude larger than the characteristic time period of the flow. The switching frequency was also found to increase as the freestream velocity increased. This instability meant that the toric recirculation description of the wake became purely a time-averaged feature. The bi-stable phase-averaged topology of the wake was therefore, a more accurate description of the wake structure. Asymmetric shifts in the base pressure distribution and Reynolds stresses were also observed, following the shifts in phase (Grandemange et al. 2013b; Volpe et al. 2015).

Figure 3 contains research by Volpe et al. (2015) showing the effect of the bi-stability phenomenon on the wake structure with phase averaged measurements of the wake velocity along a spanwise plane. Figure 3(a)-(d) all show the coefficient of pressure (C_p) distributions on the rear face along with normalized mean streamwise velocity contours (V/ V_∞) with overlayed 2D streamlines. The top edge of all the velocity plots coincides with the rear face of the Ahmed body and flow direction is from top to bottom. Figure 3(a) and (d) show canonically averaged and phase averaged distributions, respectively. Figure 3(b) and (c) show the conditionally averaged bi-stable phase distributions demonstrating the spanwise asymmetry caused by the bi-stability.

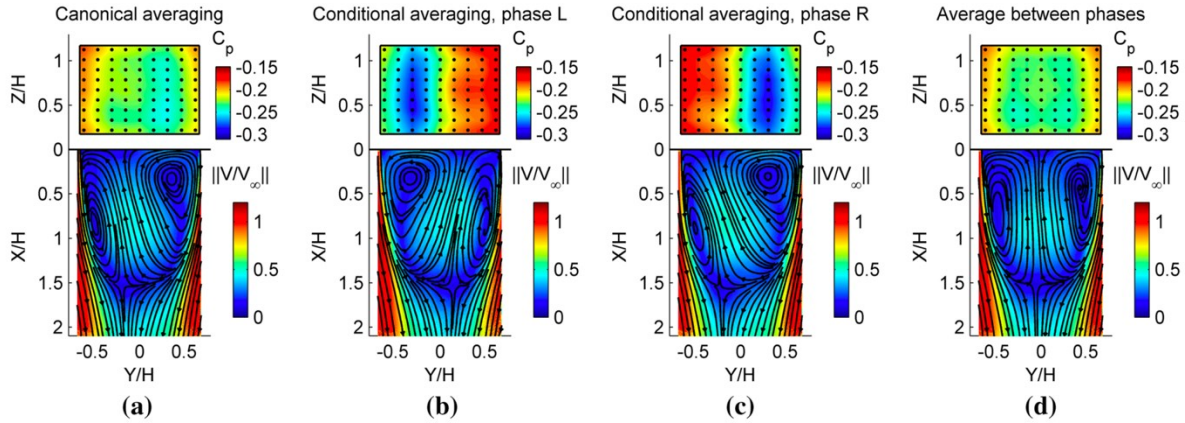

Figure 3: Rear base pressure measurements and mid-height velocity measurements for a square-back Ahmed body based on (a) the canonical average of measurements, (b) the conditionally averaged L phase, (c) the conditionally averaged R phase, and (d) the phase averaged wake (Volpe et al. 2015).

Grandemange et al. (2013b) also analyzed the effects of ground clearance, *C,* on the bi-stability phenomenon. The ground clearance is the distance between the bottom face of the body and the ground plane. By varying the ground clearance of the body they found that the bi-stability was suppressed for clearances below $C/H = 0.07$, a small transition phase was observed across the ground clearance range of $0.07 < C/H < 0.10$, and then a fully bi-stable wake was observed when $C/H > 0.10$. Grandemange et al. (2013a), experimentally explored the effects of body aspect ratio and ground clearance on the instabilities within the wake of a body similar to the square-back Ahmed body at $Re_W = 4.5\times10^4$. Using 2D PIV and pressure measurements on the rear face, they were able to identify instabilities along both the spanwise and wall-normal axes. The spanwise instabilities, which included the bi-stability phenomenon for the base Ahmed body geometry, were present within the wake at aspect ratios of $0.60 < H/W < 1.30$ and ground clearances of $C/W > 0.08$. A secondary spanwise instability range also existed when the aspect ratio was $0.30 < H/W < 0.65$ and ground clearance was $C/W < 0.03$. At intermediate ground clearances, velocity measurements showed that the separation bubble was still connected to the ground plane but the ground boundary layer detached in certain locations, introducing a stabilizing effect into the wake. The wall-normal instabilities were found to fall within an aspect ratio range of $0.77 < H/W < 1.67$ and ground clearances of $C/W > 0.08$. All base instabilities were bi-modal but an interfering range did exist where either instability could exist. The vertical instabilities were comprised of two non-symmetric states since the geometry was non-symmetric along this axis. The results of this study can be seen in Figure 4 where the instability regions are shown with respect to the body-width normalized aspect ratio ($H^* = H/W$) and ground clearance ($C^* = C/W$). The *y*-instability domains (D_y) and *z*-instability domains (D_z) are defined with respect to two aspect ratios, H_1^* and H_2^*.

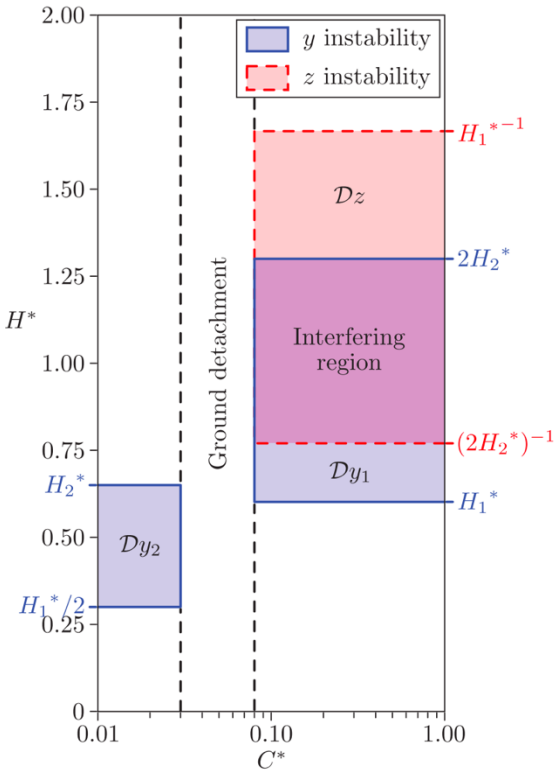

Figure 4: Zones of instability within the wake of the square-back Ahmed body based on variations of normalized body aspect ratio and normalized ground clearance (Grandemange et al. (2013a).

A third study by Grandemange et al. (2014) studied the influence of wake disturbances on the instabilities by sweeping small vertical and horizontal control cylinders throughout the wake. The effects were quantified using pressure and PIV measurements in the wake of a standard square-back Ahmed body at $Re_H = 9.2\times10^4$. It was found that positioning a small cylinder in a vertical orientation along the vertical symmetry plane resulted in the symmetrization of the wake, meaning the bi-stability phenomenon was suppressed. Positioning this cylinder in other locations resulted in an asymmetric geometry across the span and a consequent locking of the wake into one of the bi-stable modes. A horizontal cylinder orientation only suppressed the bi-stability phenomenon when placed in the upper or lower shear layer, forming a symmetric wake. Other positions for this disturbance maintained a symmetric geometry across the span and therefore had no effect on the spanwise bi-stability.

A study by Cadot et al. (2015) looked at the effects of ground clearance as they related to the flow Reynolds number. Using hot wire anemometer measurements within the gap between the body and the ground plane, they discovered that the critical ground clearance for the bifurcation

point, the point at which wake transitioned to the bi-stable state, occurred when the flow underneath the body reached a velocity peak equal to the freestream velocity. Volpe et al. (2015) focused on the statistics of the bi-stability using experimental measurements at $Re_H = 5.1\times10^5$. By conditionally averaging the base pressure measurements they were able to identify the two bi-stable states. These were then used to further characterize the switching. They found that they were able to model the random distribution of the bi-stability phase duration using a Markov chain distribution. They also attempted to confirm the mean duration period of the bi-stability suggested by Grandemange et al. (2013b) but found that the duration is actually much shorter ($T_S U_\infty/H$ = 421). The discrepancy was contributed to the use of a sampling frequency by the prior study that was not high enough to capture short phase durations. Lastly, they looked at the instability's sensitivity to yaw and found that at yaw angles of $|\beta| > 0.2°$, there was a clear predominance to one bi-modal state although both were still observed. At yaw angles of $|\beta| > 1°$, the bi-stability became fully suppressed. Within the yaw range of $|\beta| < 1°$, the topology of the two bi-stable states remained generally consistent, independent of the mode dominance. A study by Grandemange et al. (2015) was also able to verify the $|\beta| > 1°$ sensitivity limit within the wake of an industrial scale square back Ahmed body model at $Re_H = 2.5\times10^6$. Bonnavion et al. (2018) investigated the bi-stability's sensitivity to pitch angle and found that it was only present within the pitch angle range of $-0.75° < \alpha < 5°$.

The use of geometry modifications to influence the square-back body instabilities has also been investigated. Evrard et al. (2016) added a rear base cavity to square-back Ahmed body model with a different H to W aspect ratio at $Re_H = 4\times10^5$. They were able to suppress the bi-stability phenomenon when the cavity depth (d) surpassed $d/H = 0.25$. A sufficiently deep cavity was able to symmetrize the wake, producing an instantaneous wake structure similar to that of the time-averaged symmetric recirculation pattern discussed in Section 2.2.1. Perry et al. (2016) studied the effects of tapering the top and bottom edges of a square-backed Windsor body at $Re_H = 7.7\times10^5$. They found that the top and bottom tapers increased downwash and upwash respectively, which consequently weakened the bi-stability phenomenon. The weakening materialized in two forms, the first being a smaller bi-stable region since the distance between the top and bottom shear layers was reduced, and the second being an increased average phase duration.

2.2.3 Vortex Structures within the Zero-Yaw Wake

The descriptions of the time-averaged wake showed evidence of a toric vortex structure present within the recirculation bubble, defined by the recirculating vortices within it. These recirculating vortices are clearly identifiable in Figure 2(a) and (b). With the discovery of the wake instability, the time-averaged flow features, including the vortex structure identified so far, were no longer representative of the wake. Dominant recirculating vortices were still, however, identifiable within the phase averaged wake, making their 3D extensions a subject of interest. Figure 3(b) and (c) provide good visual representation of these recirculating vortices within the two phase-averaged wake modes of a square-back Ahmed body. Using a simulation based on lattice-Boltzmann method (LBM) over one bi-stability period at $Re_H = 3.96\times10^5$, Lucas et al. (2017) identified a skewed torus with one lateral side skewed upstream towards the rear face of the Ahmed body. The short duration of this simulation provided insight into the structure of the vortex when it was not influenced by the time-averaging of several bi-stability periods. Further support for this description came from large eddy simulation (LES) of a square-back Ahmed body at $Re_H = 3.3\times10^4$ by Longa et al. (2019). Instantaneous contours of pressure showed the core of a phase-dependent, tilted toroidal structure similar to Lucas et al. (2017). Large hairpin vortices were shed from the downstream tilted side of the toroidal structure. It was suggested that a large enough hairpin vortex being shed could destabilize the toroidal structure and cause the switching between the bi-stability modes.

Other studies on various square-back bodies have however, suggested an alternative interpretation in which the topology within the instantaneous wake resembles hairpin vortices (Evrard et al. 2016; Perry et al. 2016; Pavia et al. 2018; 2020; Fan et al. 2020). Evrard et al. (2016) first suggested that the phase averaged wake structure behind a square-backed Windsor body consisted of a horseshoe vortex system. Using 2D streamlines from planar PIV measurements, an extrapolation was made on the vortex structure based on the recirculating regions in the streamlines. It was proposed that the wake contained a single horseshoe vortex where the head was aligned along one side of the body and the legs advected partially across the rear face before turning downstream. Perry et al. (2016) expanded on this description using 2D streamlines on off-symmetry planes and added a second C-shaped vortex core to the model. The second vortex passed through the dominant spanwise recirculating region previously identified closer to the rear face

with the two legs stretching directly downstream. The horseshoe vortex was situated on the opposite side and passed through the remaining recirculating regions. This description better accounted for all of the 2D recirculating regions identified within the wake. Recently, a study of the square-back Windsor model wake by Pavia et al. (2018) proposed the most up to date description of this vortex structure. This model consists of a hairpin vortex that is oriented along one side of the rear face with legs that traverse across the wake to the opposite side. Once the legs reach the opposite side, the top leg bends and stretches downstream while the lower leg extends up along the spanwise edge and then merges with the top leg. The spatial description would be valid for the wake description in one bi-stable state and would flip across the vertical symmetry plane when the bi-stability switched. Figure 5 shows a sketch of the proposed vortex from Pavia et al. (2018) within the Windsor body near wake. In-plane recirculation regions along multiple planes are connected to form the proposed structure. This description has been further supported in the studies of Pavia et al. (2020) and Fan et al. (2020). It is worth noting that this description is for the Windsor body which has a different forebody than Ahmed body variants and the forebody flow could affect the vortex structure.

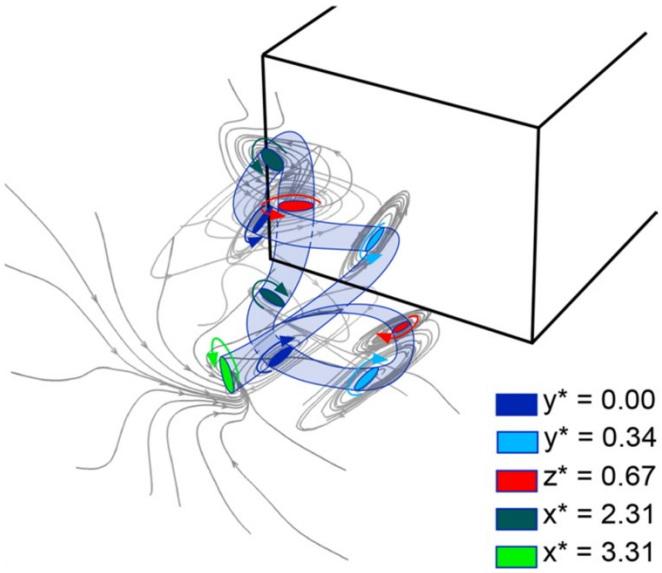

Figure 5: Proposed vortex hairpin structure within the phase-averaged wake of a Windsor body model (Pavia et al. 2018).

2.3 The Bluff Body Wake Topology at Yaw

Flat backed bluff body wakes at yaw have also been investigated to assess the effects of crosswinds on wake topology. Some initial conclusions about the flow topology at yaw can be drawn from the research focusing on instabilities within the wake. As was summarized in Section 2.2.2, several studies determined that the suppression of the bi-stability occurs at yaw angles greater than $|\beta| = 1°$ (Volpe et al. 2015; Grandemange et al. 2015; Bonnavion et al. 2018). They observed that the wake locked to a single bi-stable state as the yaw angle surpassed $|\beta| = 1°$, which could reasonably be extrapolated to describe the topology of the square-backed body wake at small yaw angles as similar to the single bi-stable mode. The range of yaw angles for which this description is accurate is however, yet to be quantified.

Recently, the effect of a $\beta = 5°$ yaw angle on the flow field was investigated by Li et al. (2019) for a square-back Ahmed body at $Re_H = 5\times10^5$. Measurements of mean velocity field using planar PIV showed that crossflow induced a large asymmetry in the wake structure along the spanwise axes. This asymmetry included a greater spanwise entrainment of flow along the leeward side of the body. The recirculation or separation bubble length was measured to be $x/H = 1.42$. The results also showed that the bulk of Reynolds stresses were concentrated along the windward shear layer. Another study by Lorite-Díez et al. (2020) carried out PIV measurements across mid-height of a square-back Ahmed body wake at three yaw angles of $\beta = 0°$, 5°, and 10°. They noted that the yawed flow deflected the recirculation bubble towards the leeward side of the wake. A decrease in the recirculation bubble length was also measured as the yaw angle increased. The influence of yaw can be seen in Figure 6 which shows the time-averaged PIV measurements of Lorite-Díez et al. (2020) for yaw angles of $\beta = 0°$, 5°, and 10°. The figure contains streamlines along the mid-height plane of the wake for each yaw angle with contours of spanwise vorticity overlayed. The flow direction is from left to right for all three subfigures.

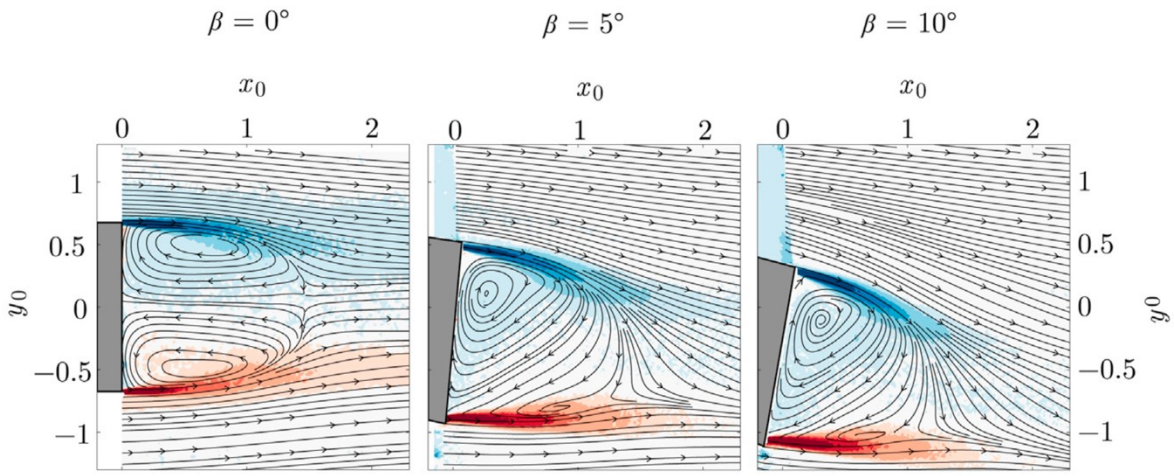

Figure 6: Mid-height velocity measurements with contours of spanwise vorticity for a square-back Ahmed body at three yaw angles of $\beta = 0°$, 5°, and 10° (Lorite-Díez et al. 2020).

2.3.1 Time-Averaged Wake Structures at Yaw

Based on what could be found in the literature, there has been minimal focus on the vortex structures that are present within the wake of bluff bodies at yaw. Gohlke et al. (2007) first experimentally investigated a Willy model for β up to 30° at $Re_L = 2.2\times10^6$. As described in Section 2.1, the Willy model has rounded edges along the length of the body, eliminating fixed separation points in crossflow conditions. The measurements showed two counter rotating vortices that formed along the leeward face of the body. These vortices separated from the body at $\beta > 10°$. A subsequent Lattice Boltzmann simulation by Gohlke et al. (2008) using the same model at $Re_L = 2.2\times10^6$, with yaw angles in the range of $-30° \leq \beta \leq 30°$, identified three more vortices, this time within the wake. They found a vortex ring that formed along the edges on the rear face, and two more vortices that extended out from the rear face. Figure 7 shows the proposed vortex system topology found by Gohlke et al. (2008). The vortex structures were based on the Lattice Boltzmann results and are identified using Γ_3 isosurfaces. At the time that this thesis was written and to this authors knowledge, there were no known studies of coherent structures at yaw for any square-backed bluff bodies.

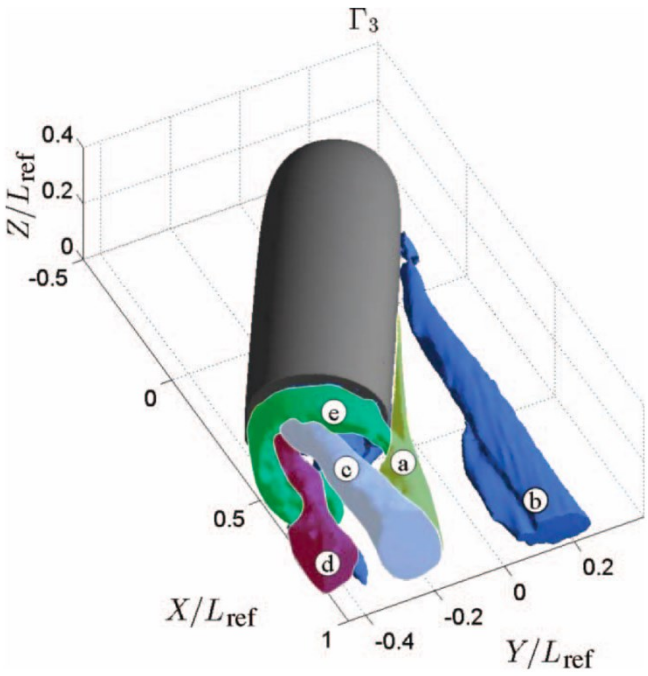

Figure 7: Proposed vortex structures within the wake of Willy body model at a yaw angle of β = 30° based on Γ_3 isosurfaces (Gohlke et al. 2008).

2.4 Spectral Properties of the Wake Flow

The spectral properties of the wakes have also been characterized and dominant frequency modes were identified within the square-backed body wakes. Duell et al. (1999) first analyzed spectral properties of a flat-backed bluff body model with equal base width and height and rounded longitudinal edges at $Re_L = 7.5\times10^5$. Anemometers were used within the wake to identify dominant frequencies. Frequencies were reported in terms of the height based Strouhal Number, defined as $St_H = fH/U$, where f is the frequency, H is the body height, and U is the flow velocity. One dominant frequency was measured at $St_H = 1.157$, which was attributed to vortex shedding in the shear layers. Another coherent fluctuation was identified in the base pressure measurements at a frequency of $St_H = 0.069$. This fluctuation was thought to be caused by streamwise oscillations or "pumping" of the separation bubble stagnation point.

Through experimental pressure measurements on the rear face of a square-backed body, Khalighi et al. (2001) also found a frequency peak a Strouhal Number of $St_H \sim 0.07$ at multiple

Reynolds numbers of $Re = 2.1\times10^5$, 2.8×10^5, 3.4×10^5. This frequency was again hypothesized to be a bubble pumping mechanism, where the stagnation point of the recirculation bubble periodically shifted along the streamwise axis. The pumping mechanism was later attributed to pressure differences along the wall-normal plane of the wake (Volpe et al. 2015), the pressure fluctuations being caused by the stretching and squeezing of a hairpin vortex structure within the wake (Pavia et al. 2018). Grandemange et al. (2013b) carried out a detailed study of the square-back Ahmed body's spectral properties using hot-wire anemometer measurements at $Re_H = 9.2\times10^4$. Two dominant frequency modes were identified corresponding to $St_H = 0.127$ and 0.174. The first mode was determined to stem from spanwise oscillations of the wake concentrated within the spanwise shear layers in the wake. The second came from wall-normal oscillations of the wake along the top and bottom shear layers. These frequency modes were shown to be caused by spanwise and wall-normal vortex shedding. The spanwise oscillations were in phase opposition, with the bi-stability phenomenon concentrating the oscillations on one side of the wake while the wall-normal shedding had a non-constant phase shift caused by interference of the ground plane with shedding from the lower edge. The bubble pumping frequency mode was not identified. A schematic of the proposed shedding modes can be seen in Figure 8. Figure 8(a) shows an illustration of the vertical shedding mode along the body height and Figure 8(b) shows the shedding mode across the wake span. A subsequent study by Volpe et al. (2015), confirmed the two shedding modes found by Grandemange et al. (2013b). No studies could be found with information regarding spectral properties of flat backed bluff bodies at yaw.

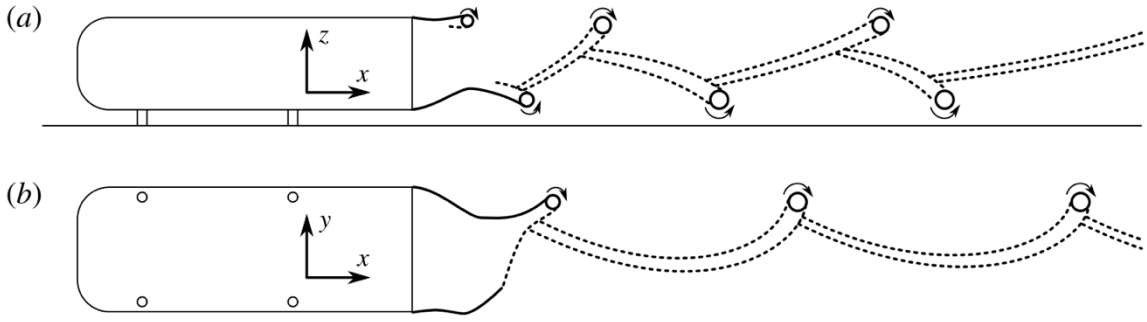

Figure 8: The suggested spatial patterns of the (a) wall-normal and (b) spanwise shedding modes within the wake of a square-back Ahmed body (Grandemange et al. 2013b).

2.5 Wake Analysis using Proper Orthogonal Decomposition

Proper orthogonal decomposition (POD) is an analysis method that allows for the identification of dominant fluctuations within a turbulent wake. It decomposes fluctuating velocity field in spatial modes that are ranked based on their contribution to the turbulent kinetic energy. Each spatial mode also has a series of temporal amplitudes. The underlying theory for POD analysis will be reviewed later in Section 2.5. This method has been used many times in the context of square-backed bluff body flows in order to better understand the wake dynamics.

Östh et al (2014) completed a POD analysis using LES results for a square back Ahmed body at $Re_H = 3\times10^5$ and found that the first mode contained a much larger proportion of energy relative to subsequent modes. Volpe et al. (2015) then analyzed the spatial modes from two different sets of pressure measurements along the rear face. The first spatial mode contained 65% of the total energy and was antisymmetric across the span. This spanwise spatial pattern was consistent with the both the bi-stability as well as the spanwise vortex shedding. Power spectral density (PSD) analysis of the mode amplitudes revealed a high energy peak at $St_H = 0.13$ which was the frequency previously found for the spanwise vortex shedding and thus further supported the connection. The second spatial mode contained 10% of the total energy. Its spatial pattern had a high amplitude region at the midspan, consistent across the height of the base. Two matching low amplitude regions were located to either side, resembling three vertical bands, with amplitudes fluctuating between the center and sides of the base. This pattern was attributed to the bubble pumping dynamic and again a PSD analysis of the amplitudes contained a peak at $St_H = 0.08$, supporting their conjecture. The third and fourth modes contained roughly the same energy content. Another distinct spatial pattern was observed within the two modes, showing an antisymmetric pattern switching across the height of the base. The mode was linked this time to the wall-normal vortex shedding. Perry et al. (2016) carried out a POD analysis on both pressure and stereo PIV measurements for a Windsor body model. Only the first mode was analyzed for the pressure measurements and closely matched the findings of Volpe et al. (2015). The first mode from the PIV results showed a spanwise asymmetry similar to the pressure-based mode and contained 15% of the total energy. Pavia et al. (2018) then expanded on the POD based flow description with an in-depth analysis of both pressure and PIV based modes for a Windsor body model. Both PIV and pressure measurements showed the already identified spanwise

antisymmetric pattern for the first spatial mode along with the $St_H = 0.13$ spectral peak. They referred to this mode as the lateral-symmetry breaking mode and attributed it to the bi-stability mode and the spanwise vortex shedding, consistent with Volpe et al. (2015). A second spatial mode was identified with a vertical asymmetry, again consistent with previous findings (Volpe et al. 2015). It was called the vertical-symmetry breaking mode. A third spatial mode was identified and related to symmetry preservation within the wake since this effect was identified when this mode was added to a reduced order model. Studying the coherence of pressure signals along the base perimeter, they also identified a connection between the bi-stable state of the wake and the strength of the wall-normal shedding, speculating that the vortex shedding strength was directly related to the interaction between the bi-stable wake mode and the top and bottom shear layers.

A study by Pavia et al. (2020) was the first to perform a POD analysis on 3D velocity data set within the wake of a Windsor body model at $Re_H = 5.78\times10^5$. They applied the decomposition to the u-velocity component only. The first mode contained approximately 20% of the total energy content followed by a large drop to < 3% for subsequent modes. The first three spatial modes were attributed to spanwise symmetry breaking, symmetry preservation, and vertical symmetry breaking, respectively. Another recent study by Fan et al. (2020) applied POD to both numerically and experimentally measured u-velocity components along 2D planes in the wake of a square back Ahmed body at $Re_H = 9.2\times10^4$. Again, the disproportionate first mode energy content was observed, accounting for 24% of the energy for experimental measurements and 15.7% for the numerical measurements. Aside from the dominant first mode, the mode number for each identified pattern varied depending on whether they came from numerical or experimental results. The three coherent spatial patterns identified, were related to the spanwise and wall-normal oscillations of the wake as well as a mode belonging to the bubble pumping mechanism. The spectra for the wake oscillation POD modes matched the expected frequencies for the vortex shedding modes. Pavia et al. (2018) also performed a POD analysis on the Windsor body model yawed to $\beta = 0.6°$. As noted in Section 2.2.2, it was found that the bi-stability was weakened which was noted in a decreased mode one energy and more asymmetric spatial patterns.

2.6 Aerodynamic Forces and Drag Reduction

2.6.1 Aerodynamic Forces at Zero-Yaw

The aerodynamic loading of these geometries has been the subject of several studies because of the relevance to real world forces and their effect on efficiency and stability. The study of Grandemange et al. (2013a) compared base pressures at different aspect ratios and ground clearances. They found that drag was at a minimum (relative base pressure was at a maximum) when the normalized aspect ratio H/W was low and the ground clearance (C) was in the range of $C/W < 0.05$, wherein the geometries resembled backwards facing steps. Drag reached a maximum at a ground clearances $C/W \approx 0.06$ and then stabilized to a smaller but constant value as ground clearance increased further.

Grandemange et al. (2014) tested the square-back Ahmed body's sensitivity to wake disturbances and found that the lowest base pressure differential followed when the base pressure was most homogenous. From the sensitivity analysis they were able to estimate that the bi-stability contributed between 4% - 9% of the total pressure drag. Forcing a stable, symmetric wake was suggested to be an optimal drag reduction strategy since the bi-stability would be suppressed and the base pressure would be homogenous. Evrard et al. (2016) experimentally investigated the effects of a base cavity and found that at cavity depths (d) of $d/H > 0.24$, the bi-stability phenomenon was suppressed, and the wake was symmetric. This effect lengthened the recirculation bubble and made the base pressure distribution more homogenous leading to a maximum drag reduction of 9%. Perry et al. (2016) incorporated horizontal edge tapers to the rear face of Windsor body in an attempt to minimize drag. They found that at taper angles of 12°, drag reduction was optimal, with the reduction being caused by the combination of a weakened bi-stability phenomenon and shortened recirculation bubble. Both effects came from increased upwash and downwash induced by the tapered edges; the amount of drag reduction was however not quantified.

A study by Lorite-Díez et al. (2020) recently analyzed the influence of a straight base cavity as well as a curved base cavity on the aerodynamic loading of a square-back Ahmed body. The results for the straight cavity confirmed the findings of Evrard et al. (2016) although only a 6.7%

drag reduction was achieved for a cavity depth of $d/H = 0.3$. The curved cavity was found to have a slightly different drag reduction mechanism, shortening the wake length instead while still suppressing the bi-stability phenomenon. This method resulted in a symmetric wake with a 9% drag reduction over the base geometry.

Boat tail geometries have also been tested, which resembled base cavities with inclined extensions instead around the perimeter. Schmidt et al. (2018) experimentally studied the effects of adding a boat tail to a GETS model, which is similar in shape to the square-back Ahmed body with a length and aspect ratio that better represent transport vehicles. For a boat tail geometry with an incline angle of 10°, they were able to measure a 17% drag reduction. Bonnavion and Cadot (2018) also tested the effects of varying boat tail incline angles using experimental measurements of square-back Ahmed body geometry with an altered aspect ratio at $Re_H = 4.0\times10^5$. They achieved a maximum drag reduction of 6.7% for a boat tail geometry with a top angle of 7.5° and a bottom incline angle of 5°. The boat tail drag reduction method has also been adapted to more realistic geometries; a study by the National Research Council of Canada (2015) tested boat tail concepts on a scale model of a tractor-trailer where they found drag reductions of up to 6.8%.

A summary of geometries and corresponding coefficients of drag at zero-yaw can be found in Table 1. The range of drag coefficients for base geometry square-backed bluff bodies are $C_D = 0.250 – 0.329$ for experimental investigations and $C_D = 0.330 – 0.356$ for numerical investigations.

Table 1: Measured drag coefficients for various square-backed bluff bodies with and without drag reduction devices.

Study	Model	Drag Reduction Method	Reynolds Number	Drag Coefficient
Ahmed et al. (1984)	Square-back Ahmed Body	N/A	$Re_H = 1\times10^5$	$C_D = 0.250$
Khalighi et al. (2001)	Square-back Bluff Body Variant	N/A	$Re_H = 1.7\times10^5$	$C_D = 0.300$
		Cavity Device		$C_D = 0.240$
Krajnović et al. (2003)	Flatted-backed Bluff Body Variant	N/A	$Re_H = 2.1\times10^5$	$C_D = 0.33$
Howell (2015)	Windsor Body Model	N/A	$Re_L = 1.8\times10^6$	$C_D = 0.30$
Khalighi et al. (2012)	Square-back Bluff Body Variant	N/A	$Re_L = 1.25\times10^6$	$C_{DB} / C_{DB} = 1$
		Cavity		$C_{DC} / C_{DB} = 0.80$
		Boat Tail		$C_{DBT} / C_{DB} = 0.70$
Grandemange et al. (2013b)	Square-back Ahmed Body	N/A	$Re_H = 9.2\times10^4$	$C_D = 0.274$
Evrard et al. (2016)	Square-back Bluff Body Variant	N/A	$Re_H = 4\times10^5$	$C_D = 0.288$
		Cavity (d^*=0.27)		$C_D = 0.262$
Perry et al. (2016)	Windsor Body Model	N/A	$Re_H = 7.7\times10^5$	$C_D = 0.274$
		12° Top TE Chamfer		$C_D = 0.265$
Lucas et al. (2017)	Square-back Ahmed Body	N/A	$Re_H = 3.96\times10^5$	$C_D = 0.356$
		Cavity (d^*=0.337)		$C_D = 0.322$
Schmidt et al. (2018)	GETS Model	N/A	$Re = 6.7\times10^5$	$C_D = 0.35$
		10° Boat Tail		$C_D = 0.29$
		20° Boat Tail		$C_D = 0.34$
Bonnavion and Cadot (2018)	Square-back Bluff Body Variant	N/A	$Re_H = 4.0\times10^5$	$C_D \sim 0.282$
		Boat Tail		$C_D \sim 0.263$
Lorite-Díez et al. (2020)	Square-back Ahmed Body	N/A	$Re_H = 1\times10^5$	$C_D = 0.329$
		Straight Base Cavity		$C_D = 0.307$
		Curved Base Cavity		$C_D = 0.299$

2.6.2 Aerodynamic Forces and Moments at Yaw

Gohlke et al. (2007) experimentally measured all six aerodynamic load components for a Willy body model across a yaw angle range of $|\beta| \leq 30°$. All components were reported relative to the body-indexed frame of reference. The drag force coefficient had a linear increase, peaking at a yaw angle of roughly $|\beta| = 18°$, and then decreasing linearly as yaw increased further. The side force coefficient had a linear trend throughout the range and its magnitude had the largest increase with yaw. The rolling moment and yawing moment also had approximately linear trends with yaw. The lift force and pitching moment only changed significantly at large yaw angles ($|\beta| > 18°$).

Howell (2015) studied the drag on a variety of automotive shapes at yaw angles (β) smaller than 25°, and again found that the drag increased almost linearly with yaw up to $|\beta| \sim 10°$. The additional drag was described as an "induced" drag component, which was proportional to the sum of the squares of the lift and side forces. This induced drag relation was originally proposed by Mercker (1986).

Volpe et al. (2014) investigated the effects of unsteady crossflow (transient gusts) over a square-backed Windsor body using a double wind tunnel. They observed that the side force coefficient is approximately 7% larger in case of transient wind guests relative to the steady crossflow condition. The lateral force was also generated with a delay with respect to the onset of the gust.

Perry et al. (2016) investigated the aerodynamic forces acting on a Windsor body at yaw angles of $|\beta| \leq 0.2°$ and found linear trends for the body aligned side force, yaw moment, and roll moment of the body. The only exceptions to these trends were when the yaw angles were small and the bi-stability was not fully suppressed.

The study by Lorite-Díez et al. (2020) looked at aerodynamic loads at yaw up to $\beta = 10°$ for the base square-back Ahmed body along with two passive drag methods: a base cavity and a curved base cavity. The straight cavity resulted in a body-indexed drag reduction at lower yaw angles ($\beta < 6°$) but its effectiveness decreased as yaw angle increased further. The curved cavity proved to be more effective showing roughly a 10% body-indexed drag reduction, with the reduction increasing with yaw angle. Side force coefficients for all three cases were found to be

much closer and increased more rapidly as yaw increased. The trends of the coefficients were compared for all three cases; the drag coefficient and side force coefficients all had linear trends while the Euclidean norms of the two coefficients had initially quadratic trends.

2.7 Particle Image Velocimetry

Particle image velocimetry (PIV) is a non-intrusive experimental measurement method that allows for quantitative measurements of local movement. In fluid flows the measurement of fluid movement allows for indirect measurement of fluid velocity. Tracer particles are introduced into a flow and ideally, they follow the fluid flow exactly. Sampling the locations of these particles at two different locations within a known time interval (at a known frequency) allows for the measurement of their velocity, which is assumed to be the same as the surrounding fluid, giving the velocity of the flow. This is the basic working principle of PIV. If this measurement is carried out across a fluid domain, the velocity of the fluid domain can be quantified. As is suggested by the title, PIV is dependent on two primary aspects: the particle in the flow and the imaging of the particles. These will be covered in more detail in the following sections.

2.7.1 Tracer Particles

PIV is based on the imaging of particles within a flow and measurement accuracy is therefore limited by how accurately the particles follow the fluid flow. To ensure a sufficient tracing fidelity, the particles have to meet a strict set of requirements, primarily focusing on the particles ability to trace the flow with minimal deviation, which is defined by the particle response time (Raffel et al. 2018). The response time (τ_P) is a measure of how long it takes for a particle to match a change in flow velocity as seen in Equation 1. Characteristics such as the particle size, density, and buoyancy are defining parameters for response time (Raffel et al. 2018). The particle response time can be calculated as

$$\tau_P = d_p^2 \frac{\rho_p}{18\mu} \quad (1)$$

where d_p is the particle diameter, ρ_p is the particle density, and μ is the dynamic viscosity of the fluid (Raffel et al. 2018). A second criteria for particles is how their time response compares to the expected timescales of velocity fluctuations in the flow, which is referred to as the characteristic time scale (τ_f) for the flow of interest (Raffel et al. 2018). The ratio between the particle response time and characteristic time scale is called the particle Stokes number (Raffel et al. 2018). It should be ensured that the particles selected have an appropriate particle stokes number for the flow of interest otherwise the measurements will not be true to the flow.

2.7.2 Particle Imaging and Light Scattering

The second aspect of PIV measurements is the imaging of the particles. This is the part of the process that directly enables the measurement of the fluid flow. Particle distributions are generally imaged with high-speed cameras, either using complementary metal-oxide semiconductor (CMOS) sensors or charge-coupled device sensors (CCD), resulting in images with particle positions given by the light intensity distributions within an imaging plane. Accurately extracting particle positions from the images is the second factor that can greatly influence accuracy of the flow field measurements.

Maximizing particle image contrast is a primary approach to improving particle definition to more accurately locate them. The contrast of particle in an image is dictated by the intensity of light being scattered and the energy (wavelength) of the light relative to surrounding imaging environment. This is directly determined by the number of photons scattered towards the imaging sensor and their energy. PIV setups and the corresponding particle selections therefore aim to maximize the scattering properties of particles. High power lasers are commonly used to increase both the number and energy of scattered photons. Lasers emit spatially and temporally coherent beams of a photons with a single high energy wavelength that are highly concentrated and directional. These factors mean the particle scattering properties also have to be considered during particle selection. The particle properties that dictate scattering are their size, shape, and refractive index ratio (Raffel et al. 2018). Light also does not scatter uniformly off particles so camera location and observation angles are important to factor into setups (Raffel et al. 2018). The amount of light scattered is dictated by the particle's scattering cross section size relative to the light

source's wavelength. When the particle diameter is smaller than the light wavelength, the scatter cross section is in the Rayleigh-scattering regime (Raffel et al. 2018). When the diameter is greater than the wavelength then the scatter cross section is in the Mie-scattering regime. Particles operating within the Mie-scattering regime scatter much more light, allowing for a sufficient image contrast to be maintained with lower illumination power.

2.7.3 General Procedure

PIV measurements follow a general procedure; the first step in carrying out PIV measurements is to determine the specifics of the experimental setup. The flow of interest will dictate the tracer particles and imaging requirements. Tracer particles will be selected based on the criteria mentioned in Sections 2.7.1 and 2.7.2. The imaging system itself consists of the cameras, a timing unit, and the light source. The cameras are selected based on the required image resolution, sensor properties, and imaging frequency while the camera lenses are chosen based on the required magnification and depth of field. The light source is commonly an Nd:YAG laser due to their high power output and energy density. With the equipment selected, the positioning and setup is carried out. The laser is augmented with optics so that the laser output covers the region of interest. Camera positions are chosen based on physical limitations related to the region of interest, the required magnification, particle scattering angles, and the number of cameras.

When the PIV setup is in place, the imaging process can begin. Best practice calls for an initial calibration of the cameras to the region of interest, which is completed by imaging a standardized calibration target that is placed within the measurement region. The imaging can then commence; tracer particles are introduced into the fluid flow, the measurement region is illuminated by the laser, and images are taken. The timing unit controls the laser pulse and camera imaging frequency so that image quality is maximized and the time intervals between images are accurate and consistent.

The final step is to process the images and extract the velocity field. Many steps can be taken to improve image quality, but the fundamental step is the cross correlation of the particle images which results in the velocity vectors. Two consecutive images are first subdivided into interrogation windows and then a cross correlation of the particle distributions within each window is carried out. During the cross correlation process, the interrogation window of the second image

in the time series is shifted in space, forming a correlation map based on the particle image intensities. The physical shift in particle position between the two images is quantified by the shift that corresponds with the highest correlation coefficient in the correlation map. The velocity vector is calculated using the shift direction, magnitude, and the time interval.

2.7.4 PIV Error Sources

PIV measurements are the culmination of many different steps, each operating under different principals and each introducing their own uncertainties into the final PIV results. Errors can first be introduced as mechanical errors in the experimental setup, which can take many forms. The illuminated measured field may not align with the desired imaging plane which would result in misalignment between the measured and desired velocity fields (Raffel et al. 2018). Many optical error sources also exist, related to both the optics systems used and the optical properties of the experimental setups. Camera optics can introduce errors in the measurement plane and particle positions with inherent distortions such as barrel distortion, pin-cushion distortion, and perspective distortions (Raffel et al. 2018). Refractive index differences between flow and imaging mediums or measurement system features such as windowpanes can also introduce imaging distortions or aberrations.

After collection of the particle images, errors can be introduced within the processing phase. The extraction of particle displacements relies on obtaining distinct cross correlation coefficient peaks which intern relies on the proper identification of particle locations within image sets. One of several factors that dictates the accuracy of this process is the particle image diameter. If the particle image diameter is too small, then the particle location can become locked to a specific pixel location, which is referred to as peak locking. If a particle image registers a disproportionately high intensity in one pixel, the particle location could lock to that pixel's integer value location, blocking sub-pixel locating. On the other hand, if it's too large then efficient identification of particle image peaks is affected. The recommended size can change based on the processing techniques used but is recommended to be close to a 3 pixel diameter (Raffel et al. 2018). Low particle image density and high image noise within measurements should also be avoided as they can hamper the cross correlation peak identification.

The final error considerations are the random errors present within all experimental measurements. Random errors have to be statistically calculated and summed with the bias errors introduced in the above text to identify the total error within PIV measurements. The cumulative errors then need to be taken into account for any analysis based on the PIV results through error propagation calculations. As displacement error of 0.1 pixels is a general estimate of how much error there may be in a PIV measurement.

2.8 Particle Tracking Velocimetry

The primary measurement method used within this thesis was 3D Particle Tracking Velocimetry (3D-PTV). A fluid flow of interest is seeded with tracer particles, the tracer particles are illuminated, and the flow is imaged. The velocity is then calculated based on the particle displacement over the imaging time. The difference between PIV and PTV arises from what is used to calculate the velocity. PTV, as the name suggests, only uses the displacement of single particles to calculate the velocity, following the particles' pathlines and resulting in the Lagrangian perspective of the velocity field. For comparison, PIV uses the ensemble displacement of particles within an interrogation window to calculate the Eulerian velocity field. Particle selection and the experimental setup are generally shared between the two measurement methods, so they won't reviewed again. The remainder of this section will focus on Shake-the-Box (Schanz et al. 2016), a specific 3D-PTV algorithm used for measurements within this thesis.

Shake-the-Box combines several particle reconstruction methods and techniques to allow for the efficient identification of particle tracks with fewer resulting ghost particles (Schanz et al. 2016). The most basic implementation of 3D-PTV uses triangulation of single particle distribution snapshots to reconstruct 3D particle positions (Schanz et al. 2016). The 3D particle positions are then tracked across snapshots giving the particle tracks. The reconstruction of the 3D particle distributions is completed without making use of the spatial and temporal flow information that is available in a time series of snapshots. Assuming the flow statistics are converged, a much more efficient approach can be derived using these two additional domains. This is the basic premise of Shake-the-Box; the converged statistics from previously tracked particles are used to predict future particle position, greatly increasing the efficiency of the reconstruction process.

2.8.1 Optical Transfer Functions

Optical transfer functions (OTF) are relied on during several stages of the Shake-the-Box process and will therefore be reviewed first. A primary step in most 3D measurements techniques is the reconstruction of the 3D particle distribution from the multiple 2D particle image planes. This reconstruction process hinges on being able to use the locations of the 2D image planes and the corresponding particle projections to locate the 3D particle distributions. This process is traditionally accomplished with triangulation. A more efficient way to complete this process, however, is with the use of a mapping function, which predefines the relations between the multiple 2D image planes and 3D space. The mapping function relates pixel locations on the 2D planes to corresponding voxels in the reconstructed volume. Schanz et al. (2013) introduced a method for calculating the mapping function called the non-uniform optical transfer function. This function gives normalized weightings to pixels, based on their influence on a given voxel. The weighting function permits non-uniform weighting on the image planes which better accounts for optical distortions that are unavoidable in experimental imagining (Schanz et al. 2013). The expression for the weighting function is given in Equation 2:

$$W(x,y) = p \cdot \exp\left(-\frac{1}{2}\begin{pmatrix} x \\ y \end{pmatrix}^T \begin{pmatrix} a & b \\ b & c \end{pmatrix}\begin{pmatrix} x \\ y \end{pmatrix}\right) \qquad 2$$

where the normalized weight assigned to the pixel of interest is given as W, x and y are the pixel coordinates, a, b, and c denote the image shape, and p is the peak height. These coefficients are initially determined using the calibration process which involves imaging a calibration target with a known spatial pattern with tight tolerances. The weighting function can then be further refined using volume self-calibration (Wieneke 2008) which uses experimental particle locations to assess and correct for disparities between their true locations in 3D space and their projected locations on the imaging planes. Volume self-calibration can identify the influence of projections on the shape of the particle helping optimize the image shape coefficients in Equation 2 (Schanz et al. 2013). The OTF can then be fully defined by combining the weighting function W with a mapping function M which relates the pixel locations to voxel locations.

2.8.2 The Shake-the-Box Method

The general Shake-the-Box methods relies on some initial particle track convergence stages where the algorithm is similar to the IPR method of Wieneke (2013) initially and then takes on an adapted Shake-the-Box approach (Schanz et al. 2016). Assuming that the Shake-the-Box algorithm has achieved an initial convergence and true tracks have been identified for a minimum number of time steps then the steps of the general Shake-the-Box algorithm follow. The process begins with the particle distributions and corresponding particle velocities from the previous time step. The particle trajectories are extrapolated to the theoretical positions that correspond with the time instance of the next measured image set, resulting a predicted 3D particle distribution. This predicted distribution is then projected onto the image planes with the OTF, which allows these predicted 2D particle images to be compared to the experimentally acquired images. The projection process is summarized in Equations 3 to 7. The projected intensities of the predicted 3D particles, I_{Part}, are calculated using Equation 3:

$$I^{i}_{\text{Part}(x_i,y_i,p)} = a\, e^{-\left(bx''^2 + cy''^2\right)} \tag{3}$$

where a, b, and c are the shape coefficients from the OTF. The particle rotations, x'', y'' are defined using Equations 4-5 as:

$$x'' = \left(x_i - x_{ip}\right)\cos\alpha + \left(y_i - y_{ip}\right)\sin\alpha \tag{4}$$

$$y'' = \left(x_i - x_{ip}\right)\sin\alpha + \left(y_i - y_{ip}\right)\cos\alpha. \tag{5}$$

The projected particle center locations are then found with Equation 6:

$$\left(x_{ip}, y_{ip}\right) = M_i(X_P, Y_P, Z_P) \tag{6}$$

where M_i is the mapping function. Finally, the projected image planes can be calculated by summing the individual particle intensities onto the image plane using Equation 7:

$$I^i_{\text{proj}}(x_i, y_i) = \sum_p I^i_{\text{Part}}(x_i, y_i, p). \quad (7)$$

The projected image planes now act as an initialization of the particle distributions which is a primary advantage of this technique. Using the projected particle distributions, residuals can be calculated by subtracting the particle intensities of the projected image from the experimental images. The residuals represent the deviations between the measured experimental particle locations and the predicted particle locations. The residual intensities are calculated using Equation 8:

$$I_{\text{res}} = I_{\text{rec}} - I_{\text{proj}} \quad (8)$$

where I_{res} is the residual intensity, I_{rec} is the intensity of the recorded particle, and I_{proj} is the intensity of the projected particle. With the initial residual intensities calculated, the "shaking" phase can begin and acts to minimize the residuals (errors in the current predicted particle positioning). The shaking procedure consists of shifting all of the predicted 3D particle locations individually along one coordinate axis by a small step size. After each shift, the particles are reprojected, and this new distribution is compared with the experimental images using the residual intensity calculation process covered by Equations 9-10. Following Equation 9, particle intensity is first adjusted by adding the current residual intensity to the most recent particle intensity, I_{Part}:

$$I_{\text{res}+p} = I_{\text{res}} + I_{\text{Part}[x,y,z,I_{\text{P}}]}. \quad (9)$$

Then at each shifted particle position, a new residual, R, is calculated using Equation 10:

$$R[x', y', z', I_{\text{P}}] = \left(I_{\text{res}+p} - I_{\text{Part}[x',y',z',I_{\text{P}}]}\right)^2 \quad (10)$$

which subtracts the intensity of the shifted particle from the adjusted intensity calculated by Equation 9. Each shake shifts the particles to three different positions $x_i' = [x_I, x_I - \delta_S, x_I + \delta_S]$. The recommended shift size is $\delta_S = 0.1$ px. Final particle position is optimized by shifting particles to the three locations, fitting a second order polynomial to the resulting residual values, and then

selecting the optimal shift size corresponding to the minimum residual along the curve. Optimized particle positions are found one coordinate axis at a time, using the previously optimized particle positions for each subsequent coordinate axis shift (i.e. $[x_{New}, y, z]$, $[x_{New}, y_{New}, z]$,). The conclusion of this process means that the predicted particle distribution matches the distribution of the experimental imaged flow.

With the completion of the shaking process and the identification of all particles belonging to established tracks, new tracks can then be identified based on the residual particles remaining after the process is finished. These new particle locations are properly identified using triangulation and the IPR method. Similarly, at the end of the shaking process, any tracks that have not had the next particle position identified are assumed to have ended. This process then repeats for the subsequent time step. Multiple passes for each time-step can be performed to further eliminate any errors in particle positions. The multiple passes use the final particle positions of the previous pass as the residual for the next. Figure 9 shows a schematic illustration of this general Shake-the-Box procedure for one iteration to give a visual representation of the many steps.

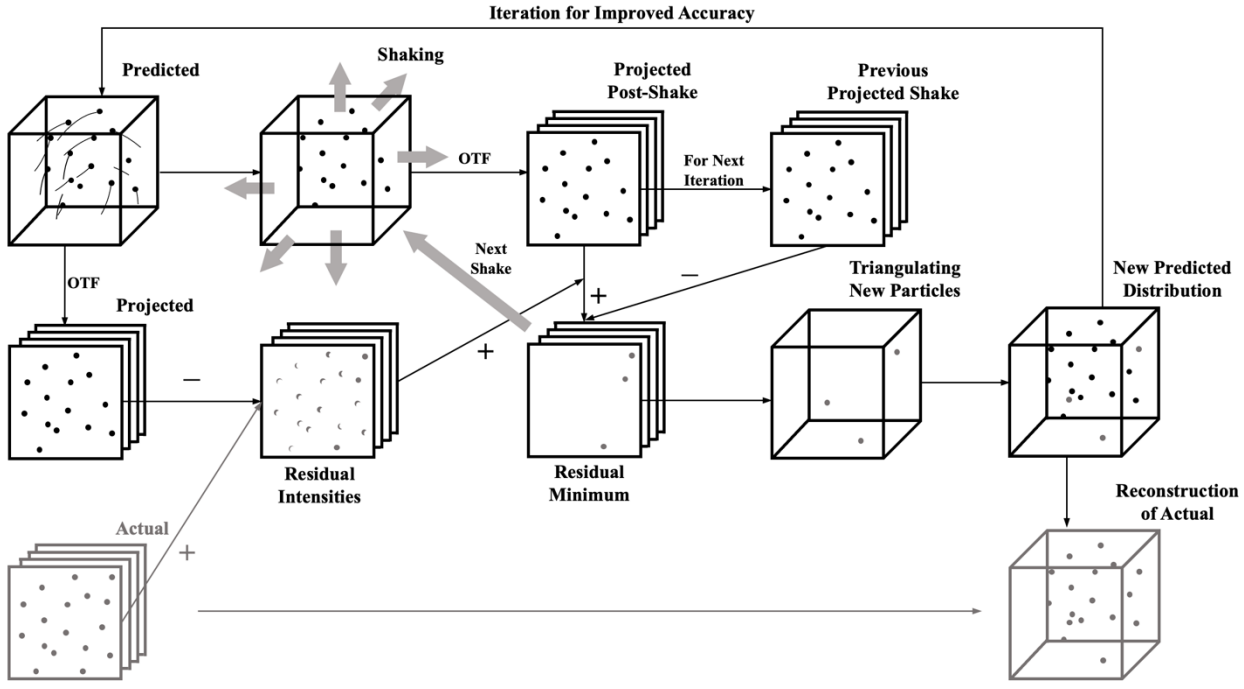

Figure 9: Schematic representation of the Shake-the-Box procedure for one iteration in the fully converged state.

2.9 Data Analysis Techniques

2.9.1 Vortex Centerline Identification

As a part of the mean flow characterization for each flow case, vortex structures are isolated and identified within the wake. The first method of doing so used the vortex center identification method proposed by Sujudi and Haimes (1995). This method utilizes critical point theory and begins with a structured velocity grid which is decomposed into tetrahedral cells. Using linear interpolation, the rate-of-deformation tensor at a critical point is calculated within each cell and the corresponding eigenvalues are found. If the eigenvalues contain one real eigenvalue and a pair of complex-conjugate eigenvalues, then they represent a spiral-saddle pattern on a plane normal to the real eigenvalue. The eigenvector of the real eigenvalue is used to identify the center of the spiralling flow. This results in the identification of the vortex centerline, showing its spatial position and orientation.

2.9.2 Q-Criterion

A second method was also used to identify coherent vortex structures within the mean flow wake for each case based on Q-criterion identification. Q-criterion, which was first proposed by Hunt et al. (1988), defines a vortex structure based on ratio between the shear strain and vorticity magnitudes in the flow (Jeong et al. 1995). The definition of the Q-criterion follows Equation 11:

$$Q = \frac{1}{2}[\|\boldsymbol{\Omega}\|^2 - \|\boldsymbol{S}\|^2] > 0 \qquad 11$$

where a vortex is identified when the norm of the local vorticity is greater than norm of the local strain tensor (Jeong et al. 1995). Mathematically this is equivalent to when the balance of the anti-symmetric rotation tensor ($\boldsymbol{\Omega}$) is greater than the corresponding symmetric strain rate tensor ($\boldsymbol{S}$). The definition in Equation 11 can be expanded to take the form of Equation 12:

$$Q = -\frac{1}{2}\left[\left(\frac{d\langle U\rangle}{dx}\right)^2 + \left(\frac{d\langle V\rangle}{dy}\right)^2 + \left(\frac{d\langle W\rangle}{dz}\right)^2 + 2\left(\frac{d\langle U\rangle}{dy}\frac{d\langle V\rangle}{dx}\right) + 2\left(\frac{d\langle U\rangle}{dz}\frac{d\langle W\rangle}{dx}\right) + 2\left(\frac{d\langle V\rangle}{dz}\frac{d\langle W\rangle}{dy}\right)\right] > 0 \quad (12)$$

which is the form that was implemented for the analysis within this thesis.

2.9.3 Power Spectral Density

The power spectral density of velocity signals was also used to analyze wake spectral properties. The power spectral density is found by taking discrete samples of a velocity signal at a given point and then computing the discrete Fourier transform (DFT) of overlapped segments; this gives the frequency domain properties of the sampled signal (Welch 1967; Heinzel et al. 2002). A window function is first applied to the segmented input signal to minimize the effects of a performing a DFT on a signal with frequencies that do not have integer numbers of cycles within the segment, corrupting the theoretically continuous signal. The window function tends to near zero values at the edges of the window which minimizes the effects of incomplete frequency intervals at the ends of a segment. For the PSD analyses in this thesis, a Hanning window is applied with a 50% overlap. The overlap allows for more of the signal to be used since the window function effectively eliminates useable signal at the ends of each segments. The formulation of the DFT can be seen in Equation 13:

$$y_m = \frac{1}{N}\sum_{k=0}^{N-1} x_k e^{-2\pi\frac{mk}{N}} \quad (13)$$

where y_m is the DFT output in the frequency domain, x_k is the signal input after been multiplied by the windowing function, k is the index of the current input sample, m is the index of the output number, and N is the length of the DFT. For segmented signals, the outputs of the DFT are averaged over the segments (Heinzel et al. 2002). The power spectral density (PSD) is then calculated using Equation 14 (Heinzel et al. 2002):

$$\mathrm{PSD} = \frac{2|y_m|^2}{f_s S_2}. \qquad 14$$

It is proportional to the square of the DFT output magnitude and is normalized by the sum of the square of windowing function coefficients S_2 and the sampling frequency f_s.

2.9.4 Proper Orthogonal Decomposition

Proper orthogonal decomposition (POD) is an eigen value-based coherency analysis of a data set (Lumley 1967). Within the context of fluid flows, it is a mathematical decomposition of a discrete series of fluctuating velocity measurements, resulting in spatial modes that are ranked based on their contribution to the total turbulent kinetic energy and corresponding temporal coefficients for each mode that describe the mode evolution in time. POD can be used to create low order representations of complex data series since the spatial modes are orthogonal and are ranked based on their cumulative contribution to the base set. The general principal of POD can be seen in Equation 15:

$$\mathbf{u}'(\mathbf{x}, t) = \sum_{i=1}^{N} a_i(t)\mathbf{u}_i(\mathbf{x}) \qquad 15$$

where the fluctuating velocity field, $\mathbf{u}'(\mathbf{x}, t)$, is decomposed into the sum of spatial modes, $\mathbf{u}_i(\mathbf{x})$, and the corresponding temporal coefficient, $a_i(t)$ (Luchtenburg 2009). The method of snap shots POD (Sirovich 1987) was used within this thesis because of its suitability to decomposing data sets with high numbers of spatial variables (Luchtenburg 2009). It is based on autocorrelation of snap shots within the temporal domain, which results in the same final spatial modes, but the decomposition basis is the temporal domain and not the spatial, which can be orders larger for measurements with a high spatial resolution. First the correlation matrix, *C,* is formed with a number of snap shots, *M*, using Equation 16:

$$C_{mn} \coloneqq \frac{1}{M}\left(\mathbf{u}'(\mathbf{x}, t_m), \mathbf{u}'(\mathbf{x}, t_n)\right)_{\Omega}. \quad 16$$

Using the correlation matrix, the eigenproblem in Equation 17:

$$C_{mn}\mathbf{a}_i = \lambda_i \mathbf{a}_i \quad 17$$

can be solved resulting in eigenvalues, λ_i, and eigenvectors, $\mathbf{a}_i$. The spatial modes can then be calculated using Equation 18:

$$\boldsymbol{\phi}_i = \sum_{i=1}^{N} \mathbf{a}_i \mathbf{u}(t_n) \quad 18$$

which projects the eigenvectors onto the time signal of the velocity at a set point in space $\mathbf{u}(t_n)$. The final normalized spatial modes, $\mathbf{u}_i$, are calculated with Equation 19:

$$\mathbf{u}_i = \frac{\boldsymbol{\phi}_i}{\|\boldsymbol{\phi}_i\|_2}. \quad 19$$

Corresponding temporal coefficients are determined by reprojecting the spatial modes, $\mathbf{u}_i$, onto the time series $\mathbf{u}(t)$ using Equation 20:

$$a_i(t) = \left(\mathbf{u}_i, \mathbf{u}(t)\right). \quad 20$$

Lastly, the eigenvalues of each mode can be used to determine their energy content since the eigenvalue represents the energy contribution. The percent energy contribution, E_i, can be calculated following Equation 21:

$$E_i = \frac{\lambda_i}{\sum \lambda_i}. \quad 21$$

Chapter 3: Experimental Setup and Data Analysis

For the research subject of this thesis, the square-back Ahmed body was selected. Based on the literature reviewed in Chapter 2, this model had a very strong base of literature for zero-yaw characteristics but its characteristics at yaw had only been the subject of a limited number of studies. This aligned well with the motivations for this thesis that were summarised in Chapter 1.

This chapter will outline the experimental measurement setups, measurement techniques, and relevant equipment used to collect data for this thesis. The base square-back Ahmed body geometry is first introduced along with the supporting structures that allowed for integration into the wind tunnel. Experiment I is then detailed, covering the 2D-PIV setup, 3D-PTV setup, and the HFSB system, all used to collect data for Chapter 4. Finally, a summary for Experiment II is given, showing the setup used to collect the aerodynamic load measurements that are later discussed in Chapter 5.

All of the measurements for this thesis were carried out in a closed-loop wind tunnel located at the University of Alberta. The test-section of the wind tunnel has a cross section of 2.4 m × 1.2 m and is located after a nozzle with a contraction ratio of 6.3:1.

3.1 Square-back Ahmed Body Geometry

The research subject was chosen to be a half-scale square-back Ahmed body. The dimensions of the wind-tunnel model used are 522 mm in length (L) × 195 mm in width (W) × 144 mm in height (H). Figure 10 shows a schematic of the Ahmed body with dimensions. As can also be seen in the Figure 10, the Ahmed body was positioned on a flat plate that was installed 110 mm above the wind tunnel floor. The plate raised the Ahmed body above the turbulent boundary layer that forms on the wind tunnel floor while also emulating the effects of the road surface proximity. The bottom face of the Ahmed body was 25 mm above the plate and the plate's leading edge was 200 mm ahead of the Ahmed body. The gap between the Ahmed body and the plate was set by adjustable mounts supporting the plate. This ensured that the correct gap was maintained

throughout the length of the body. The boundary layer plate also has streamlined leading and trailing edges and extends more the twice the length of the wake past the rear face. This length was based on the finding of previous studies. Similar configurations have been used by previous investigations (Gohlke et al. 2007; Grandemange et al. 2013b; Volpe et al. 2015).

Slots were cut into the boundary layer plate to allow for the body to be yawed while maintaining the boundary layer plate position. These slots allowed of up to 30° of yaw in both directions. The slots were covered during experiments to ensure there was no interference from the flow underneath the plate. The coordinate system for the model changed between Experiments I and II, so the coordinate systems used for each experiment and their subsequent analyses will be introduced in context. The complete engineering drawing package for the manufacturing of this model can be found in Appendix B.1.

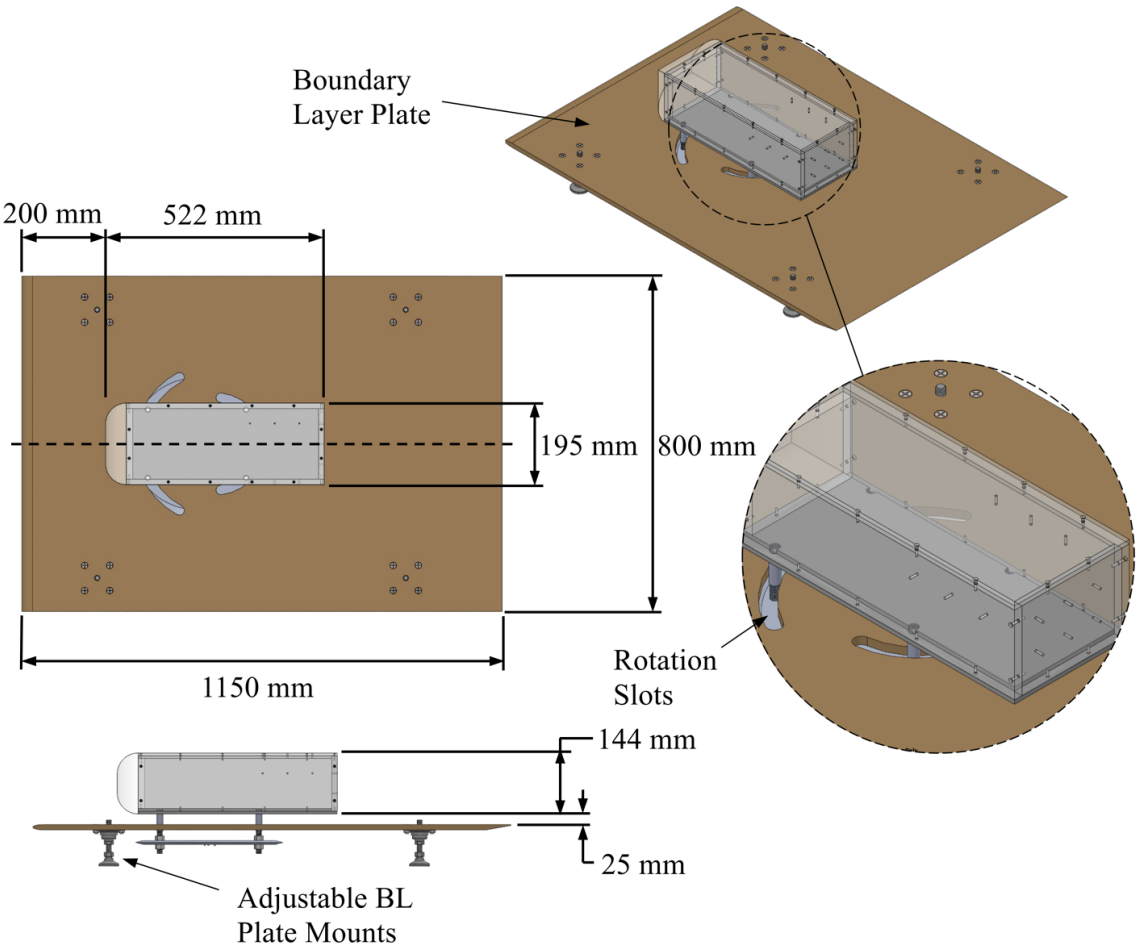

Figure 10: Schematics showing the geometry and dimensions of the half-scale square-back Ahmed body and the boundary layer plate used within the investigations of this thesis.

3.2 Experiment I: Wake Characterization at Yaw

Experiment I details the experiments used to analyze and characterize the wake of the square-back Ahmed body at yaw. The results are discussed in Chapter 4.

3.2.1 Planar 2D-PIV Measurements

To properly study the Ahmed body wake at various yaw angles, the zero-yaw angle had to first be properly defined. With the Ahmed body assembly installed in the test section, a planar 2D-PIV system was setup to analyze the alignment and symmetry of the wake. The setup consisted of a high-repetition dual-cavity Nd:YLF laser (Photonics Industries) light source with a pulse energy of 20 mJ per cavity and a single high-speed CMOS camera (Phantom V611) with an attached 60 mm lens. The camera had a sensor size of 1280 × 800 pixels with pixel sizes of 20 × 20 μm^2. The magnification of the camera system was approximately 0.06. The laser beam was expanded using a concave lens to illuminate the wake region. The measurement plane was on the *xy*-plane at the mid-height of the body with the high-speed camera positioned above the test section as can be seen in Figure 11. Dual frame PIV measurements were recorded at a frequency of 12 Hz with a freestream velocity of U_∞ = 10 m/s, which corresponds to a Reynolds number of $Re_H = 9.2\times10^4$ based on body height and free stream flow-speed. A height-based Reynolds number was chosen for two primary reasons: it has become convention within related automotive bluff body research and the height is a defining dimension for the wake. The time delay between the dual frame images was set to 150 μs. During one measurement, 3034 images were taken which equated to an imaging duration of 250 seconds or $TU_\infty/H \approx 17000$. This was a much longer time period than that of the mean bi-stable mode duration ($TU_\infty/H = 420$), ensuring that on average at least 40 switches would be measured. The estimated uncertainties for this planar PIV method are 0.1 pixels (Raffel et al. 2018). Using the digital resolution of 0.333 mm/pixel, this corresponds to a velocity uncertainty of $0.022U_\infty$.

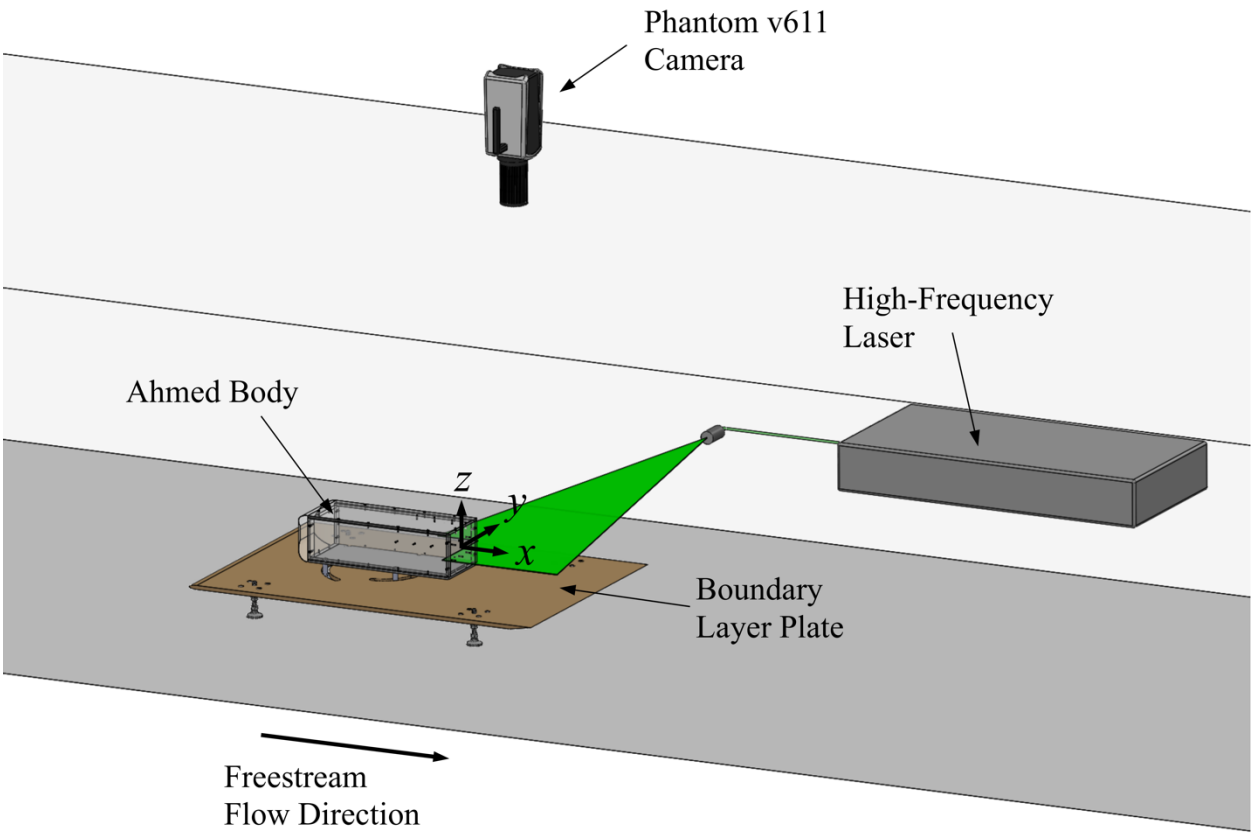

Figure 11: A schematic of the experimental setup used to collect planar PIV measurements along the mid-height plane of the Ahmed body wake.

The Ahmed body rotation was set by the yaw table which had a yaw resolution of $\beta = \pm 0.5°$. The criteria used to evaluate alignment of the body relative to the flow was decided to be the identification of both bi-stable wake modes. Based on the study of Volpe et al. (2015), the bi-stability phenomenon within the wake was found to be highly sensitive to yaw. At yaw angles greater than $|\beta| > 0.2°$, a single mode of the bi-stability was dominant and at yaw angles of $|\beta| > 1°$, the bi-stability became fully supressed with only one mode being expressed. With these limits, if both bi-stable spatial patterns could be observed in the planar PIV measurements, then the yaw angle was known to be within the range of $|\beta| < 1°$. Small subsets of the recorded images that matched the expected mean bi-stable mode duration of $TU_\infty/H = 420$ (6 seconds) were averaged. This procedure is equivalent to applying a 0.17 Hz low pass filter to the data set. The measured velocity fields of the averaged subsets were then used to identify the current phase of the bi-stability phenomenon over the measurement period.

3.2.2 3D-PTV Measurements

The first objective of this thesis was to measure and characterize the three-dimensional wake of the square-back Ahmed body at yaw. To be able to analyze the 3D wake, 3D-PTV (Shake-the-Box) was chosen as the measurement technique. Three cases were selected for the analysis, corresponding to yaw angles of β = 0°, 5°, and 10°, which provides a baseline measurement for comparison as well as spans a range of realistic crossflow driving conditions (SAE International 2012; Garcia de la Cruz et al. 2017; Dalessio et al. 2017). All measurements were made at a freestream flow rate of U_∞ = 10 m/s, which is equivalent to a Reynolds number of $Re_H = 9.2\times10^4$ based on body height and free stream flow-speed. At the largest yaw angle of β = 10°, the blockage of the Ahmed body relative to the cross-sectional area of the wind tunnel was 1.4%.

The experimental setup used to carry out the measurements can be seen in Figure 12. For the 3D-PTV measurements, a volume in the wake of the Ahmed body was illuminated using a high-repetition dual-cavity Nd:YLF laser (Photonics Industries) with a pulse energy of 20 mJ per cavity. The laser beam was expanded using a spherical concave lens with a focal length of -100 mm. The expanded beam was cropped to the form a rectangular cross-section using knife-edges. The illuminated volume was imaged using four high-speed CMOS cameras (Phantom V611) with a sensor size of 1280 × 800 pixels, each pixel being 20 × 20 μm^2. The cameras were equipped with SLR lenses with a focal length of f = 105 mm which were connected to the camera bodies using Scheimpflug adapters. The cameras were arranged in a cross configuration. The imaging distance of the lens was approximately 1.6 m, with the apertures set at f / 16. The magnification of the cameras was roughly 0.067. Helium-filled soap bubbles (HFSB) were chosen as tracer particles for the flow and will be discussed in more detail in Section 3.2.3. The resulting images of the HFSB particles were approximately 2-3 pixels in diameter. A seeding density of 0.02 particle per pixel was obtained in the 3D-PTV images. The imaging system was calibrated using a dual-plane target with the planes separated by 3 mm. The target was placed parallel to the xz-plane on a traverse, and a total of three views, 5 mm apart, were recorded by traversing the target along the y axis. These images were then used to obtain a mapping function for the measurement volume using a 3rd order polynomial fit in Davis 10.1 (LaVision GmbH).

The origin of the coordinate system was centred along the width and height of the Ahmed body's rear face at zero yaw as seen in the inset of Figure 12. The coordinate system was fixed

with respect to the wind tunnel with its x-axis aligned with the flow direction. The y-axis corresponded with the spanwise direction; the z-axis corresponded to the direction normal to the flat plate located under the Ahmed body. The yaw angle, β, is the angle between the Ahmed body and the x-axis in the xy-plane. Henceforth, the side of the body angled upstream will be referred to as the windward side and the opposite will be referred to as the leeward side.

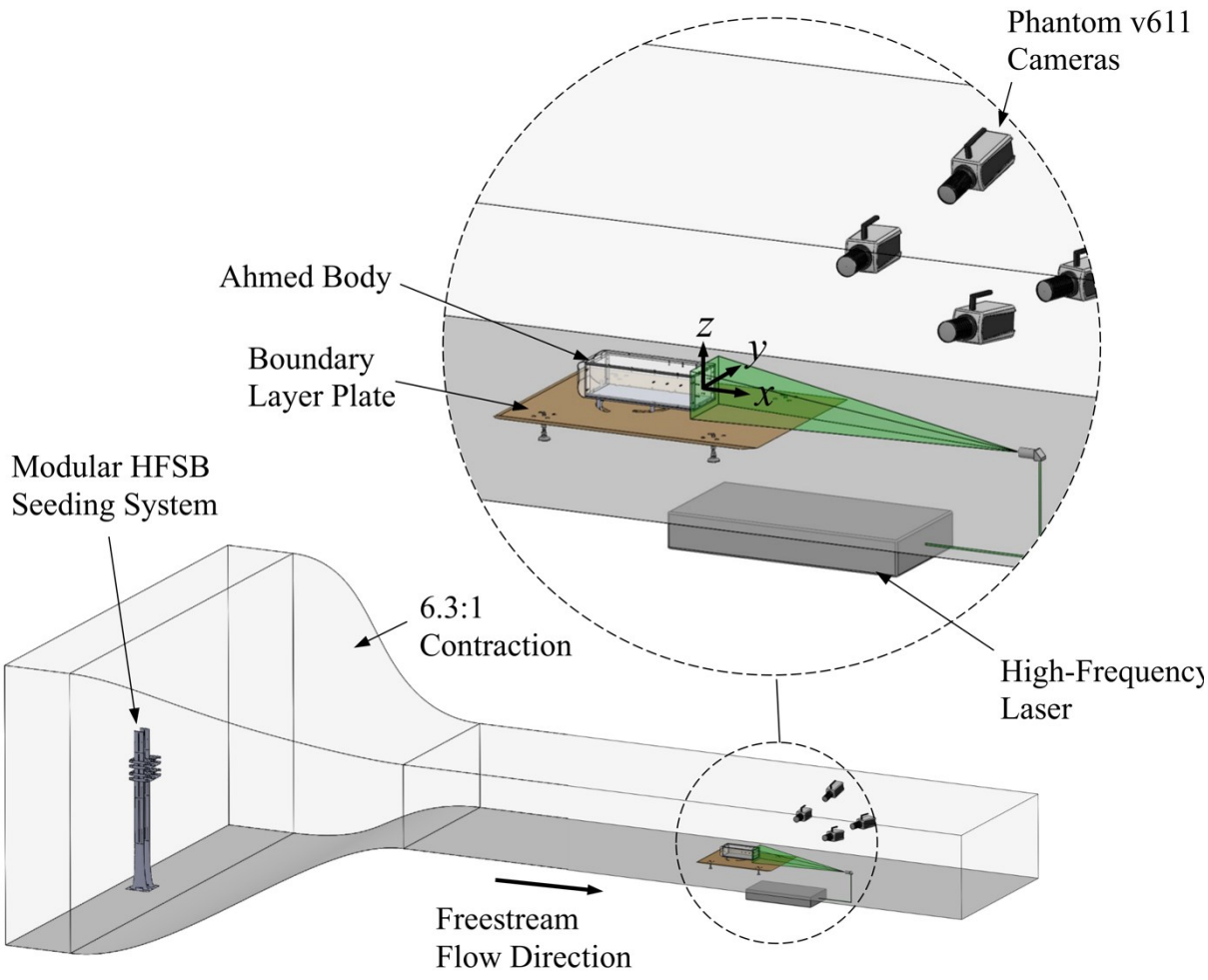

Figure 12: A schematic of the experimental setup showing the wind tunnel, the Ahmed body installed on a flat plate, the 3D-PTV system, and the system used for generating the helium-filled soap bubbles.

The final measurement volume for the $\beta = 0°$ case was approximately 350 mm × 240 mm × 180 mm ($x \times y \times z$). For the $\beta = 5°$ and 10° cases, the measurement volume was approximately 350 mm × 300 mm × 180 mm ($x \times y \times z$) to cover a wider wake region. Figure 13 shows the size and position of the measurement volume for each case as well as the rotation of the Ahmed body. The measurement volumes were located in the wake region of the Ahmed body, each with a slight overlap with the rear of the body. Note that the coordinate system is fixed with respect to the wind tunnel, therefore the x-axis remains parallel to the streamwise direction for all cases.

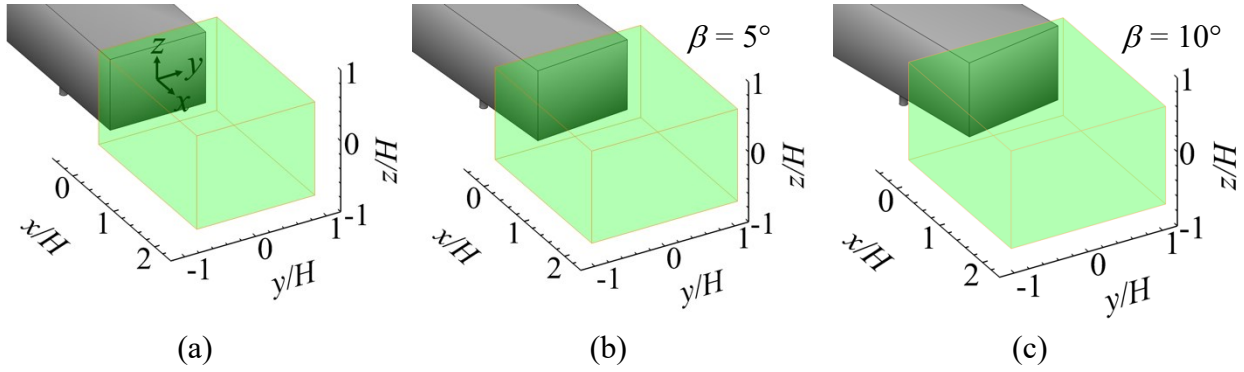

Figure 13: The illuminated measurement volumes in the wake flow of the Ahmed body for yaw angles of a) $\beta = 0°$, b) $\beta = 5°$, and c) $\beta = 10°$.

The recorded images were processed using a commercial software (Davis 10.1, LaVision Gmbh). First, the minimum intensity of the images ensemble was subtracted from each image to remove any background noise. The images were then normalized using the ensemble average of the images. A volume self-calibration process was applied on the resulting images to eliminate the remaining calibration disparities (Wieneke 2008). An optical transfer function was also estimated (Schanz et al. 2013). Finally, the shake-the-box (STB) algorithm (Schanz et al. 2016) was applied to obtain Lagrangian particle tracks in the measurement volume. For each time instant, approximately 10,000 tracks were detected. Figure 14 shows a snapshot of the 3D particle tracks visualizing four successive time-steps at $\beta = 0°$. To visualize the core of the wake, only the half of the measurement volume that occupies the positive y region is shown here. As it is observed, the free stream, the shear layer and the recirculating flow in the separated zone are captured in the measurement volume.

A cyclic data collection procedure was used to improve the statistical convergence of time-resolved data required for the STB algorithm. For each yaw angle, 4 sets of 250 cycles of images were collected. The cycles were collected at 40 Hz, while each cycle consisted of 20 time-resolved images at recorded at 2.5 kHz. At the latter frequency, the maximum particle displacement in the freestream region was roughly 10 pixels between successive frames. The time-resolved images within each cycle allowed for the STB algorithm to obtain Lagrangian tracks of the particles, while the lower acquisition frequency of the cycles ensured convergence of turbulence statists. A single concurrent frame from all 1000 cycles was used for calculating the statistics, resulting in a temporal resolution of 40 Hz. Overall, the total duration of measurement using this setting was 25 s spanning over 1000 cycles. This is equivalent to approximately $1700H/U_\infty$, which is longer than the time-scale of the bi-stabilities. For obtaining the Eulerian instantaneous velocity fields, the velocity vectors of particles in each instantaneous field were binned into $30\times30\times30$ mm^3 cubes with 75% overlap. These time-resolved velocity fields were used for the proper orthogonal decomposition (POD) analysis. To obtain the mean flow statistics, the velocity vectors of the particles obtained from the 1000 frames were combined into a single velocity field that was binned into small volumes with dimensions of $15\times15\times15$ mm^3 and 50% overlap.

A second data acquisition method was also implemented for spectral analysis of the wake. For each yaw angle, 4 data sets were collected at 2.5 kHz leading to a single set duration of 2.2 s and a total duration of 8.8 s for each β. The processing of these sets was carried out in the same manner as the cyclic data, and the instantaneous particle fields were binned into $30\times30\times30$ mm^3 cubes with a 75% overlap.

The estimated uncertainties for this 3D-PTV method were 0.1 pixels along the in-plane x and z axes, and 0.2 pixels for the out-of-plane y-axis (Ebrahimian et al. 2019; Rowin et al. 2019). Using the digital resolution of 0.294 mm/pixel and the imaging frequency of 2.5 kHz, the corresponding velocity uncertainties were $0.0074U_\infty$ along the x and z axes and $0.0148U_\infty$ along the y-axis. It should also be noted that for the discussion in Chapter 4, the time averaged velocity components will be denoted by $\langle U \rangle$ for the streamwise direction, $\langle V \rangle$ for the spanwise direction, and $\langle \mathrm{W} \rangle$ for the wall-normal direction. The corresponding fluctuating velocity components will be denoted by u, v, and w.

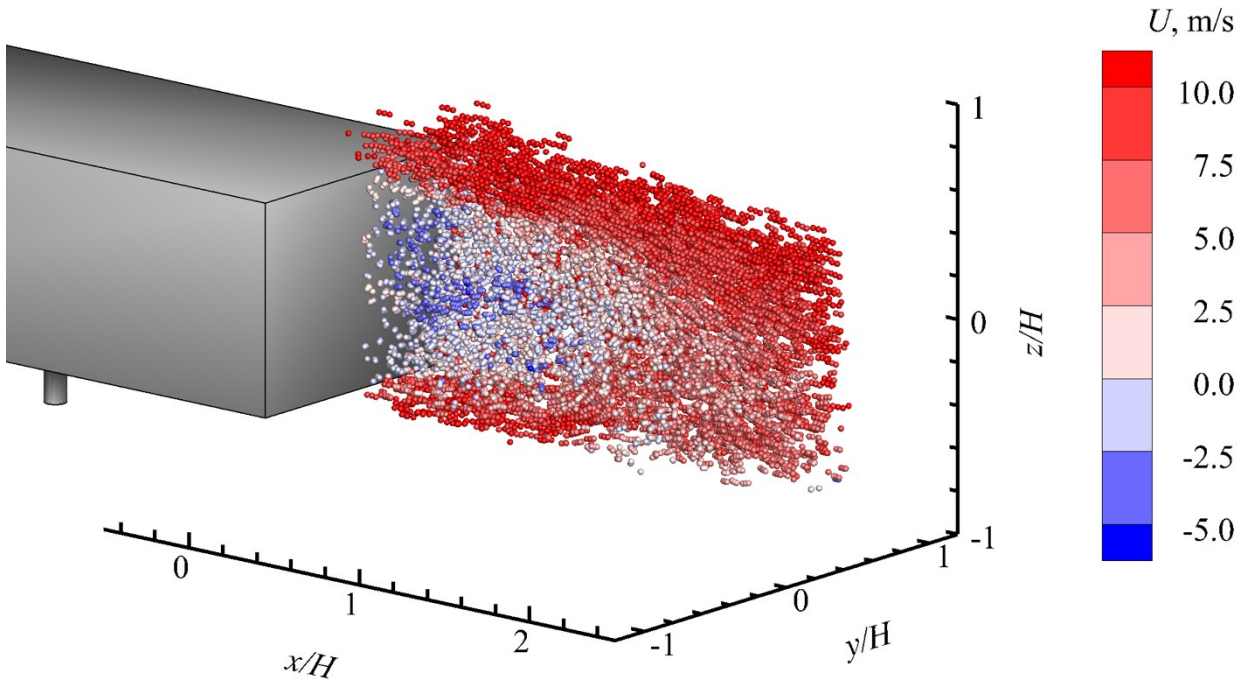

Figure 14: A visualization of particle tracers detected in four consecutive time-steps using the STB algorithm. The visualized particle field is cropped to only show particles that fall within the range of $y/H > 0$.

3.2.3 The HFSB Seeding System

As discussed in Section 2.7.2, imaging based experimental measurements rely on a high particle image contrast in-order to ensure quality measurements and contrast is highly dependent on the amount of light scattered by tracer particles. Although the amount of scatter can be increased by using lasers as an illumination source, this approach quickly reaches its limitations. Volumetric measurements also require the laser power to be spread over a much large area further reducing the illumination energy and photon count. A more effective solution is to change the size of the tracer particles since the scattered light intensity scales by the square of the particle diameter (Raffel et al. 2018).

For this reason, helium-filled soap bubbles (HFSB) were chosen as tracer particles for the 3D-PTV measurements as they are neutrally buoyant and have a diameter of approximately 0.5 mm, which is several orders of magnitude larger than the conventional ~1 µm droplets typically used

for particle tracking velocimetry (Scarano et al. 2015). The increased scattered light by HFSB tracers make it possible to carry out the 3D-PTV in volumes in the order of 1000 cm^3 or larger. The system used to generate the HFSB was developed in-house and is based on the design of Gibeau et al. (2018). The HFSB nozzles were 3D-printed orifice type nozzles as shown in Figure 15. These nozzles consist of an inner and outer body that form an internal cavity with a small orifice in the outer body. Regulated flow rates of air, helium, and soap are distributed to the nozzle through three separate supply tubes, also pictured in Figure 15. To construct the nozzles, the inner nozzle body and outer nozzle cap were 3D printed using high resolution stereolithography (SLA). The assembly of the nozzles first required the installation of the 0.0065" outer diameter 304 stainless-steel tubing which was used to connect the supply tubing. Each corresponding hole in the SLA printed nozzle pieces were first drilled out to ensure proper fitment, after which the stainless-steel tubing was glued in place using an instant-bond adhesive. A 22-gauge dispensing needle was inserted into inner nozzle body and adjusted until concentric to the stainless-steel outer tube and coincident to the outer most point of the tube. The nozzle body and cap were then joined. A buna-n O-ring was installed between the two nozzle pieces to maintain a proper seal for the internal cavity. A locking mechanism was also designed into the nozzles for consistent spacing during assembly and to keep the pieces secured to each other. Once the pieces were together, instant-bond adhesive was applied along the top joint, along the O-ring, as an extra sealing and strengthening provision. Dimensions of the fully assembled HFSB nozzle can be found in Appendix B.2.

Gibeau et al. (2020) experimentally characterized the response time of the HFSB tracers produced by these nozzles, measuring their deceleration near the stagnation point of an airfoil. The investigation found that the bubbles were neutrally buoyant on average while the standard deviation of the response time was 150 μs. The bubbles were also determined to have a mean size of approximately 400 μm and were produced at an approximate rate of 50,000 bubbles per second per nozzle. With regards to the wavelength of lasers used for these measurements (~1000 nm), these particles fall well within the Mie scattering regime, further explaining their suitability for volumetric measurements. In order to seed the large volume required for this study, the original system of Gibeau et al. (2018) was scaled up to accommodate 48 of these nozzles.

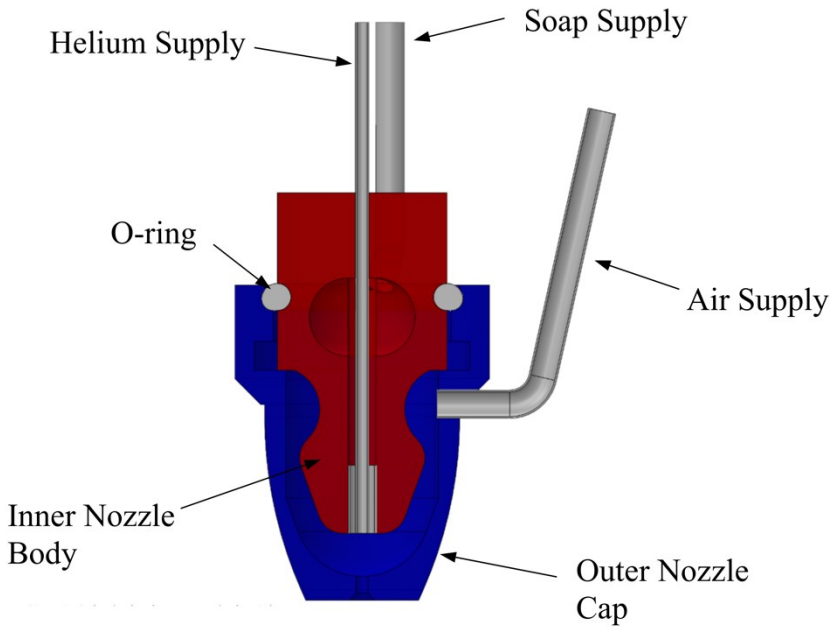

Figure 15: A cut away view of the HFSB nozzle geometry used within the 3D-PTV experiments. The nozzle consists of two separate bodies: the nozzle body and the nozzle cap. Steel tubing embedded within the nozzle geometry supply soap, air and helium.

The scaled-up system consisted of four ducts with each duct carrying 12 HFSB as can be seen in Figure 16. The nozzles pointed downward and were staggered horizontally to minimize the potential for coalescence of the bubbles. The ducts were sectioned in half so that the distance between the nozzle face and the duct floor could be controlled. This acted to minimize interference between the bubble jet and the duct as the ejection depth of the jet is dependent on the freestream velocity. The ducts were supported by two vertical stands with NACA 0012 profiles to provide streamlined housing units for the tubing. Dimensions of the fully assembled HFSB stand can be found in Appendix B.2.

Each stand was designed to house the nozzle supply tubing internally where tubing would enter through a cutaway in the bottom of the stand and would then be routed to the nozzles through slots that span the height of the stand sections. The tubing system consisted of three different configurations for each supply line (helium, air, and soap). The helium was supplied using a single initial 1/2” inner diameter PVC supply tube connected to a volumetric flow meter (Cole-Parmer RK-32907-71), supplying helium at 0.1 L/m per nozzle. The metered helium supply then passed to a symmetric circular distributor which split the line into six 1/4” inner diameter PVC supply

tubes. A secondary symmetric distributor split each 1/4” supply lines into eight more 1/8” inner diameter PVC supply tubes that were routed directly to the nozzles, counting as 48 final supply tubes in total. This tubing configuration was repeated for the air supply, with a larger flow meter (Omega FMA-LP1603A) providing 1.2 L/m of air to each nozzle. The soap supply was provided using two World Precision Instruments multi-syringe pumps (model AL-8000), each being modified to hold twelve 10 mL syringes. The syringes were tipped with barbed wye connectors that split each syringe supply into two 1/8” PVC supply tubes. The syringe pumps supplied Sage Actions Inc. 1085 bubble film solution at 36 mL/hr which equated to 18 mL/hr at each nozzle.

The stand was positioned upstream of the contraction nozzle in the settling chamber of the wind tunnel. Using hot-wire probes, Gibeau et al. (2020) measured the effect of a similar HFSB system on the test-section turbulent intensity. They observed that at a free stream velocity of U_∞ = 10 m/s, the turbulence intensity of the test section increased from 0.4% to 0.6% due to the presence of the HFSB system in the settling chamber.

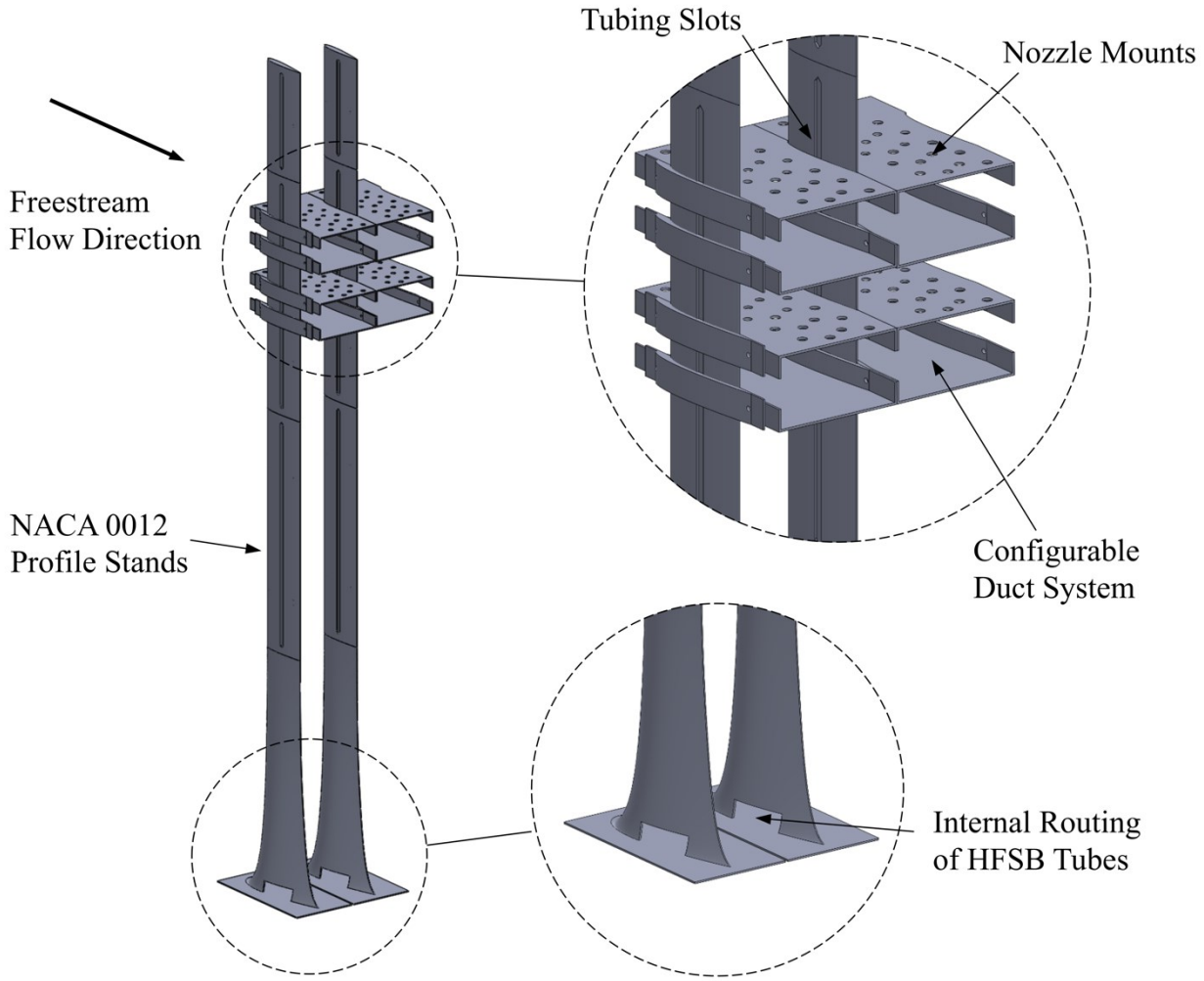

Figure 16: A schematic of the stand used within the 3D-PTV experiments to house 48 HFSB nozzles. The stand consists of four modular ducts each containing 12 in-plane HFSB nozzles. The ducts are supported by two streamlined stands that also route supply tubing for the nozzles internally.

3.3 Experiment II: Aerodynamic Loads and Passive Control

Experiment II was used to measure the aerodynamic loads for the square-back Ahmed body at yaw. Loads were measured for the baseline configuration as well as for the baseline geometry with four different passive drag reduction devices. The results from this experiment are presented and discussed in Chapter 5.

3.3.1 Aerodynamic Load Measurements

To assess the effects that yaw has on the aerodynamic loads acting on the square-back Ahmed body, force and torque measurements were taken across a yaw angle sweep of $-12.5° \leq \beta \leq 12.5°$ with measurements occurring at 2.5° yaw increments. Each measurement was repeated three times with the final results being based on the average of the three runs. All measurements were completed at a freestream speed of $U_\infty = 30$ m/s corresponding to a height-based Reynolds number of $Re_H = 2.7 \times 10^5$. To facilitate the force and torque measurements, a 6-component force and torque transducer (load cell) was integrated into the body support system as can be seen in Figure 17. The load cell was placed on a vertical shaft which was then mounted to the yaw table. The load cell was centered relative to the Ahmed body wheelbase and positioned in-between the wind tunnel floor and the boundary layer plate. Due to its mounting position, the load cell rotated with the body when the yaw angle was adjusted, meaning that the measured load components were aligned with the body's reference frame. The coordinate system location and orientation for the load cell can be seen in the cross-sectioned assembly view in the upper left of corner of Figure 17. This coordinate system is fixed to the reference frame of the body and rotates as the body is yawed. The load cell model was an ATI Industrial Automation Mini45 force and torque transducer. The Mini45 was selected based on availability but the proper calibration for the load cell was determined based on the estimated force load. A representative force load was estimated using the projected frontal area at $\beta = 12.5°$ and a coefficient of drag of $C_d = 0.35$ which equated to a drag load of ~9 N. The manufacturer calibration with the highest load sensitivity was chosen based on this load. The load cell specifications for the selected calibration (Calibration FT19593) can be seen in Table 2.

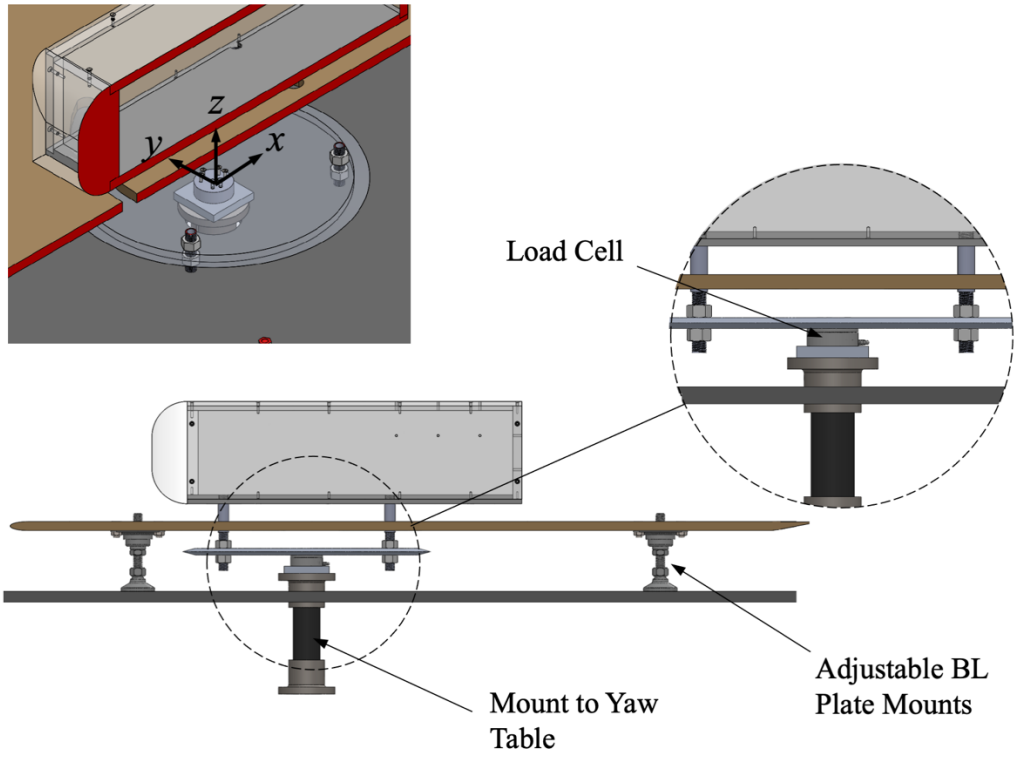

Figure 17: A schematic of the experimental setup used to collect force and load measurements for the square-back Ahmed body. A load cell used to collect the load measurements is passed through the wind tunnel floor to a yaw table using a stinger mount. The Ahmed body support structure is attached to the load cell via four support posts that pass through the boundary layer plate. A cross sectioned view of the assembly also shows the coordinate system of the load cell.

Table 2: The manufacturer specified ranges and resolutions for the 6 load components recorded by the Mini45 load cell.

	F_x, F_y	F_z	T_x, T_y	T_z
Range	145 N	290 N	5 Nm	5 Nm
Resolution	1/16 N	1/16 N	1/752 Nm	1/1504 Nm
Uncertainty	1.81 N, 1.45 N	2.18 N	0.06 Nm, 0.08 Nm	0.06 Nm

The load measurements were logged using a National Instruments data acquisition system and a LabView user interface. Several parameters were controlled to ensure the load measurements converged and accurate. Based on initial convergence studies for the load cell measurements, it was determined that the measurements were sensitive to temperature creep of both the wind tunnel

and the load cell itself. At an operating speed of 30 m/s, the temperature of the wind tunnel would increase by 6 - 7 °C during the data collection period. To minimize the effects of this drift, data collection was always initiated at a set wind tunnel temperature of 30 °C. It was also determined that because of the wind tunnel temperature variations, the load cell required a period of time within the operating temperature range before the outputs would stabilize. To control for this load cell temperature drift, a collection time of 7 minutes per case was found to allow for temperature drift to stabilize, leaving 4 minutes of converged load measurements at a frequency of 100 Hz. The collection time had the included 3 minutes buffer because the load cell temperature drift had to stabilize but the measurements had to be initiated at the same wind tunnel temperature. Figure 18 shows these effects with convergence plots for all six aerodynamic load components recorded during one zero-yaw measurement set. Each data point is the average of all the data points up to that time instance, showing the convergence means in time. From Figure 18 it is also worth noting that the F_z component did not fully converge within the collection period. This was attributed to non-stabilizing temperature drift of the load cell since the ambient temperature was the only changing variable. The resulting total duration of the useable measurements was several orders greater than the characteristic time scale for the Ahmed body wake ($\sim 17000H/U_\infty$). One last control method was the zeroing of the load cell voltage outputs at zero wind velocity. This process was completed each time the yaw angle returned to $\beta = 0°$. The wind tunnel temperature was set before the voltage output zeroing so that it was at the midpoint of the expected drift.

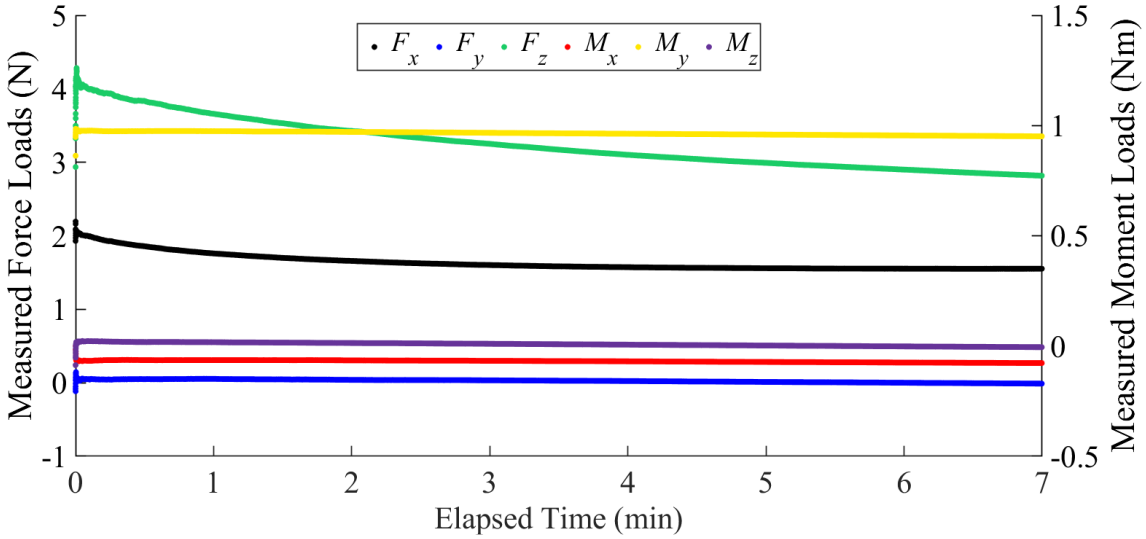

Figure 18: Convergence of load cell force and moment measurements as collection time elapsed.

3.3.2 Passive Drag Reduction Devices

The aerodynamic forces and moments at yaw were investigated for the baseline square-back Ahmed body as well as for several passive drag reduction configurations which can be seen in Figure 19. The configurations consisted of (a) a four-panel boat tail device, (b) and vertical splitter positioned at the mid span of the wake, (c) two rakes of extruded cylinders positioned at the spanwise edges of the body, and (d) two fans positioned at the upper corners of the rear face, blowing downwards. The boat tail device or similar cavity type devices have been used previously as drag reduction mechanisms and have been shown to be effective (Khalighi et al. 2012; Schmidt et al. 2018; Bonnavion et al. 2019; Lorite-Díez et al. 2020). The vertical splitter plate was suggested based on the yawed flow field features identified within Chapter 4. A strong spanwise flow was present along the rear face of the body at yaw and the vertical splitter plate was conceived to disturb this spanwise crossflow. This could potentially cause a perturbation to the flow field with a very small change in geometry. The splitter was positioned along the vertical symmetry plane of the rear face and extended 25 mm downstream. The cylinder rakes along the spanwise edges were intended to increase mixing of the shear layers and the separated region at yaw. Five cylinders with 10 mm diameters were uniformly distributed along each edge, the cylinders extended 10 mm downstream. Finally, the fan setup was theorized as a way to infuse momentum

into the separated region by means of an external power source and would act as an initial validation of the idea. This method is considered passive within the context of this study since there are no mechanisms or algorithms in place that actively measure and control the wake. The setup had two 60 mm 40 CFM fans (Bgears b-Blaster 60) located at the top two corners of the rear face, blowing downwards. Technical drawings for all manufactured drag reduction devices can be found in Appendix B.3.

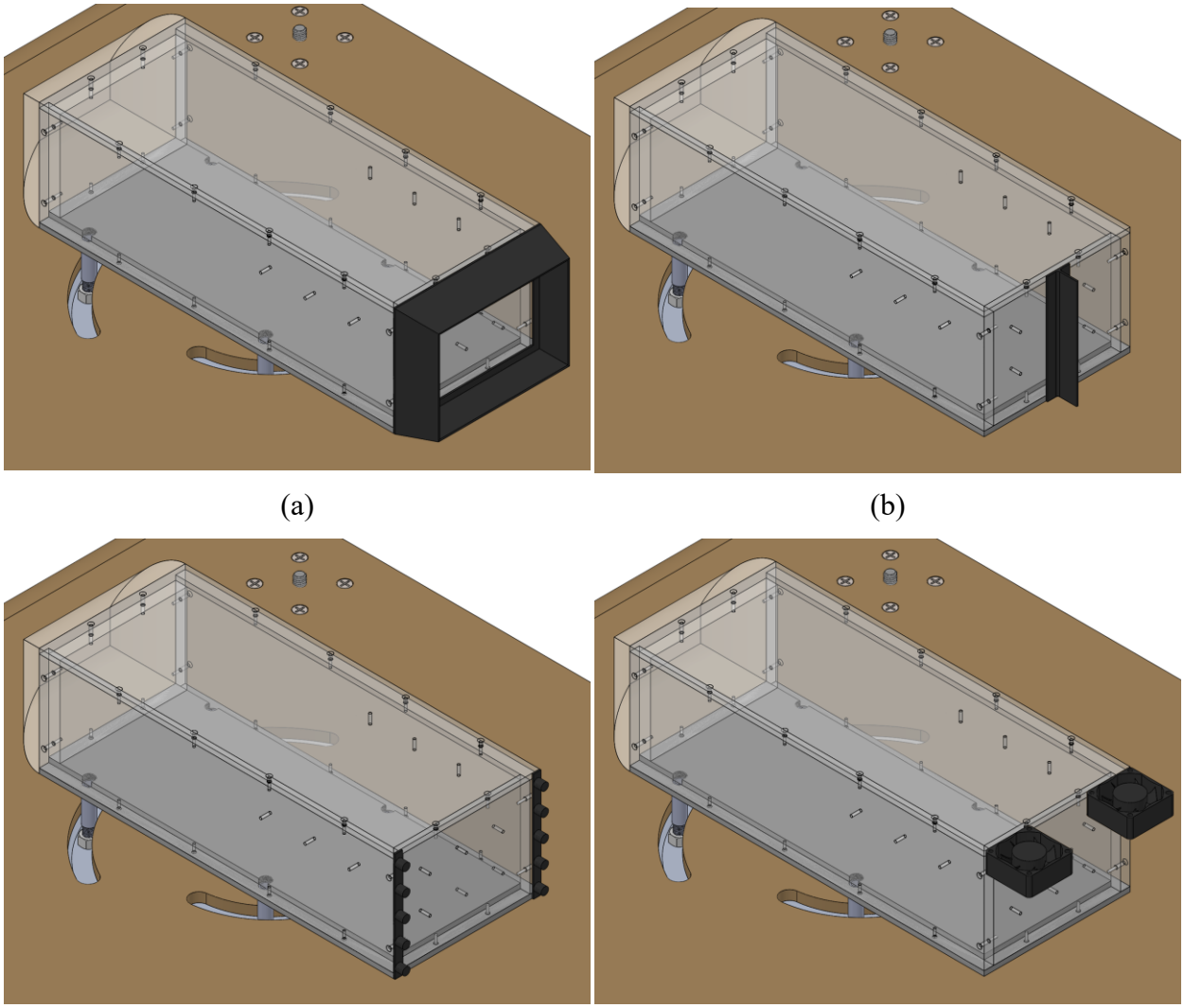

(a) (b)

(c) (d)

Figure 19: Models of the four passive drag reduction devices tested. The drag reduction devices consist of (a) a four-panel boat tail, (b) a vertical splitter located at the mid-span of the rear face, (c) two rakes of cylinders place along the spanwise edges of the rear face, and (d) two fans located at the top corners of the rear faces, with positive flow being directed downward.

3.3.3 Aerodynamic Loading Coordinate Systems and Coefficients

All of the load measurements are reported in terms of their respective non-dimensionalized coefficients. The coefficients were calculated according to Equation 22 for the force measurements:

$$C_i = \frac{2F_i}{\rho U_\infty A} \tag{22}$$

and Equation 23 for the measured moments:

$$C_{Mi} = \frac{2M_i}{\rho U_\infty A l}. \tag{23}$$

The force coefficients were based on the model frontal area, A = 0.028 m^2, an air density of ρ = 1.164 kg/m^3, and the freestream velocity, U_∞ = 30 m/s. Moment coefficients were also calculated using these parameters, along with a characteristic length, l, of 0.235 m which is the wheelbase length, the streamwise distance between support posts.

The coefficients are reported with respect to two different coordinate systems that are pictured in Figure 20. The first reference frame, Figure 20(a), will be referred to as the body-indexed reference frame and is always aligned with the axes of the body. It represents the forces and moments a vehicle would experience in crossflow conditions. The second reference frame, Figure 20(b), is the wind-indexed reference frame and is always aligned with the freestream direction or the body reference frame at zero-yaw. Both reference frame origins are centred between the four support posts, similar to the load cell itself, and are at the mid-height of the body. Since the load cell was fixed to the body-indexed reference frame, it is the native reference frame, and the measurements are corrected after collection to align with the wind-indexed reference frame. As can also be seen in Figure 17, some of the support structure between the Ahmed body and the load cell was below the boundary layer plate but was also still exposed to the freestream and therefore contributed to the load measurements. To account for this effect, the portions of the body and support structure above the boundary layer plate were blocked from the freestream flow and measurements were then taken for all of the yaw cases. This resulted in force and moment system corrections for the setup that were subtracted from all other experimental measurements.

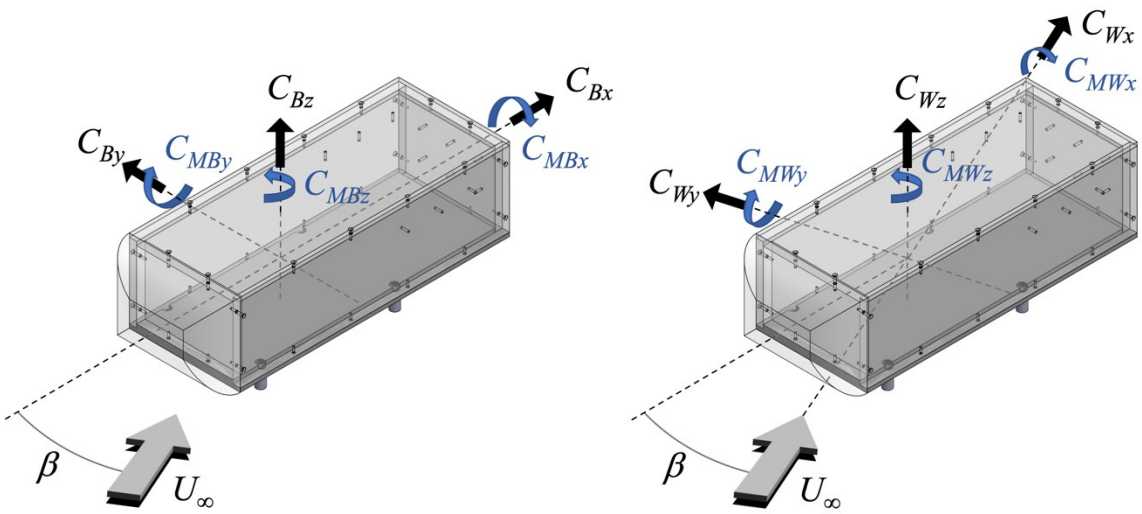

(a) (b)

Figure 20: Diagrams showing the two coordinate reference frames used during the analysis of the drag reduction devices. The first coordinate system (a) is the body-indexed reference frame, staying orthogonal to the body axes, the second (b) is the wind-indexed reference frame which remains aligned with the zero-yaw body-indexed reference frame.

The correction process of the measured forces for the body-indexed cases can be seen in Equation 24(a)-(c):

$$\begin{aligned} &\text{(a)} \quad F_{Bx} = F_{Lx} - F_{Cx} \\ &\text{(b)} \quad F_{By} = F_{Ly} - F_{Cy} \\ &\text{(c)} \quad F_{Bz} = F_{Lz} - F_{Cz} \end{aligned} \tag{24}$$

where F_{Bi} denotes the body-indexed force, F_{Li} the load cell measured force, and F_{Ci} the measured force for the supporting system (correction term). The correction process for the corresponding body-indexed moments can be seen in Equation 25(a)-(c):

$$\begin{aligned} &\text{(a)} \quad M_{Bx} = M_{Lx} - M_{Cx} - F_{By}L_V \\ &\text{(b)} \quad M_{By} = M_{Ly} - M_{Cy} - F_{Bx}L_V \\ &\text{(c)} \quad M_{Bz} = M_{Lz} - M_{Cz} \end{aligned} \tag{25}$$

where M_{Bi} denotes the body-indexed moment, M_{Li} the load cell measured moment, M_{Ci} the measured system moment correction, and L_V is the vertical distance between the load cell center

plane and the reference frame origin (0.235 m). The z-axis moment did not need to account for a vertical shift since the load cell z-axis was the same as the body-indexed z-axis.

Similarly, the correction process of the measured forces for the wind-indexed cases can be seen in Equation 26(a)-(c):

$$\begin{aligned} &\text{(a)} \quad F_{Wx} = F_{Lx}\cos(\beta) - F_{Ly}\sin(\beta) - F_{Cx}\cos(\beta) + F_{Cy}\sin(\beta) \\ &\text{(b)} \quad F_{Wy} = F_{Ly}\cos(\beta) + F_{Lx}\sin(\beta) - F_{Cy}\cos(\beta) - F_{Cx}\sin(\beta) \\ &\text{(c)} \quad F_{Wz} = F_{Lz} - F_{Cz} \end{aligned} \tag{26}$$

where F_{Wi} denotes the wind-indexed force. The correction process for the corresponding wind-indexed moments, M_{Wi}, can be seen in Equation 27(a)-(c):

$$\begin{aligned} &\text{(a)} \quad M_{Wx} = M_{Lx}\cos(\beta) - M_{Ly}\sin(\beta) - M_{Cx}\cos(\beta) + M_{Cy}\sin(\beta) - F_{Wy}L_V \\ &\text{(b)} \quad M_{Wy} = M_{Ly}\cos(\beta) + M_{Lx}\sin(\beta) - M_{Cy}\cos(\beta) - M_{Cx}\sin(\beta) - F_{Wx}L_V \\ &\text{(c)} \quad M_{Wz} = M_{Lz} - M_{Cy}. \end{aligned} \tag{27}$$

Chapter 4: Characterization of the Square-Back Wake at Yaw

This chapter will present the results of Experiment I (Section 3.2) with the intention of identifying and characterizing the effects of yaw on the wake of the square-back Ahmed body. First the time-averaged wake structures for the yaw angles of $\beta = 0°$, 5°, and 10° will be described in Section 4.2, followed by analysis of the Reynolds stresses within the wake in Section 4.3. Upon establishing the descriptions of the time-averaged wake at both zero-yaw and yaw, the time-averaged vortex structures within each wake are then described in Section 4.4. Characterization of the spectral characteristics of the wake are discussed in Section 4.5. Finally, the coherent motions within the wake are studied using a proper orthogonal decomposition based analysis in Section 4.6.

4.1 Identification of Bi-Stable Modes

To characterize the square-back Ahmed body at yaw, the zero-yaw condition first had to be set properly. As discussed in Section 3.2.1, the criteria used to set the zero-yaw condition would be identification of both bi-stable modes within the wake. Doing so would be proof that the yaw angle was within the range of $|\beta| < 1°$, which was deemed acceptable based on the low resolution of the yaw table. Verification of the proper zero-yaw condition according to this criterion can be seen in Figure 21, where the two bi-stable modes that were extracted from the 2D-PIV measurements are shown. It shows two time-averaged samples of the wake, averaged over subsets of 72 frames which is equivalent to the expected mean duration of one bi-stable mode ($TU_\infty/H = 420$). A switching of the lateral symmetry is apparent, most notably seen in the location of the upstream recirculating vortex as it switches between Vortex #1 and Vortex #2.

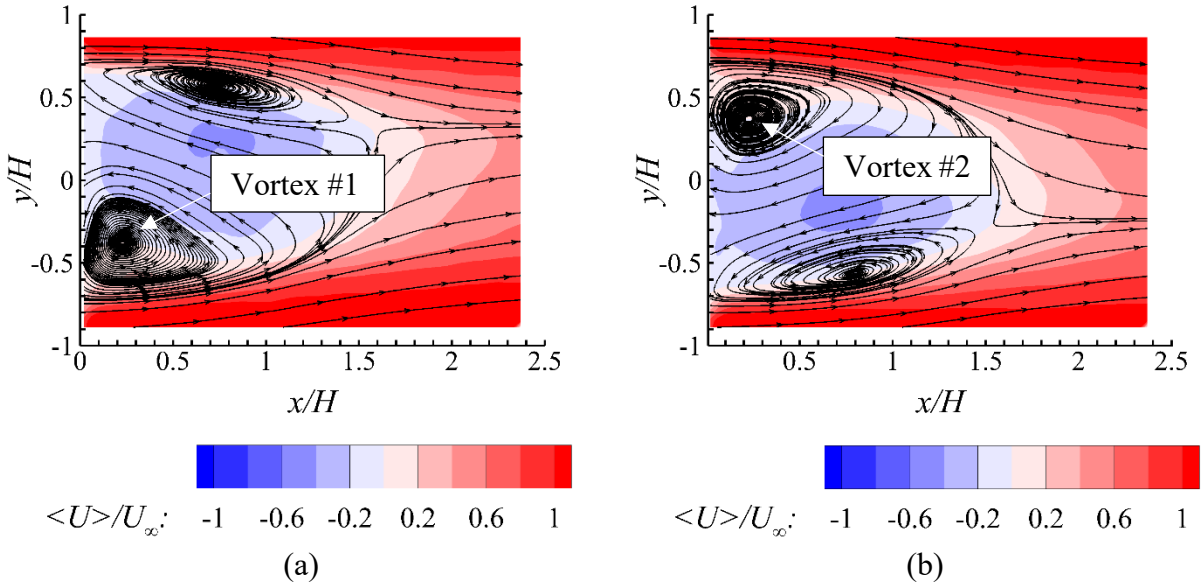

Figure 21: Flow fields resulting from the averaged 2D-PIV measurements taken across the span of the wake at the mid-height. Contours of streamwise velocity are shown with 2D streamlines overlayed. The existence of two distinct but opposite wake modes (a) and (b) can be seen within the in-plane streamlines.

4.2 Time-Averaged Velocity Fields

The wake characterization begins with the descriptions of the mean flow field for all three yaw cases. The mean velocity field of the $\beta = 0°$ case acts as a reference for analyzing the effects of crossflow and is shown in Figure 22. In Figure 22(a), (b), and (c), 3D isosurfaces of $\langle U \rangle / U_\infty = 0$, $\langle V \rangle / U_\infty = \pm 0.1$, and $\langle W \rangle / U_\infty = \pm 0.1$ are shown, respectively. Figure 22(d) and (e) show in-plane streamlines and contours of $\langle U \rangle / U_\infty$ and $\langle V \rangle / U_\infty$ at the $z/H = 0$ plane, respectively, while Figure 22(f) shows in-plane streamlines and contours of $\langle W \rangle / U_\infty$ across the $y/H = 0$ plane. I will refer to the region enclosed by the $\langle U \rangle / U_\infty = 0$ isosurface in Figure 22(a) as the separation bubble. The separation bubble appears relatively symmetric and elongated in the streamwise direction. In the 2D slice of Figure 22(d), the region of recirculating streamlines, which will be named the recirculation bubble, extends to $x/H = 1.5$, which is consistent with the experimental observations of Grandemange et al. (2013b) also made at $Re_H = 9.2 \times 10^4$. The streamlines also show a slight asymmetry between the two recirculation regions, which is attributed to the imbalanced of one of

the bi-stable states in the mean flow field (Volpe et al. 2015) and is caused by limitations in the yaw resolution..

The isosurfaces of $\langle V \rangle / U_\infty = \pm 0.1$ in Figure 22(b) are relatively equal in size and positioned symmetrically. The exception is a small isosurface of $\langle V \rangle / U_\infty = -0.1$ close to the base of the Ahmed body, for which a positive counterpart is not visible. Inspection of $\langle V \rangle$ contours in Figure 22(e) shows that a region of positive $\langle V \rangle$ exists close to the base at $y/H > 0$ but with a smaller magnitude. In general, Figure 22(e) demonstrates a relative symmetry of the spanwise mean flow with respect to $y/H = 0$ plane. The isosurfaces indicate that zones of large $\langle V \rangle$ are located further downstream at approximately $x/H = 1.2$ where streamlines curved around the separation bubble.

The isosurfaces of $\langle W \rangle / U_\infty = \pm 0.1$ in Figure 22(c) and contours of Figure 22(f) show a large zone of downward motion from the top edge of the Ahmed body and smaller zone of upward motion on the bottom edge. This asymmetry is due the ground plane, limiting the flow underneath the Ahmed body. As discussed by Rouméas et al. (2009) and Grandemange et al. (2013a; 2015), the increased flow from overtop of the body compensates for the restricted flow from underneath. Streamlines in Figure 22(f) show the maximums of wall-normal velocity are located outside of the separation bubble where the streamlines curvature is large. Two large vortices are also seen in the wall-normal cross-section of the recirculation bubble.

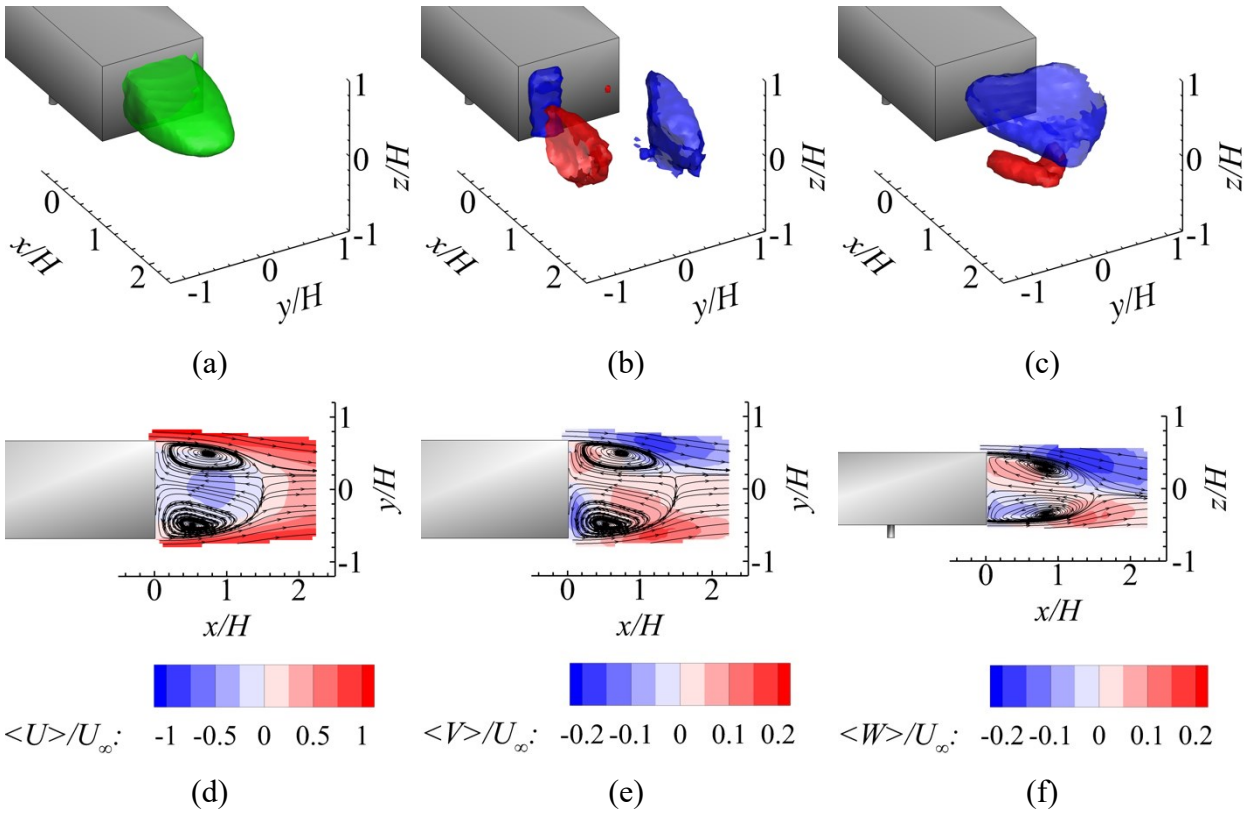

Figure 22: Visualization of the mean velocity components for the $\beta = 0°$ case. (a) The green isosurface shows $\langle U \rangle / U_\infty = 0$, (b) the red isosurface corresponds to $\langle V \rangle / U_\infty = 0.1$ and the blue indicates $\langle V \rangle / U_\infty = -0.1$. (c) The red isosurfaces corresponds to $\langle W \rangle / U_\infty = 0.1$ and blue to $\langle W \rangle / U_\infty = -0.1$. The slices show (d) contours of $\langle U \rangle / U_\infty$ at the $z/H = 0$ plane, (e) $\langle V \rangle / U_\infty$ contours also at the $z/H = 0$ plane, (f) and $\langle W \rangle / U_\infty$ contour at the $y/H = 0$ plane.

The effects of yaw on the time-averaged flow field are investigated for $\beta = 5°$ in Figure 23. The presentation of the results in Figure 23 is consistent with Figure 22. The $\langle U \rangle / U_\infty = 0$ isosurface in Figure 23(a) is asymmetric with respect to $y/H = 0$ plane, with the bulk of the separation bubble being positioned on the windward side of the wake. This separation bubble has a streamwise length of $x/H = 1.5$ which remains consistent with the zero-yaw case.

The velocity distributions in Figure 23(b) and (e) show a large increase in positive spanwise flow from the leeward side of the wake. Two zones of negative spanwise velocity are identified, one located along the rear face and one downstream along the windward side of the wake. The negative zone on the rear face is larger than the similar one observed in the zero-yaw wake. The

3D isosurface in Figure 23(b) shows that the positive spanwise velocity is strongest on the leeward side and along the mid-height of the wake. The two regions of negative spanwise velocity extend primarily along the z direction. Streamlines across the spanwise xy-plane in Figure 23(d) and (e) show a large recirculating vortex forming on the leeward side of the rear face, while a smaller recirculating vortex is seen further downstream on the windward side.

The isosurfaces of $\langle W \rangle$ in Figure 23(c) show that both the zones of positive and negative velocity have become larger relative to the zero-yaw case. The primary region of negative wall-normal velocity is now asymmetric with respect to $y/H = 0$ plane, being larger on the leeward side. The magnitude of the wall-normal velocity component is also significantly stronger as seen when comparing Figure 23(f) with Figure 22(f). The positive $\langle W \rangle$ isosurface is still smaller than the negative $\langle W \rangle$ component and is positioned on the lower half of the wake, close to the end of the recirculation bubble. Streamlines in Figure 23(f), which are on a plane located at the midspan of the rear face, show two recirculation regions along the top and bottom, similar in arrangement to the zero-yaw case but with the top recirculation being smaller and shifted slightly downstream in comparison.

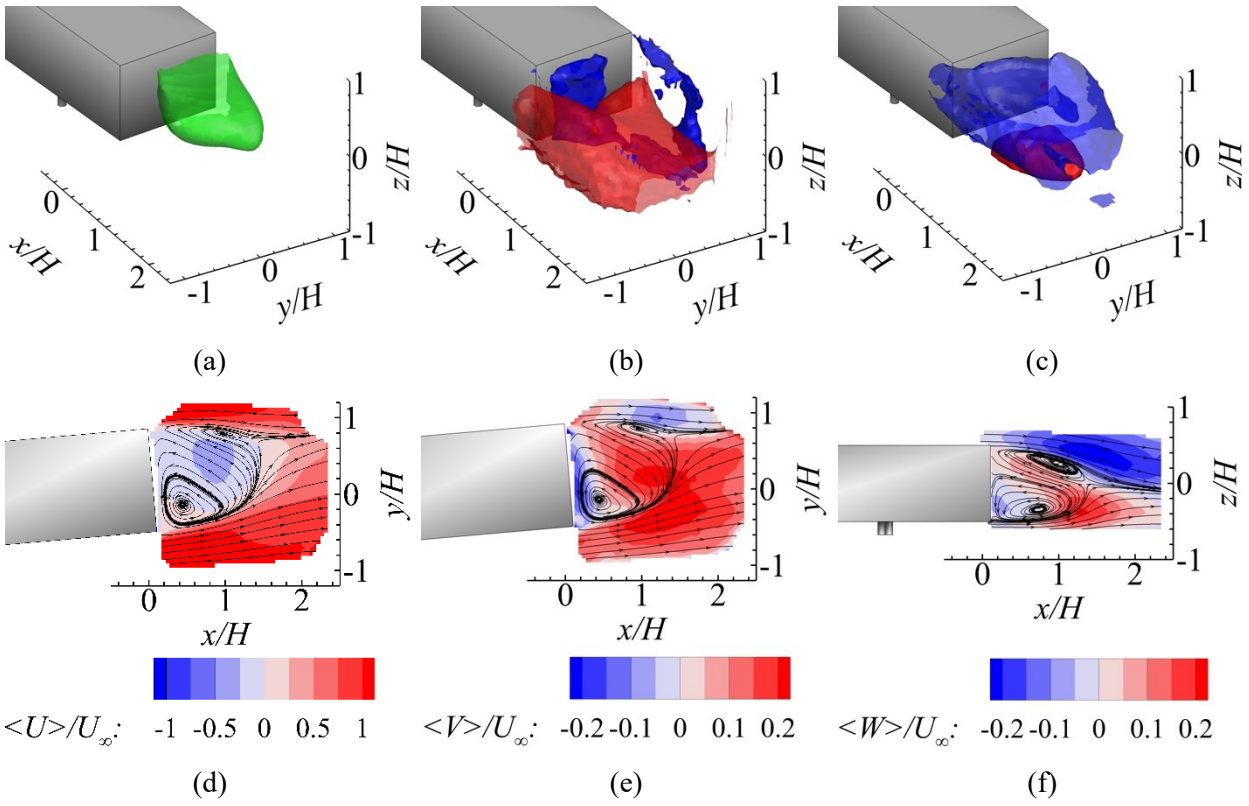

Figure 23: Visualization of the mean velocity components for the $\beta = 5°$ case. (a) The green isosurface shows $\langle U \rangle / U_\infty = 0$, (b) the red isosurface corresponds to $\langle V \rangle / U_\infty = 0.1$ and the blue indicates $\langle V \rangle / U_\infty = -0.1$. (c) The red isosurfaces corresponds to $\langle W \rangle / U_\infty = 0.1$ and blue to $\langle W \rangle / U_\infty = -0.1$. The slices show (d) contours of $\langle U \rangle / U_\infty$ at the $z/H = 0$ plane, (e) $\langle V \rangle / U_\infty$ contours also at the $z/H = 0$ plane, and (f) the $\langle W \rangle / U_\infty$ contours at the $y/H = 0.184$ plane.

The isosurface of $\langle U \rangle / U_\infty = 0$ for $\beta = 10°$ in Figure 24(a) is asymmetric across the span of the wake and favours the windward region, similar to Figure 23(a). It is worth note, however, that the size of the separation bubble is smaller, evident in a 7% smaller spanwise width relative to the $\beta = 5°$ case, as well as in a reduced separation bubble length of $x/H = 1.4$. The flow patterns inferred by the isosurfaces and in-plane velocity plots in Figure 24 remain consistent with the descriptions of the $\beta = 5°$ flow patterns discussed before. Effects of increasing yaw are evident in the larger velocity magnitudes for both the spanwise and wall-normal velocity components.

The comparison between the three cases of $\beta = 0°$, 5°, and 10° showed a large increase in the strength of positive spanwise and negative wall-normal motions as yaw angle increased.

Increasing the yaw angle also resulted in a shorter recirculation bubble and significantly increased the asymmetry of the wake along the spanwise axis. The latter effect was observed because of a stronger leeward recirculating vortex.

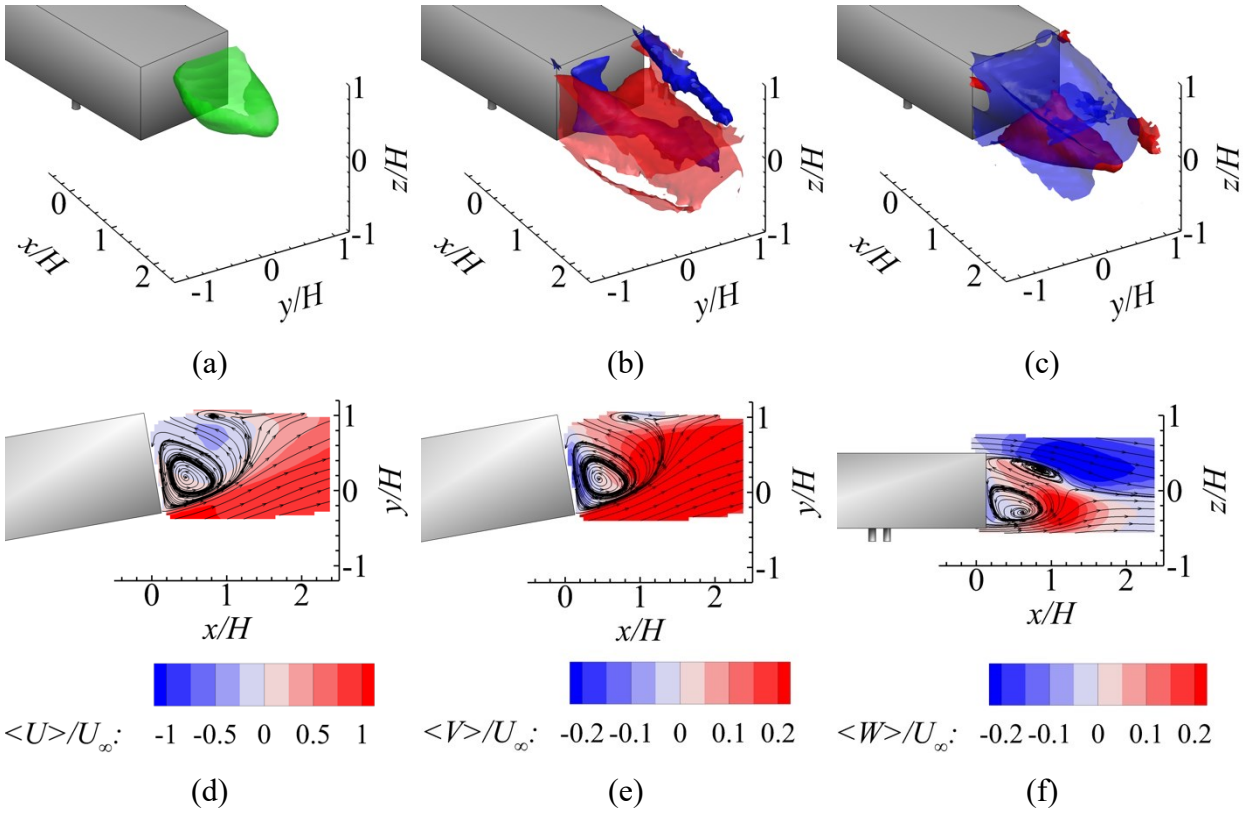

Figure 24: Visualization of the mean velocity components for the β = 10° case. (a) The green isosurface shows $\langle U \rangle / U_\infty$ = 0, (b) the red isosurface corresponds to $\langle V \rangle / U_\infty$ = 0.1 and the blue indicates $\langle V \rangle / U_\infty$ = -0.1. (c) The red isosurfaces corresponds to $\langle W \rangle / U_\infty$ = 0.1 and blue to $\langle W \rangle / U_\infty$ = -0.1. The slices show (d) contours of $\langle U \rangle / U_\infty$ at the z/H = 0 plane, (e) $\langle V \rangle / U_\infty$ contours also at the z/H = 0 plane, and (f) $\langle W \rangle / U_\infty$ contours at the y/H = 0.366 plane.

4.3 Reynolds Stresses

Isosurfaces of the streamwise Reynolds stress for $\langle u^2 \rangle / U_\infty{}^2 = 0.05$ are investigated in Figure 25. Across all three cases, the locations of the isosurfaces are consistent with shear layers forming along the perimeter of the rear face (Grandemange et al. 2013b; Li et al. 2019). The isosurface structure of the zero-yaw case is approximately symmetric with respect to $y/H = 0$ and $z/H = 0$ planes with the stress distributions slowly converging toward the center of the wake. The effects of yaw can be assessed in Figure 25(b) and (c), where the isosurface of $\langle u^2 \rangle$ along the leeward side of the body becomes smaller and $\langle u^2 \rangle$ along the upper, lower, and windward sides increase in size.

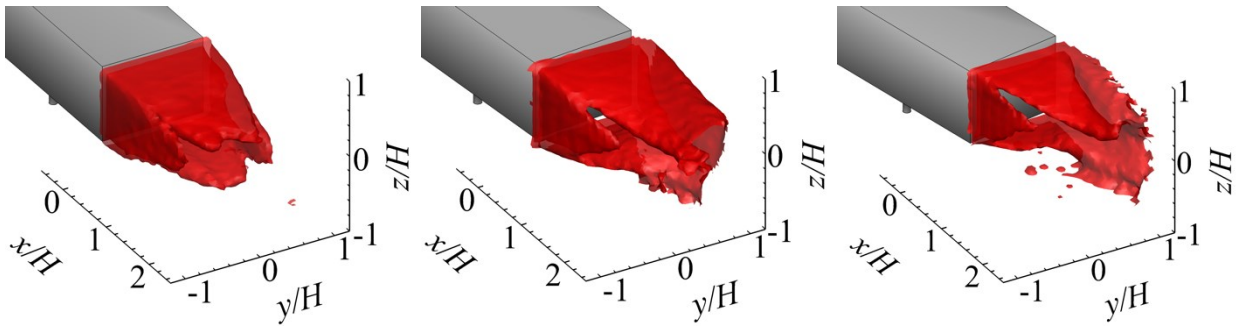

Figure 25: Isosurfaces of streamwise Reynolds stress at $\langle u^2 \rangle / U_\infty{}^2 = 0.05$ for yaw angles of (a) $\beta = 0°$, (b) $\beta = 5°$, and (c) $\beta = 10°$.

Isosurfaces of the two Reynolds shear stress components are investigated in Figure 26. The three plots in the top row correspond to $\langle uv \rangle / U_\infty{}^2$ while the three on the bottom row correspond to $\langle uw \rangle / U_\infty{}^2$. The isosurfaces of $\langle uv \rangle$ for the zero-yaw case are predominantly distributed along the spanwise limits of the recirculation bubble, tapering slightly as they extend downstream. The negative and positive component distributions are symmetric and both isosurfaces have small inward bulges centered at the mid-height of the wake. The $\langle uv \rangle$ isosurfaces for $\beta = 5°$ in Figure 26(b) are asymmetric; the leeward isosurface is smaller and has a wall-normal tapering while the windward isosurface is larger and expands in the wall-normal direction. Two smaller isosurfaces of positive and negative $\langle uv \rangle$ also extend downstream from the top edge and one positive $\langle uv \rangle$

isosurface extends along the bottom of the wake, all of them favoring the windward side. The positive isosurface extending from the top edge suggests a vortex like structure that originates at the rear face. The isosurface extending along the bottom of the wake is more centered along its span and is position further downstream of the rear face. Figure 26(c) shows that the increase in yaw angle to $\beta = 10°$, increases the tapering of the positive $\langle uv \rangle$ distribution along the leeward side. No tapering is observed for the negative $\langle uv \rangle$ isosurface. The small isosurfaces extending along the top and bottom of the wake are again present and slightly larger in size compared to the $\beta = 5°$ case.

Figure 26(d)-(f) show $\langle uw \rangle$ isosurfaces for each yaw case, all of them extending downstream from the top and bottom edges of the rear face. For the zero-yaw case, the negative $\langle uw \rangle$ isosurface is distributed over a larger area and has a greater peak magnitude relative to the positive isosurface. When the yaw angle increases to $\beta = 5°$, the $\langle uw \rangle$ distributions become asymmetric also along the span of the wake. The wall-normal extent of the isosurfaces is greater on the windward side of the wake. The leeward sides of the $\langle uw \rangle$ isosurfaces also taper inwards towards the center. With the increase to $\beta = 10°$, the small positive $\langle uw \rangle$ isosurface on the leeward edge extends in the streamwise direction. This again suggets the existence of a vortex extending downstream from the top leeward. Aside from this noted difference, the $\langle uw \rangle$ distributions for $\beta = 10°$ remain similar to those described for $\beta = 5°$.

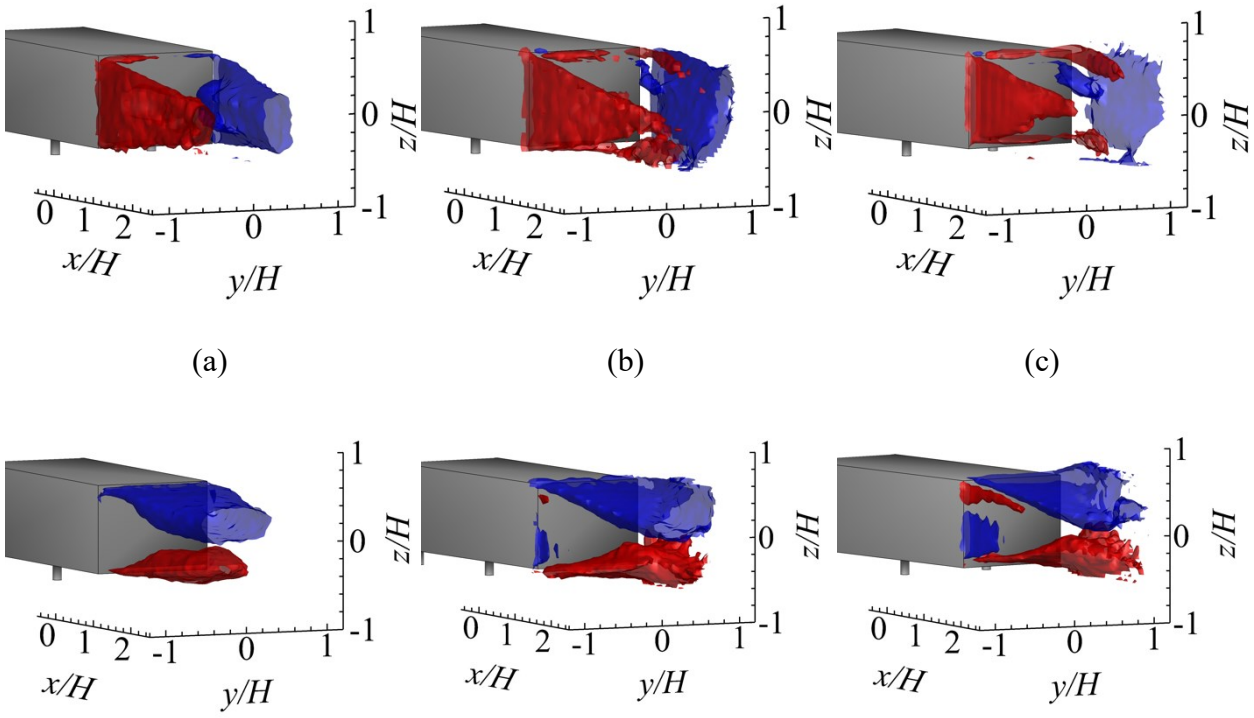

Figure 26: Isosurfaces of streamwise-spanwise Reynolds stress $\langle uv \rangle / U_\infty^2$ = +0.01 (red) and $\langle uv \rangle / U_\infty^2$ = -0.01 (blue) for the yaw angles of (a) β = 0°, (b) β = 5°, and (c) β = 10°. The streamwise-wall-normal Reynolds stress is visualized using isosurfaces of $\langle uw \rangle / U_\infty^2$ = +0.01 (red) and $\langle uw \rangle / U_\infty^2$ = -0.01 (blue) for (d) β = 0°, (e) β = 5°, and (f) β = 10°.

4.4 Time-Averaged Vortex Structures

4.4.1 Vortex Centerline Identification

The volumetric data obtained for the wake in this study also allowed for the identification of 3D vortex structures within the mean flow. Vortex filaments are identified using the critical-point theory described by Sujudi and Haimes (1995), which was covered in more detail in in Section 2.9.1. This method has been effectively used in similar bluff body studies (Östh et al. 2012; Zhu et al. 2017). The vortex centers that are shown in the current investigation were confirmed to be physical by visual inspection of the 3D streamlines. The 3D streamlines are omitted here for

clarity of the figures. All of the vortex center lines can be seen in Figure 27 along with the respective $\langle U \rangle / U_\infty = 0$ isosurfaces for each case to give spatial context. The vortex center line for the zero-yaw case is shown by a thick overlayed red line in Figure 27(a) to make visual identification easier. The vortex filament indicates the presence of a ring vortex (RV) that is always coincident to the $\langle U \rangle / U_\infty = 0$ isosurface. The ring is centered at approximately $x/H = 0.71$ and is shifted slightly downstream at the midspan. This vortex structure is consistent with the toric structure reported in previous studies (Khalighi et al. 2001; 2012; Krajnović et al. 2003; Rouméas et al. 2009; Perry et al. 2016).

The vortex filaments for the $\beta = 5°$ case, shown in Figure 27(b), also form a ring vortex (RV) that is this time skewed. The portion of the vortex filament on the leeward side is positioned further upstream relative to the rest of the filament. The vortex filaments without the thick overlays did show some small discontinuities. These could be due to lower vortex strength or measurement noise propagating to the spatial derivatives of velocity field, which would affect the vortex centerline identification method. The cause of these discontinuities is credited to limitations in this method and are not suggested to be physical discontinuities. Even with the slight fragmentation, the overall continuation remained distinguishable for a qualitative analysis. Also worth noting is that this ring vortex is similar to the skewed torus that was previously identified for a single symmetry-breaking mode of the zero-yaw (Lucas et al. 2017; Dalla Longa et al. 2019). This commonality could suggest that the skewed vortex ring is a progression of the skewed instantaneous torus of the zero-yaw case. In addition to the main vortex ring, two streamwise vortex cores (SV1 and SV2) are also noted on the windward side of the body, extending downstream from the vortex ring. Vortex core SV1 is positioned above vortex core SV2.

Figure 27(c) shows the identified vortex filaments for the $\beta = 10°$ case. A ring vortex (RV) like structure is again identified and stretches in the wall-normal direction on the leeward side and then bends along the top and bottom of the separation bubble toward the windward side. The vortex ring does not close on the windward side, suggesting that the strength of the vortex filament in this region decreases as the yaw angle increases. A weak vortex does however still exist on the windward side as can be verified by the streamlines in Figure 24(d). The streamwise filaments (SV1 and SV2) identified in the $\beta = 5°$ case are also present and slightly longer. Finally, two new vortex filaments are observed, one at the top-windward corner (SV3) and one on the leeward side of the separation bubble (SV4).

There is significant overlap between these vortex filaments and the vortex structures that were suggested by the Reynolds stress distributions in Figure 26, further supporting the proposed vortex topology. The extensions identified along the top of the wake in Figure 26(b) and (c) overlap well with the SV1 and SV3 vortices. Similarly, the extension that is positioned along the bottom of the wake in Figure 26(b) and (c) is consistent with the SV2 vortex. Finally, the effects of the SV4 vortex can be identified in the Reynolds stress isosurfaces of the $\beta = 10°$ case in Figure 26(f).

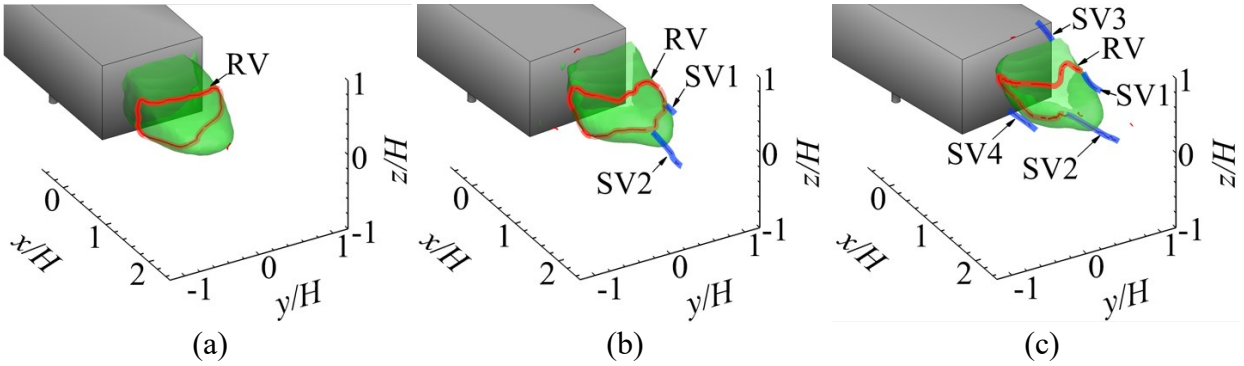

Figure 27: Vortex centerlines identified within the wake at the yaw angles of of (a) $\beta = 0°$, (b) $\beta = 5°$, and (c) $\beta = 10°$. Vortex centerlines are differentiated based on color where red lines identify the ring vortex structure (RV), and blue lines identify streamwise vortex structures (SV).

4.4.2 Q-criterion Vortex Identification

Distributions of Q-criterion within the wake were also calculated for all three yaw cases as a secondary method of vortex identification. The results are visualized using isosurfaces of Q-criterion and can be seen in Figure 28. The isosurface values are different and were selected based on how well they showed vortex structures. The isosurfaces are also all overlayed with contours of normalized streamwise vorticity. Background theoretical context for Q-criterion was given in Section 2.9.2. Beginning with the zero-yaw case in Figure 28(a), the Q-criterion isosurface shows a ring like structure that forms along the perimeter of the rear face to the inside of the wake. This structure closely matches the description of the ring vortex identified in Figure 27(a), even sharing the downstream shift of the ring vortex along the midspan of the wake. The Q-criterion isosurface also extends from the perimeter to the proposed location of the ring vortex. These extensions are

consistent with the shear layers the develop around the perimeter of the recirculation region in the wake. The contours of streamwise vorticity in Figure 28(a), appear approximately symmetric as is expected for the zero-yaw wake and are small in magnitude. No sections of the ring vortex are aligned with the streamwise axis making the contours consistent with the identified structure.

Figure 28(b) shows the Q-criterion isosurfaces for $\beta = 5°$ case. A large ring like structure can be identified again based on the location of the most downstream segments of the isosurface. The isosurface is also thickest along location of the ring vortex. The leeward side of the isosurface is positioned further upstream which is consistent with the ring vortex topology identified in Figure 27(b). The contours of streamwise vorticity help to confirm or reveal several more features of the coherent vortex structures. The positive streamwise vorticity magnitude is high on the most downstream portion of the isosurface on the leeward side where the ring vortex from Figure 27(b) would be located. The ring vortex in Figure 27(b) was skewed downstream in this section, becoming more aligned with the streamwise axis which matches these vorticity contours. The sign of the vorticity contours is consistent with the expected rotation of the ring vortex, turning the flow from the shear layers towards the center of the wake. The vorticity contours also show three more high vorticity regions. The first is a high positive vorticity region at the top windward corner of the wake which is matches the SV3 vortex structure proposed previously, stemming from the top windward corner. The second is a high positive vorticity section slightly downstream where the SV1 vortex was identified. Finally, the third is a high negative vorticity region in the lower half of the wake, closer to the windward side. It is consistent with the SV2 vortex. The signs of the vorticity contours also help specify the rotation of these three vortices structures: the rotation being clockwise for SV1 and SV3 and counter clockwise for SV2.

The Q-criterion isosurfaces for the last yaw case of $\beta = 10°$ in Figure 28(c) show a significant progression over the previous. Downstream portions of the isosurfaces again align with the spatial distribution of the ring vortex in Figure 27(c). Similar to the $\beta = 5°$ case, streamwise vorticity contours are large where the ring vortex is aligned with the streamwise axis. The isosurface is also present on the windward side of the wake where the vortex centerlines in Figure 27(c) were broken. The ring vortex continuity on the windward side is therefore further implied by the Q-criterion analysis. The isosurfaces also show the presence of two streamwise extensions which again account for the SV1 and SV2 vortices from Figure 27(c). The extensions are much larger than those of Figure 28(b), even with the larger isosurface value for Figure 28(c). This

implies a large increase in the strength of the SV1 and SV2 vortices as yaw angle increases. A long streamwise extension is then identified on the leeward side, stemming from the top corner, which matches the location of streamwise vortex SV4. The vorticity magnitude indicates that this vortex structure has a clockwise rotation. Lastly, as was seen in Figure 28(b), the SV4 structure is not clearly identified in the Q-criterion isosurfaces but the streamwise vorticity contours have a large magnitude where this vortex is located.

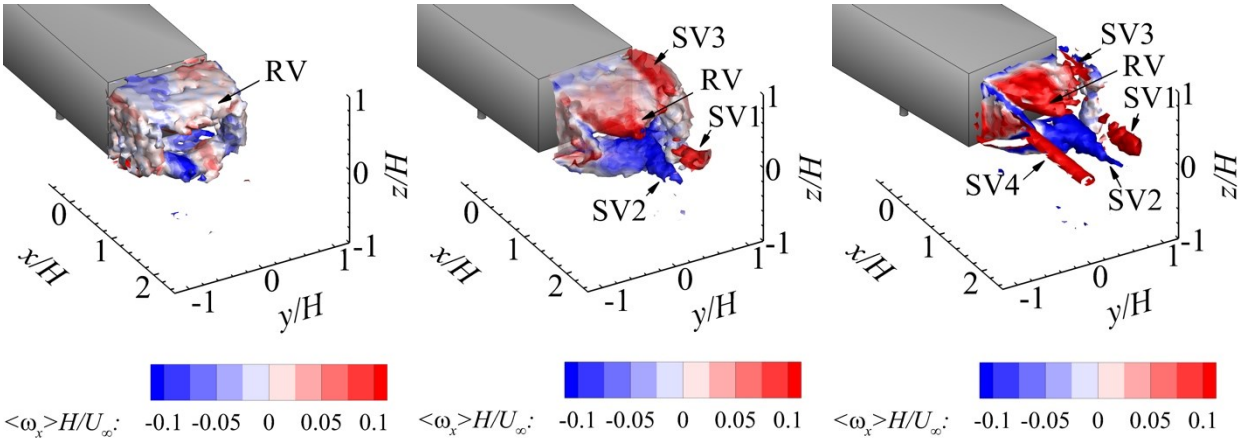

Figure 28: Isosurfaces of Q-criterion within the wake where respective isosurface values and yaw angles are (a) Q = 0.5 for β = 0°, (b) Q = 0.3 for β = 5°, and (c) Q = 0.75 for β = 10°. The isosurfaces have contours of streamwise vorticity overlayed.

4.5 Spectral Flow Properties

To understand the spectral characteristics of the wake dynamics during crossflow and how these may differ from the zero-yaw case, the frequency-multiplied power spectral densities (PSD) of the u-velocity component are evaluated. The theory underlying this PSD analysis was summarized in Section 2.9.3. PSD was calculated using the time-resolved velocity fields measured at 2.5 kHz and the frequency resolution of the PSD analysis is St_H = 0.0072. The PSD is locally averaged on a 3 × 3 × 3 grid of neighboring data points centered at (x, z) = (1.30H, 0.25H). The y location for β = 0, 5, 10° cases is set to 0.45, 0.75, and 0.90H, respectively. The resulted frequency-multiplied PSD (St_H×PSD) are shown in Figure 29.

The zero-yaw case is analyzed first and compared to previous investigations by Grandemange et al. (2013b) and Volpe et al. (2015). Figure 29(a) shows the frequency-multiplied PSD spectrum from probing at $(x, y, z) = (1.30H, 0.45H, 0.25H)$. Three peaks are identified at $St_H = 0.09$, 0.12, and 0.18. Based on the findings of previous studies, the higher frequency peak at $St_H = 0.18$ is attributed to wall-normal vortex shedding of the shear layer while the middle peak at $St_H = 0.12$ is attributed to spanwise vortex shedding of the wake (Grandemange et al. 2013b; Volpe et al. 2015). The third peak at $St_H = 0.09$ closely matches the bubble pumping frequency previously identified by Khalighi et al. (2001; 2012) and Volpe et al. (2015). Out of the three peaks, the wall-normal shedding peak has the highest power, followed by an even peak power for the two lower frequency peaks.

Figure 29(b) shows the PSD spectrum for the $\beta = 5°$ case at $(x, y, z) = (1.30H, 0.75H, 0.25H)$; a point in the windward shear layer. Two peaks are identified at $St_H = 0.14$ and 0.19 which are both close to the two higher frequency peaks identified in the zero-yaw case. The low-frequency bubble-pumping that was observed for the zero-yaw case disappears. The lower frequency peak at $St_H = 0.14$ is attributed again to spanwise shedding and the higher frequency peak at $St_H = 0.19$ is attributed to wall-normal shedding. In general, the power content within the full spectrum shows a significant increase over the zero-yaw case. The higher frequency peak has the highest power content out of the two peaks for this case. Compared to the zero-yaw case, however, the relative magnitude of the spanwise shedding peak is greater, which indicates a stronger vortex shedding on the windward side of the $\beta = 5°$ case.

The spectrum for the last case of $\beta = 10°$ is shown in Figure 29(c) where the probe point is again positioned in the windward shear layer at $(x, y, z) = (1.30H, 0.90H, 0.25H)$. Two peaks are identified at $St_H = 0.14$ and 0.17. The lower frequency peak remains the same as the $\beta = 5°$ case, but the high frequency peak reduces slightly to $St_H = 0.17$. There are no fundamental changes in the mean flow characteristics summarized in Section 4.2, so the lower frequency peak is again attributed to spanwise shedding and higher frequency peak to wall-normal shedding. The magnitude of the lower frequency peak is this time larger than that of the high frequency peak, indicating that the spanwise shedding is stronger that the wall-normal shedding. In addition, the power within the total spectrum is significantly higher than the previous two cases, having both more energy contained within the spectrum as well as a peak power that is almost three times greater than the previous maximum.

The spectra in Figure 29 make it possible to identify three different patterns within the wake oscillations as the yaw angle increases. When comparing the dominant frequencies identified for each case, two primary peaks are always present and the respective frequencies match closely for each peak (St_H = 0.12-0.14 and St_H = 0.17-0.19). This pattern suggests that an increase in yaw angle had negligible effect on the shedding frequencies within the range of $0 \leq \beta \leq 10°$. The only variation between the spectra is therefore related to the power content of the peaks at these characteristic frequencies. The second trend can then be seen when comparing the total power content for each case. Increasing the yaw angle, significantly increases the power contained within the spectrum, with the largest increase being between the two yawed cases. This is consistent with the larger $\langle u^2 \rangle$ isosurface observed in Figure 25 on the windward sides of the wake for $\beta = 5°$ and 10°. The last trend is identified by comparing the power of the two shedding mode peaks for each case. As the yaw angle increases, so does the comparative power of the spanwise shedding peak with respect to the higher wall-normal frequency peak, eventually surpassing it in power content for the $\beta = 10°$ case.

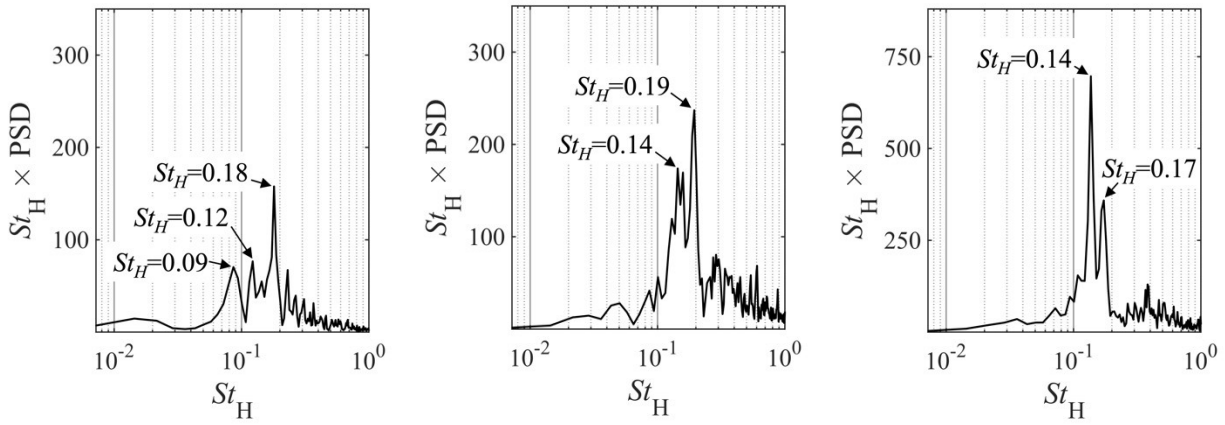

Figure 29: Frequency-multiplied PSD of streamwise velocity for yaw angles of $\beta = 0°$ (a), $\beta = 5°$ (b), $\beta = 10°$ (c). The PSD spectrum for the $\beta = 0°$ case is based on fluctuations at the coordinates of $(x, y, z) = (1.30H, 0.45H, 0.25H)$. The PSD spectrum for the $\beta = 5°$ case is based on fluctuations at the coordinates of $(x, y, z) = (1.30H, 0.75H, 0.25H)$. Lastly, the PSD spectrum for the $\beta = 10°$ case is based on fluctuations at the coordinates of $(x, y, z) = (1.30H, 0.90H, 0.25H)$.

4.6 Coherent Motions within the Wake Based on POD

Proper orthogonal decomposition (POD) is applied here based on the method of snapshots POD (Sirovich 1987) to identify the energetic motions. A more detailed account of the theory for POD can be found in Section 2.9.4. The analysis focuses on the entirety of the 3D wake motions since the POD algorithm is applied to the full velocity field, accounting for all three velocity components within a 3D measurement domain. The data used for this analysis was the cyclic data with a temporal resolution of 40 Hz because it was collected over a large time span, improving the convergence of turbulent statistics.

4.6.1 Spatial Mode Energy

The energy of the first 20 spatial modes as a percentage of the total turbulent kinetic energy is presented in Figure 30. From Figure 30(a), the energy distribution for the zero-yaw case shows that the first mode contains 33% of the total energy while the first four modes for the zero-yaw case contain 44% of the total energy. In contrast to this, for the $\beta = 5°$ case, mode one contributes to 9% of the total kinetic energy, and the first four modes contain 23.6% of the total energy. The yaw case of $\beta = 10°$ has an energy content distribution similar to the $\beta = 5°$ case with a gradual reduction of energy. For $\beta = 10°$, the first mode contribution is 11%, and the first four modes contain 28% of the total energy. The high energy content of the first mode for the zero-yaw case is the most apparent difference between the three cases. The high energy level of this first mode has been previously observed by multiple studies (Östh et al. 2014; Perry et al. 2016; Pavia et al. 2018; 2020; Fan et al. 2020), however, the energy content observed within this analysis is much higher still, underscoring the significance of 3D data included in the decomposition.

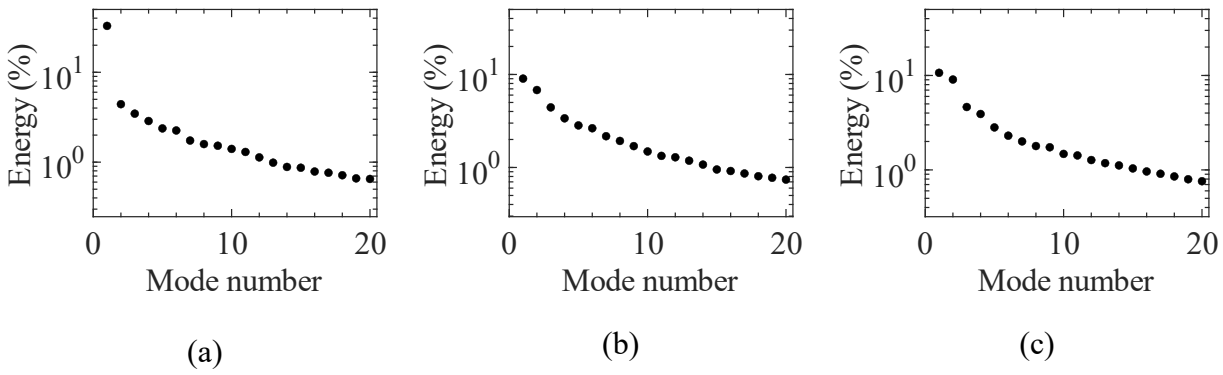

Figure 30: The distribution of POD mode energy for yaw angles (a) $\beta = 0°$, (b) $\beta = 5°$, and (c) $\beta = 10°$.

4.6.2 Zero-Yaw Spatial Modes

The spatial distribution of the first four modes for the zero-yaw case are presented in Figure 31. Mode one consists of two symmetric structures situated on spanwise sides. This observed pattern agrees with the first POD mode identified by Pavia et al. (2018), which they named the lateral symmetry-breaking mode. Recent studies by both Pavia et al. (2020) and Fan et al. (2020) also observed this spatial pattern within 3D spatial modes and 2D spatial modes, respectively. Pavia et al. (2018) suggested that this lateral spatial distribution is attributable to both the bi-stability phenomenon and spanwise oscillations of the wake. This conclusion is further supported by the disproportionately high energy content of the first mode in Figure 30(a) since both of these features are characterized by dominant fluctuations within the wake. The second mode consists of three lobes, one at the mid-span on the $z/H = 0.35$ plane, and the two other lobes on the $z/H = -0.2$ plane. In the study of Grandemange et al. (2013b), hot wire measurements across several planes normal to the streamwise axis were used to identify the distribution of the spectral peaks for the zero-yaw case. It was found that the wall-normal oscillation frequency peaks had a distribution that very closely aligns with the orientation of the structures in mode two, with the distributions localized around the bottom corners of the body and at the top of the body along the midspan. Given that the upper and lower lobes of this mode are out of phase and amplitude switching occurs with respect to the $z/H = 0$ plane, this mode can be attributed to wall-normal wake dynamics. Again this spatial distribution is consistent with low order POD modes found by Pavia et al. (2018; 2020)

and Fan et al. (2020) and was originally referred to as the vertical symmetry breaking mode by Pavia et al. (2018). Mode three consists of four lobes that form a plus pattern downstream of the rear face. The amplitude switching within this mode changes its expression between the horizontally and vertically distributed structures. The study by Pavia et al. (2018) found a POD mode with a similar 2D distribution which they attributed to planar symmetry preservation within the wake. They found that the symmetry of the low order representation increased when this mode was included. This theory was later reaffirmed in the POD analysis of Pavia et al. (2020). The fourth mode consists of several smaller structures with little symmetry across any plane signifying that it is related to small-scale structures. The energy of this mode is approximately 3%.

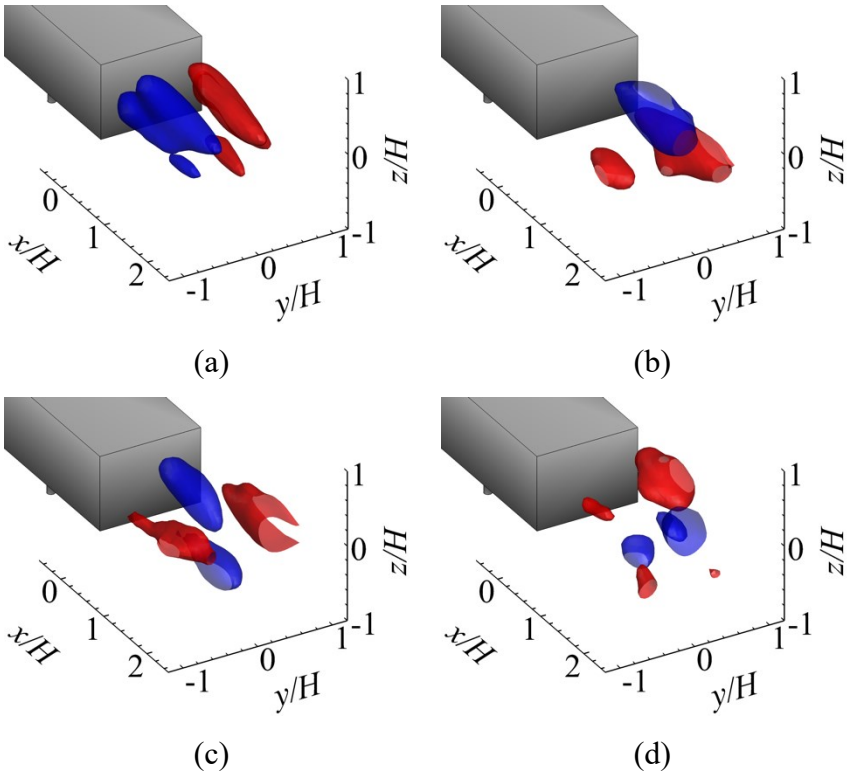

Figure 31: The spatial distribution of (a) mode 1, (b) mode 2, (c) mode 3, and (d) mode 4 of POD of the 3D velocity field at yaw angle of $\beta = 0°$. All isosurfaces are visualized of the same spatial magnitude.

4.6.3 Yawed Spatial Modes

Figure 32 shows the spatial organization of the first two modes for $\beta = 5°$ (a-b) and $\beta = 10°$ (c-d). Only the first two spatial modes are presented for each case as the higher order modes contain less energy. Further justification for only showing the first two spatial modes will be given in the PSD analysis of mode coefficients at the end of this section. The spatial structures of mode one and two for both yaw cases are very similar and therefore will be described with reference to both yaw cases. Mode one consists of a large structure favoring the upper half of the wake and two smaller structures with the opposite amplitude, position inward and below the primary structure. All three structures are in the windward side of the wake. Mode two consists of two structures situated along the windward side of the wake. The larger structure has a downward tilt as it moves downstream. The second structure is located above the larger primary structure. The spatial organization of these two structures with opposite amplitudes also indicates a wall-normal dynamic in the windward shear layer. The similarity between the mode structures for both yaw cases imply that there are no fundamental changes in the large-scale flow structure for the yawed flow fields. In general, both modes for $\beta = 5°$ and $\beta = 10°$ show wall-normal alternations within the windward shear layers. The high order POD modes do not show any evidence of a symmetry–breaking mode, or spanwise oscillations originating from the interaction of leeward and windward shear layers.

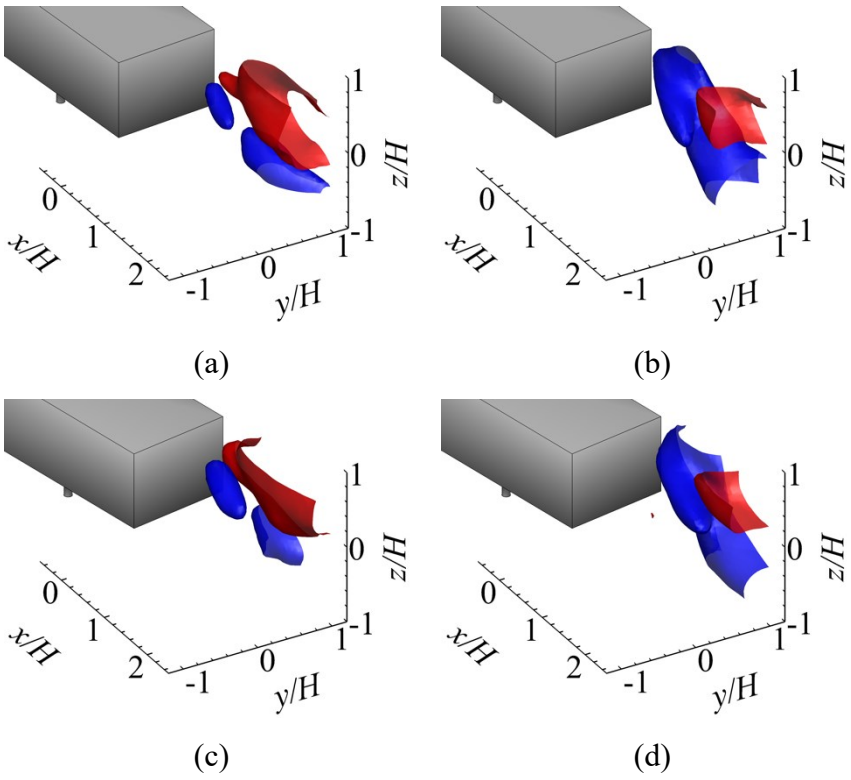

Figure 32: The spatial distribution of (a) mode 1 and (b) mode 2 for the $\beta = 5°$ case, and (c) mode 1 and (d) mode 2 for the $\beta = 10°$ case resulting from POD of the 3D velocity fields. All isosurfaces are visualized with the same spatial magnitude.

4.6.4 PSD Analysis of Temporal Coefficients

Figure 33 shows the frequency-multiplied PSD of the time-dependent mode amplitudes. Mode one of the zero-yaw case in Figure 33(a) has a high energy content within frequencies below $St_H = 0.1$. This low frequency energy distribution is consistent with the spanwise bi-stable switching that occur at timescales much larger than that of the shedding process. The energy distribution is also relatively broad which agrees with the non-periodic nature of the bi-stability phenomenon (Grandemange et al. 2013b). Mode one also contains a peak at $St_H = 0.13$ which coincides with the spanwise shedding frequency that was discussed in Section 4.5. Mode two has a high frequency peak at $St_H = 0.19$ which matches the wall-normal shedding frequency discussed

in Section 4.5, again supporting the discussion of the second spatial mode in Figure 31(b). The high frequency peak at $St_H = 0.19$ is identified in modes 3 and 4 as well.

In Figure 33(b), modes one and two for the $\beta = 5°$ case both have large peaks at $St_H = 0.19$. The first two modes of $\beta = 10°$ case in Figure 33(c), have high amplitude peaks at a smaller St_H of 0.13. The mode energy at St_H smaller than 0.1 is negligible for both $\beta = 5°$ and 10°, further indicating the lack of bi-stable switching. A significant increase in power is also seen when comparing the first two modes of the yawed spectra to that of the zero-yaw spectra. This is consistent with the trend identified in the PSD plots of Section 4.5. Modes three and four for the yawed flow cases contain no distinguishable peaks and have very low energy content throughout the spectra when compared to the first two modes.

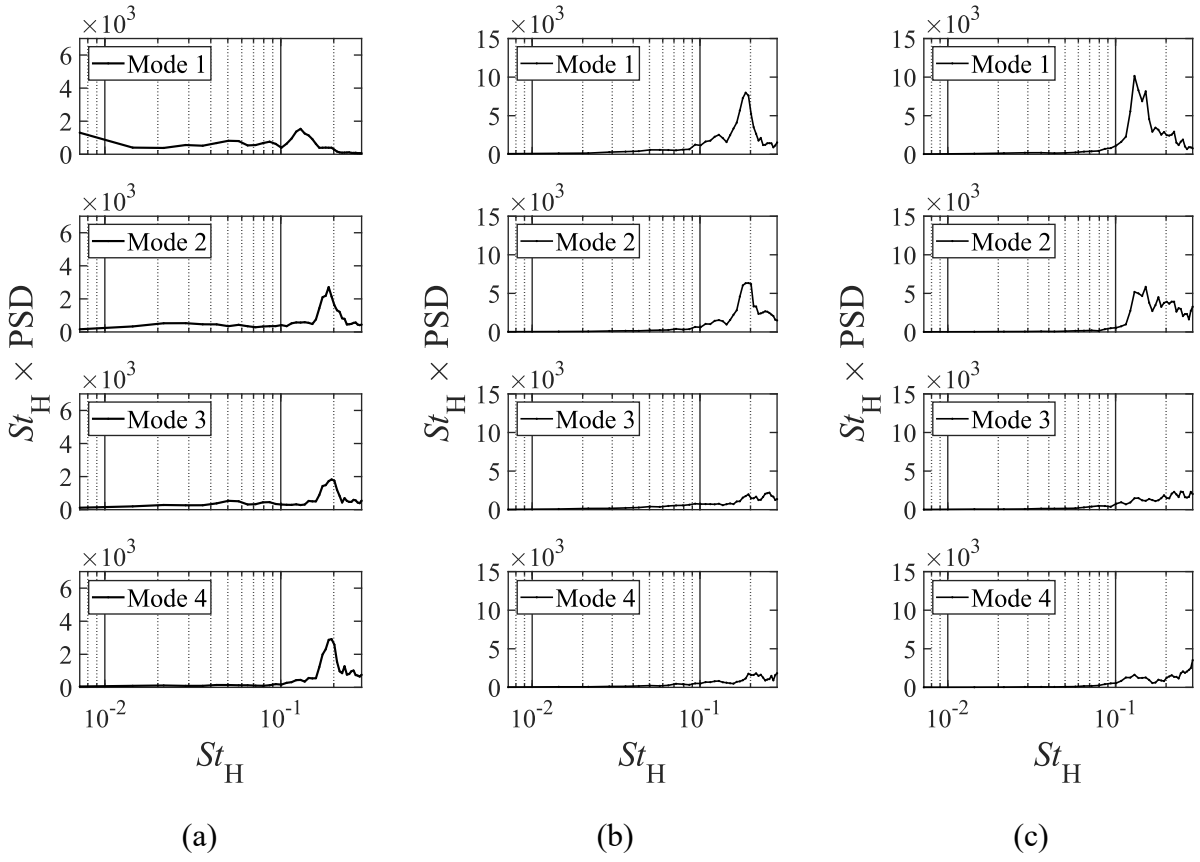

Figure 33: Frequency-multiplied PSD of the POD mode coefficients for the first four spatial modes of yaw cases (a) $\beta = 0°$, (b) $\beta = 5°$, and (c) $\beta = 10°$.

4.7 Conclusions

Measuring and characterizing the full wake flow field is a fundamental step in understanding the aerodynamic properties of a vehicle and sets the basis for any further aerodynamic development. Within this chapter, the 3D flow structures in the near-wake of a square-back Ahmed body at two yaw angles of $\beta = 5°$ and 10° were characterized and compared with the flow structures at $\beta = 0$, in order to better understand its fundamental flow properties at yaw. The experiments were carried out using a half-scale Ahmed body in a wind tunnel at Reynolds number of 9.2×10^4. State-of-the-art measurements of the wake flow were obtained using a large-scale time-resolved 3D-PTV that employed helium-filled soap bubbles.

First the mean flow fields for each yaw case were analyzed, focusing on the velocity distributions and resulting flow patterns. The baseline consisted of a large separation bubble and corresponding recirculating flow. Spanwise flow was nearly symmetric and a slightly asymmetry was observed between the flow over top and underneath the body. Comparing these features to crossflow, it greatly increased the asymmetry in the mean flow. The separation bubble became smaller and inclined to the windward side. Recirculating vortices were identified in both planes of symmetry for the zero-yaw wake. As the yaw angle increased, the recirculating vortex on leeward side became dominant and the windward vortex decreased in strength. Furthermore, with increasing yaw angle, the downwash motion from the top-edge and the spanwise motion from the leeward edge of rear-face strengthened. A spanwise asymmetry was notable in all three components of flow. The results also showed that streamwise and streamwise-spanwise Reynolds stresses became stronger and covered a larger region along the windward side as the yaw angle increased. In contrast, streamwise and streamwise-spanwise Reynolds stresses became weaker along the leeward side.

The mean flow analysis was supplemented with the identification of vortex structures present in the mean flow. First vortex filaments were visualized showing a continuous vortex ring in the baseline wake, progressing to an increasingly skewed vortex ring as the crossflow angle increased. The leeward portion of the vortex ring was positioned closer to the back face of the Ahmed body for the yawed cases. Four streamwise vortex filaments also appeared in the yawed wakes as crossflow increased. Two of them originated closer to the top corners of the body, and the

remaining two formed downstream of the vortex ring, closer to the windward side. A second analysis based on Q-criterion isosurfaces and streamwise vorticity contours verified the existence of each vortex filament.

Spectral analysis of the wake motions in the upper-portion of the windward shear layer found three trends as yaw angle increased. The first was that the Strouhal number of the spectral peaks associated with the spanwise and wall-normal oscillations of the shear layer did not change. The second pattern was an increase in the peak magnitudes which indicated that the energy of the flow oscillations increased with the yaw angle. The last trend showed an increase of the spanwise shedding power relative to the wall-normal shedding power as yaw angle increased.

Finally, proper orthogonal decomposition of the velocity field showed that the first mode of the zero-yaw case was attributed to the bi-stability phenomenon and spanwise oscillations within the wake and the second mode was attributed to wall-normal oscillations. When the yaw angle was increased to 5° or 10°, a more than 20% decrease in the energy of the first spatial mode relative to subsequent modes was observed, caused by the disappearance of the bi-stability. The first two spatial modes for the yawed cases matched closely with respect to the yaw angle and showed that the majority of turbulent kinetic energetic within the yawed wakes were on the windward side of the wake.

Chapter 5: Aerodynamic Forces and Moments

The drag of commercial road vehicles is a principal contributing factor to their fuel efficiency. The other aerodynamic loads can have detrimental effects on the stability of a vehicle. Furthermore, multiple studies have found that the ideal condition of zero-yaw onset flow is not representative of real-world driving conditions (SAE International 2012; Garcia de la Cruz et al. 2017; Dalessio et al. 2017), which means aerodynamic loading during crossflow bears much more importance.

The preceding investigation and characterization of the square back Ahmed body wake at yaw has also shown that significant changes in the wake structure are observed at yawed flow angles. Drag reduction strategies that have proven to be effective for the zero-yaw wake, therefore may not be relevant to drag reduction at yaw as the drag generating mechanisms themselves may no longer be present at yaw. For all of these reasons, several passive drag reduction devices were tested. The aerodynamic loads for each case were measured at yaw angles ranging from $-12.5° \leq \beta \leq 12.5°$. The experimental method is described in Experiment II in Section 3.3.

5.1 System Load Corrections

As mentioned in Section 3.3.3, a portion of the measured load comes from the experimental support structure. Measurements were conducted to quantify these additional loads so that they could be subtracted from the full geometry measurements. Theses loads were incorporated into the load corrections described in Section 3.3.3. Figure 34 shows the coefficients of the force and moment corrections applied to the results presented in this chapter. The lift coefficients are not presented in Figure 34; justification will be given in Section 5.2. The coefficients beginning with C_B denote the body-indexed forces and the coefficients beginning with C_{MB} denote the body-indexed moments.

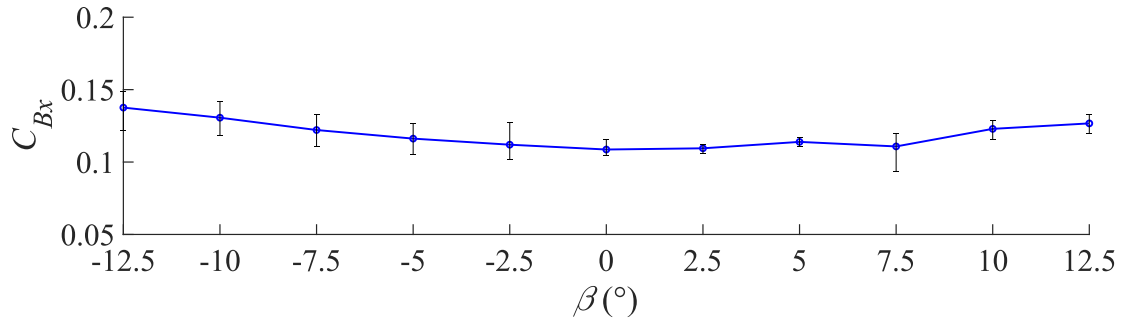
0.2
0.15
0.1
0.05
C_{Bx}
-12.5 -10 -7.5 -5 -2.5 0 2.5 5 7.5 10 12.5
β (°)

(a)

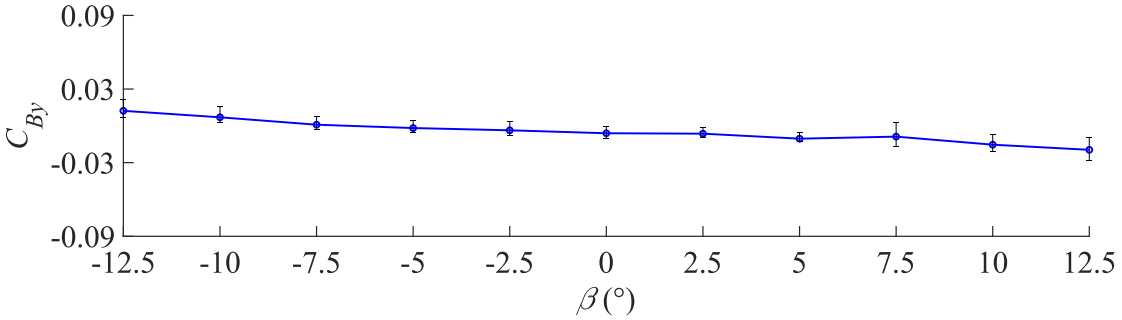
0.09
0.03
-0.03
-0.09
C_{By}
-12.5 -10 -7.5 -5 -2.5 0 2.5 5 7.5 10 12.5
β (°)

(b)

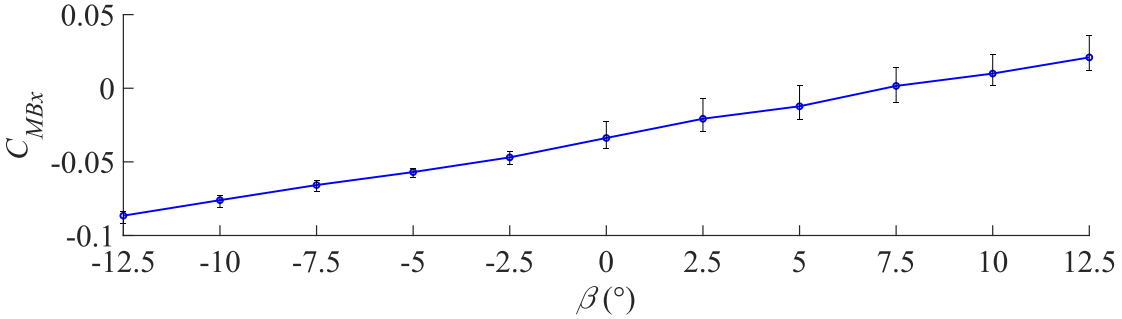
0.05
0
-0.05
-0.1
C_{MBx}
-12.5 -10 -7.5 -5 -2.5 0 2.5 5 7.5 10 12.5
β (°)

(c)

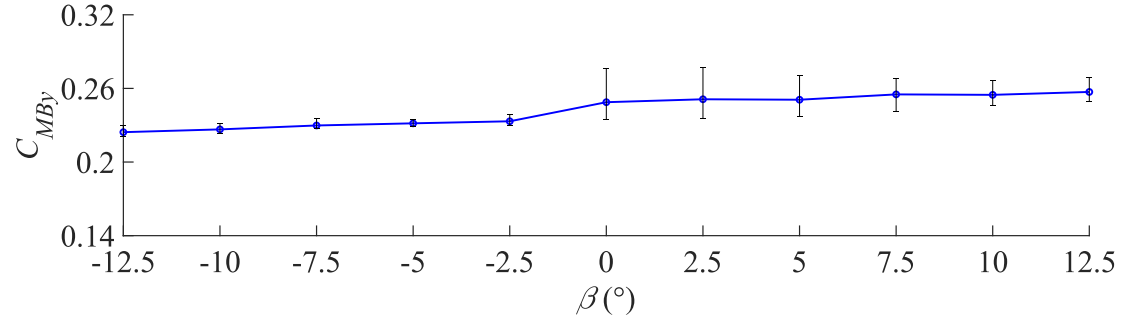
0.32
0.26
0.2
0.14
C_{MBy}
-12.5 -10 -7.5 -5 -2.5 0 2.5 5 7.5 10 12.5
β (°)

(d)

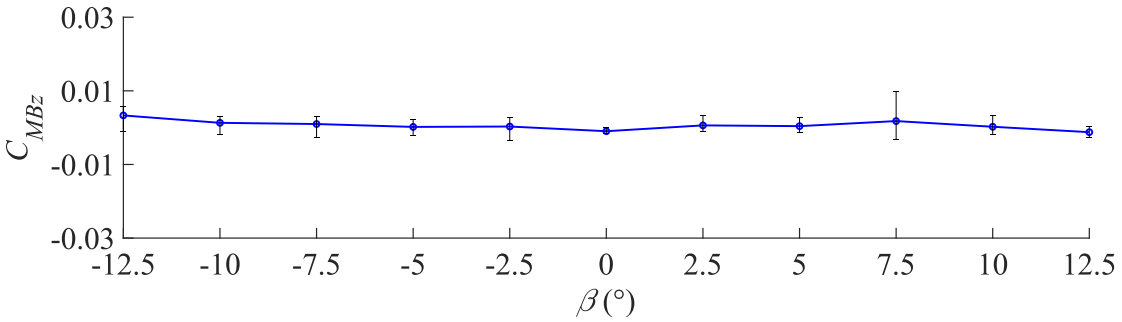

(e)

Figure 34: The coefficients of (a) drag, (b) side force, (c) roll, (d) pitch, and (e) yaw caused by the support structure across the yaw angle range of -12.5° ≤ β ≤ 12.5°. The corrections are subtracted from all drag measurements to account for measured loads not that are not directly related to the aerodynamic loads of the Ahmed body. Error bars represent the highest and lowest measurements taken across the three runs.

5.2 Aerodynamic Drag and Side Forces

The forces measured for the drag reduction cases are presented in terms of coefficients normalized by the frontal area and the freestream flow speed as was described in Section 3.3.3. Figure 35 shows both the body-indexed (C_{Bx}) and wind-indexed (C_{Wx}) drag coefficients for each drag reduction case across the yaw angle range of -12.5° ≤ β ≤ 12.5°. The body-indexed coefficients are always aligned with the body's coordinate system while the wind-indexed coefficients are always aligned with the freestream flow direction. The zero-yaw drag coefficient for the baseline was C_{Bx} = 0.37 which is on the upper end of the range of values found in previous studies. The pitot tubes used for verifying the wind tunnel freestream speed showed some drift during the temperature change discussed in Section 3.3.1, so experimental freestream speeds may not have been exact. Accounting for this variation in the assumed freestream speed when calculating drag coefficients, can quickly account for the deviation from previous experiments. A shift of 1 m/s in the assumed freestream velocity for the zero-yaw baseline case results in a drag coefficient shift of ~0.03.

All drag reduction devices prove to be effective to varying extents with the baseline configuration having the largest drag coefficients across the yaw range. The reported values for

each case are the averages of three data sets. From Figure 35(a), the resulting body-indexed drag reductions for all cases, ranked from highest to lowest, are the boat tail with a 26.8% reduction, followed then by the cylinder rake (11.1% reduction), the dual fan configuration (7.2% reduction), and finally the vertical splitter with a 6.9% reduction. The measured boat tail reductions are larger than previous studies of the boat tail geometry (Khalighi et al. 2012; Schmidt et al. 2018; Bonnavion et al. 2019; Lorite-Díez et al. 2020). The relationship between yaw and the body-indexed drag is initially parabolic before hitting an inflection point and slightly plateauing when $5° \leq |\beta| \leq 12.5$. The baseline configuration is a slight exception, having a more linear initial trend. Similar trends have been measured in the studies of Gohlke et al. (2007) and Lorite-Díez et al. (2020). The drag reductions are also fairly constant when the yaw angle is $|\beta| \geq 2.5°$ for all cases, but only in terms of overall magnitude of the reduction. Since the coefficients are lower at low angles of yaw, the percent drag reduction is greater at low angles of yaw for all cases. The averaged percent drag reductions over the entire yaw range are provided in Table 3 for each case.

Measuring drag forces at equal but opposite yaw angles also gives a measure of the experimental validity. Since the setup and yaw angles were symmetric about $\beta = 0°$, the resulting drag coefficient curves should be symmetric. This is observed for the majority of the body and wind-indexed cases, confirming that there were no fundamental faults with the experimental setup. The dual fan configuration is the only outlier, which could be due to the direction of rotation of the fans which was counter clockwise for both fans. The fan speed and CFM were not measured during the experiment as this case was only meant to give an initial indication into the effectiveness of the configuration and not a detailed study of fan performance.

The wind-indexed drag reductions were also investigated and can be seen in Figure 35(b). The resulting wind-indexed drag reductions from the passive devices rank in the same order as the body-indexed reductions. From highest to lowest, the average drag reduction for each device is the boat tail with a 24.9% reduction, followed by the cylinder rake (10.1% reduction), the dual fan configuration (6.5% reduction), and finally the vertical splitter with a 5.8% reduction. The reductions are all slightly less than the respective body-indexed reductions. The baseline wind-indexed drag coefficient curve shows an approximately linear drag increase with yaw angle. All the other configurations show initially parabolic coefficient curves, becoming linear at yaw angles of $|\beta| \geq 5°$. The parabolic curvature at low yaw angles signifies a lower sensitivity to yaw for the drag reduction devices which is a desirable result. Respective device drag reductions are again all

fairly consistent when $|\beta| \geq 2.5°$. The slope of the linear portions of the curves is similar for all cases at $\partial C_{Wx}/\partial\beta \sim 0.02$. The similarities noted between the body-indexed and wind-indexed coefficients are expected since they are planar rotational transformations of each other. Variations between the two cases are expected to be accounted for by the respective side-force coefficients which will be investigated next. The averaged percent drag reductions for each case over the entire yaw range are also provided in Table 3.

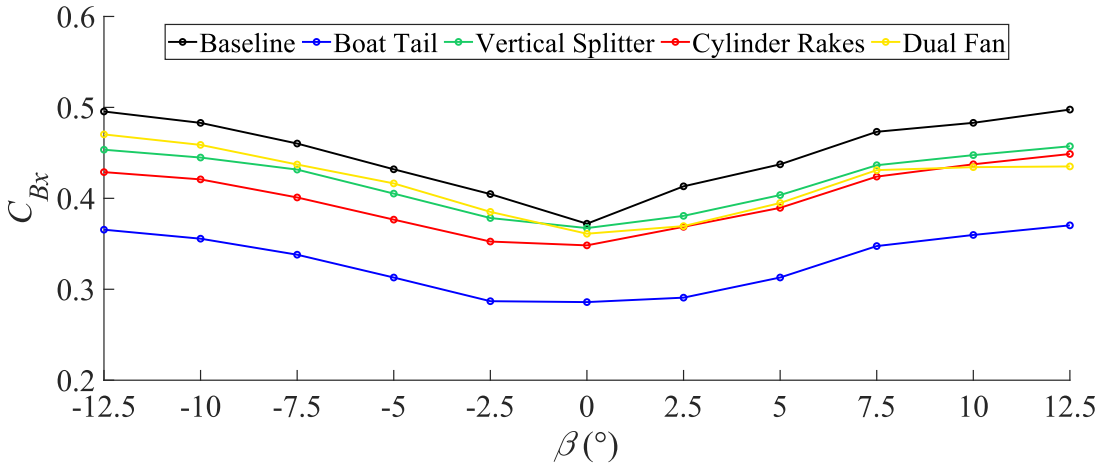

(a)

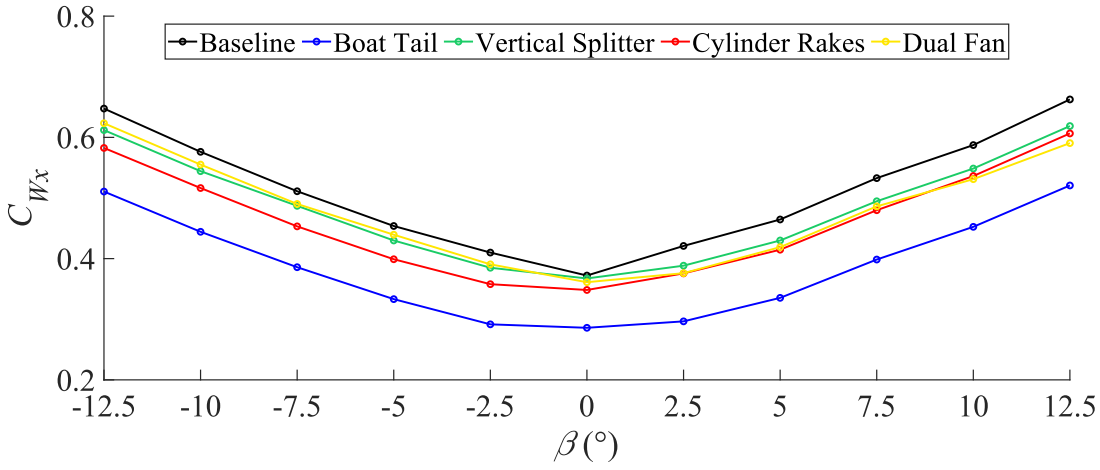

(b)

Figure 35: The streamwise force coefficients as a function of yaw angle for the (black) baseline, (blue) boat tail, (green) vertical splitter, (red) cylinder rake, and (yellow) dual fan configurations.

Table 3: The averaged percentage reduction in drag coefficient relative to the baseline for both body-indexed and wind-indexed reference frames.

	Boat Tail	Vertical Splitter	Cylinder Rakes	Dual Fan
% C_{Bx} Diff	26.8%	6.9%	11.2%	7.1%
% C_{Wx} Diff	24.9%	5.8%	10.1%	6.6%

The coefficients of side force for all drag reduction configurations can be seen in Figure 36. Both the body-indexed coefficients (C_{By}) in Figure 36(a) and the wind-indexed coefficients (C_{Wy}) in Figure 36(b) are anti-symmetric and approximately linear throughout the yaw range. The slope for the body-indexed coefficients is $\partial C_{By}/\partial\beta \sim 0.06$ and for the wind-indexed coefficients it's $\partial C_{Wy}/\partial\beta \sim 0.05$ which is over a factor of two greater than the corresponding drag force slope for the wind-indexed cases. The steeper slope of the body-indexed coefficients is expected as they account for the lower drag coefficients. Relative body-indexed side force deviations between the configurations are smaller than the drag forces deviations with the largest differences over the baseline case being a 12.3% reduction for the boat tail case and a 3.7% increase for the vertical splitter. All of the reductions for the side force, averaged over the entire yaw range, can be seen in Table 4.

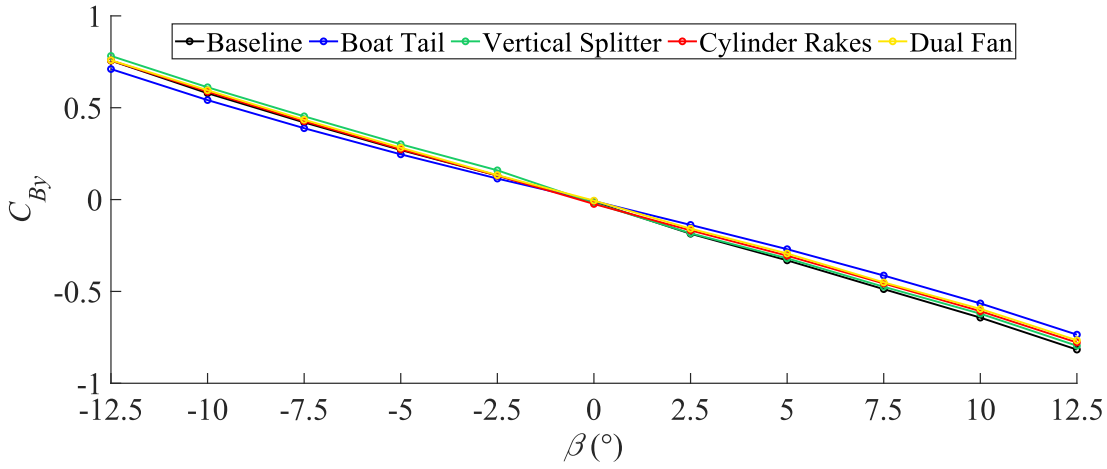

(a)

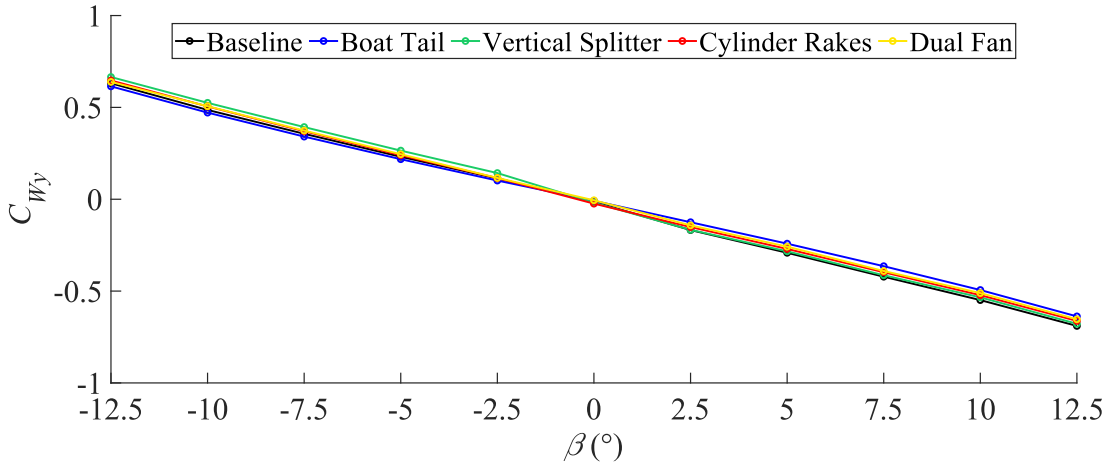

(b)

Figure 36: The spanwise force coefficients as a function of yaw angle for the (black) baseline, (blue) boat tail, (green) vertical splitter, (red) cylinder rake, and (yellow) dual fan configurations.

Table 4: The averaged percentage reduction in side force coefficient relative to the baseline for both body-indexed and wind-indexed reference frames at yaw ($|\beta| \geq 2.5°$).

	Boat Tail	Vertical Splitter	Cylinder Rakes	Dual Fan
% C_{By} Diff	12.3%	-3.7%	3.0%	3.4%
% C_{Wy} Diff	9.9%	-5.5%	1.6%	2.7%

The load cell used had a disproportionate amount of thermal drift for the F_z force component (F_{Bz} and F_{Wz} are the same). For these flow cases where the body is nearly symmetric across the $y/H = 0$ plane aside from the ground plane plate and the support posts, the effective F_z forces were

small and the measure forces were significantly impacted by the thermal drift. For these reasons the F_z force components will not be reported on.

Overall, the side force coefficients are more than twice as sensitive to yaw than the drag coefficients. The body-indexed force coefficients also show some non-linearity in the trends which is not shared with the wind-indexed coefficients, most notable in the respective drag coefficients. One hypothesis was that the non-linear trends were proportional to the change in projected frontal area for the body-indexed forces. For the body-indexed drag coefficients, the projected area of the front face normal to the freestream scales with $W \times \cos(\beta)$, which matches the parabolic trend over the small yaw range being considered. Similarly, the side force coefficients would be tied to the projected side area which scales by $L \times \sin(\beta)$, a linear trend over the small yaw range. These variations, however, were not found to fully linearize the body-indexed drag coefficient trends.

The reference frames and their effects on the coefficient curves are also useful when the results are related to the expected change in forces during a crossflow speed increase, in the context of real-world driving conditions. For the body-indexed case, the increased velocity of the crosswind relative to the vehicles motion could be expressed as a constant crosswind speed but an increased relative yaw angle. This would mean the effects of the speed increase on the aerodynamic forces could be estimated by shifting along the coefficient curves to the appropriate effective yaw angle. The wind-indexed coefficients intern would remain constant regardless of crossflow velocity and would be much better indicators of crossflow speed increase effects. The expected forces can be calculated directly without having to determine an effective yaw angle, a much more efficient process.

Comparing the force characteristics of the different devices, the boat tail was the most effective device by a large margin. It gave a significant reduction in drag force and side force coefficients while also show less sensitivity to yaw angle for the side force coefficients which could have a large impact on vehicle stability.

Finally, the observed drag coefficient increases with yaw also imply that there is an additional drag term with yaw. An induced drag term has been suggested by Mercker (1986), relating the induced drag to the sum of the squared side force and lift components. Equation 28 shows the proposed relation for the induced drag term C_{Bxi}:

$$C_{Bxi} \propto \left({C_y}^2 + {C_z}^2\right). \qquad 28$$

Since the lift force measurements for the current experiments were relatively small and subject to drift, the following comparisons of induced drag will use solely the square of the side force component as the Mercker (1986) equivalent. This suggested induced drag term is compared to the measured induced drag term for each case, as described by Equation 29:

$$C_{Bxi} = C_{Bx} - C_{Bx(\beta=0°)} \qquad 29$$

and can be seen in in Figure 37(a). First and second order regressions were performed, and the resulting curves are superimposed over the data points. The proportional increase between the drag increase and induced drag is not clearly observed. This could potentially be explained by the geometry; the original relationship was found for automotive models with forebody slopes and backlight angles which are not features of the square-back Ahmed body. Howell (2015) determined that for this induced drag relationship, in the context of more streamlined automotive shapes, the induced drag term was primarily related to the lift forces which were much larger than the side forces. The measured lift forces from these experiments showed the opposite and were small compared to the side forces implying the induced drag is linked to the side force, but not necessarily to its square. The first order regression has an R^2 value of 0.722 while the second order regression has an R^2 value of 0.844. Given that the side force was squared, and the second order regression gives a much better fit to the data than the first order, the induced drag may be linearly proportional to the measured side force.

A more accurate relationship for the induced drag term for square-backed bodies may therefore be based solely on the side force. The measured wind-indexed drag coefficients from this study were also noted to have linear increases, further suggesting that the body-indexed drag and side force increases may be linearly proportional. This theory is tested with the body-indexed side force coefficients being compared to the respective induced drag coefficients in Figure 37(b). First and second order regressions were again performed and are superimposed. Both curves predict the distributions of the data points well. The coefficient of determination values for the first and second order fits are this time R^2 = 0.840 and 0.860, respectively. The first order regression fit results in a curve that describes the induced drag relationship with a similar accuracy as the second order fits in both Figure 37(a) and (b). Based on these results, it can be argued that the induced drag term is proportional to the side force for square backed bluff bodies.

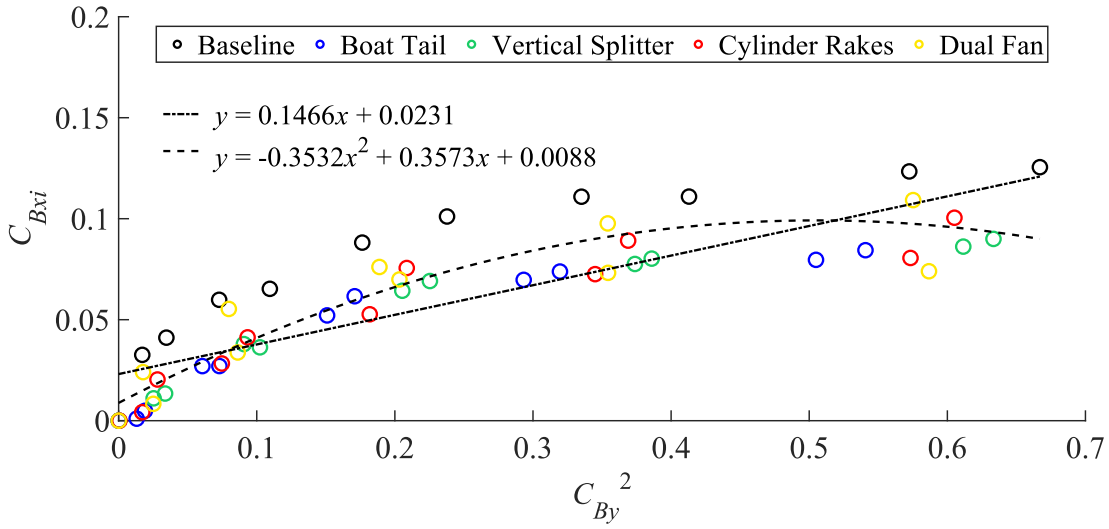

(a)

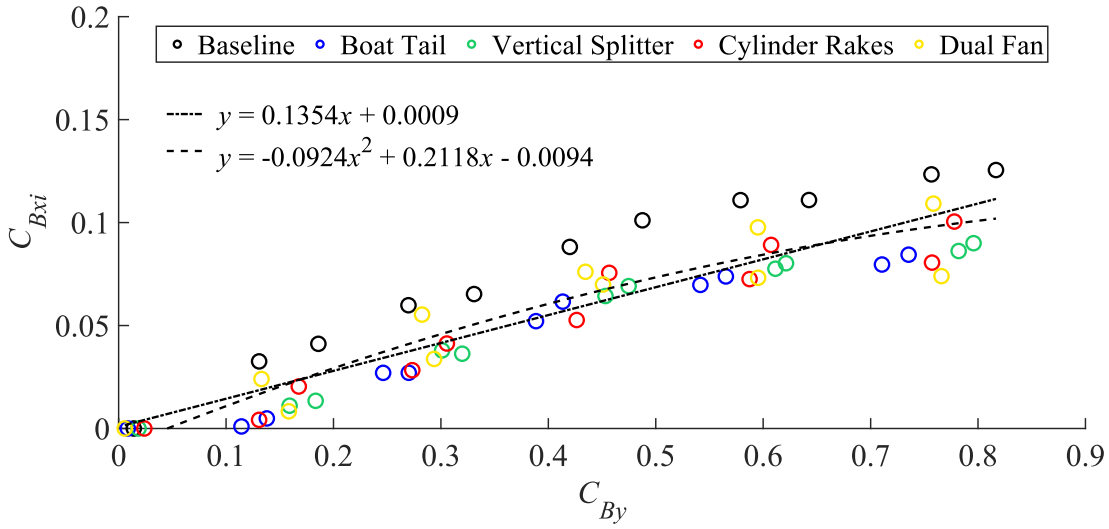

(b)

Figure 37: The body-indexed induced drag at yaw for all configurations as a function of (a) the square of the body-indexed side force and (b) the body-indexed side force. First order and second order regressions were performed on the data points and the corresponding lines of best fit are overlayed along with the resulting polynomial equations.

5.3 Aerodynamic Moments

The aerodynamic moments were also measured for the drag reduction devices. All moments were corrected so that they were centered at the reference frame origins in Figure 20. The roll moment coefficients (C_{MBx}, C_{MWx}) can be seen in Figure 38 where an approximately linear relationship is seen between the roll moment and the body yaw angle for both the reference frames. Anti-symmetry of the roll coefficients is also maintained across the zero-yaw baseline, a property that is expected for a symmetric body. Out of the configurations, the boat tail is the clear outlier with an average roll moment reduction of 12.2% over the body-indexed baseline, closely following the measured side force reduction. The boat tail roll moment slope is also not as constant, showing a lower sensitivity to yaw within the range of $-7.5° \leq \beta \leq 7.5°$. The only significant difference between reference frames was the slope of the roll moments. The slope of the body-indexed roll curve is $\partial C_{MBx}/\partial\beta \sim 0.10$ while the wind indexed is $\partial C_{MWx}/\partial\beta \sim 0.08$. The roll moment is therefore over 50% more sensitive to the yaw than the corresponding side force for both reference frames ($\partial C_{Mx}/\partial C_y \sim 1.7$). The averaged reductions in roll moment for each case can be found Table 5. The vertical splitter resulted in a slight increase in roll moment, and the remaining two cases had little relative effect.

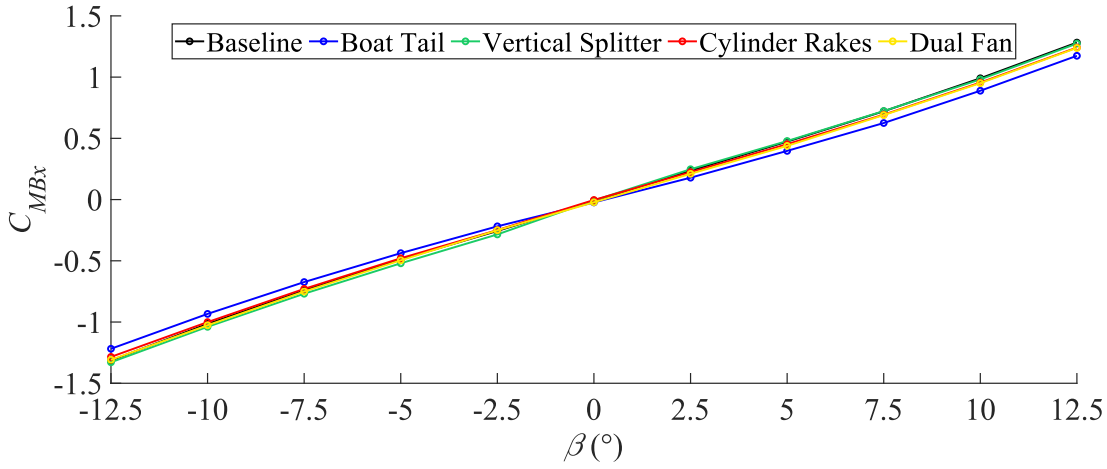

(a)

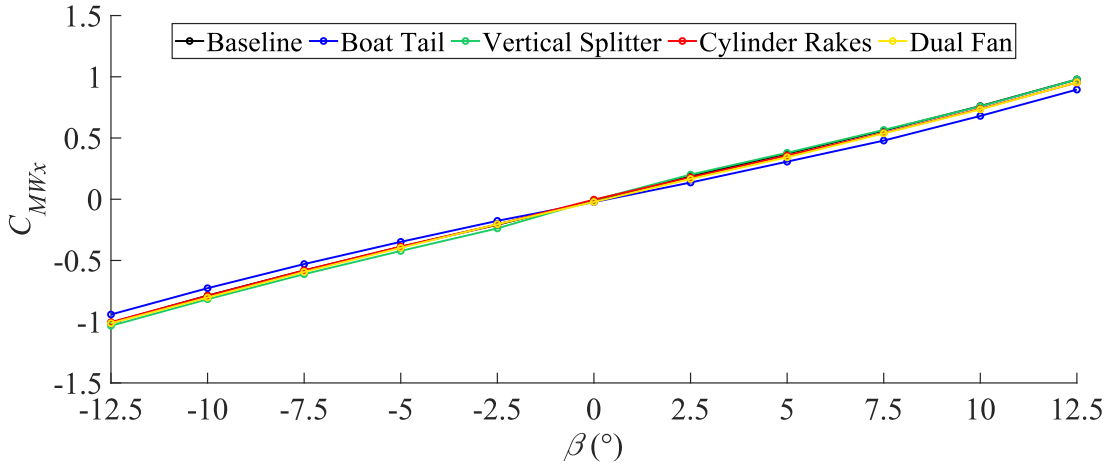

(b)

Figure 38: The roll moment coefficients as a function of yaw angle for the (black) baseline, (blue) boat tail, (green) vertical splitter, (red) cylinder rake, and (yellow) dual fan configurations.

Table 5: The averaged percentage reduction in roll moment coefficient relative to the baseline for both body-indexed and wind-indexed reference frames at yaw ($|\beta| \geq 2.5°$).

	Boat Tail	Vertical Splitter	Cylinder Rakes	Dual Fan
% C_{MBx} Diff	12.2%	-3.0%	3.0%	2.9%
% C_{MWx} Diff	12.9%	-4.4%	2.1%	2.6%

The pitch moment coefficients for all drag reduction devices can be seen in Figure 39. The body-indexed pitch moments (C_{MBy}) are relatively small ($C_{MBy} \sim 0.01$) and are near zero. The trends are also approximately flat across the yaw range. These observations imply that the average force

vector is centered along the height of the body, coplanar to the body-indexed origin. The only outlier for the body-indexed pitch moments was again the boat tail, which had a positive pitch coefficient ranging within $C_{MBy} \approx 0.04$ - 0.07 and a trend that showed a slight increase in the coefficient magnitude with yaw. The effective force vector for this case was therefore implied to be above the body height midplane. The wind-indexed pitch coefficients (C_{MWy}) are nearly identical to the body-indexed but show a sensitivity to yaw, increasing as the angle increases. Since the difference in these wind-indexed pitch coefficients would primarily stem from the addition of side face pressure forces, it indicates that the net force vector of the side face pressures migrates upwards with yaw, albeit minimally.

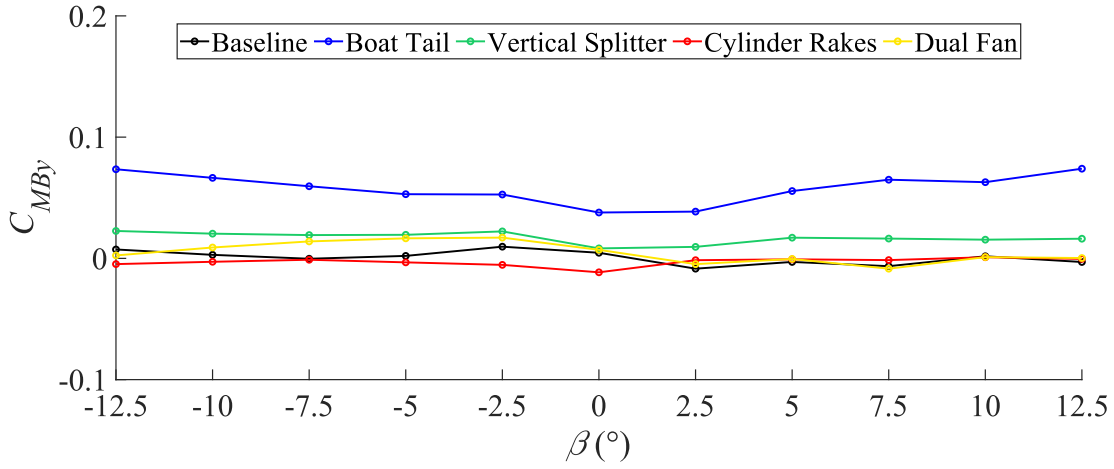

(a)

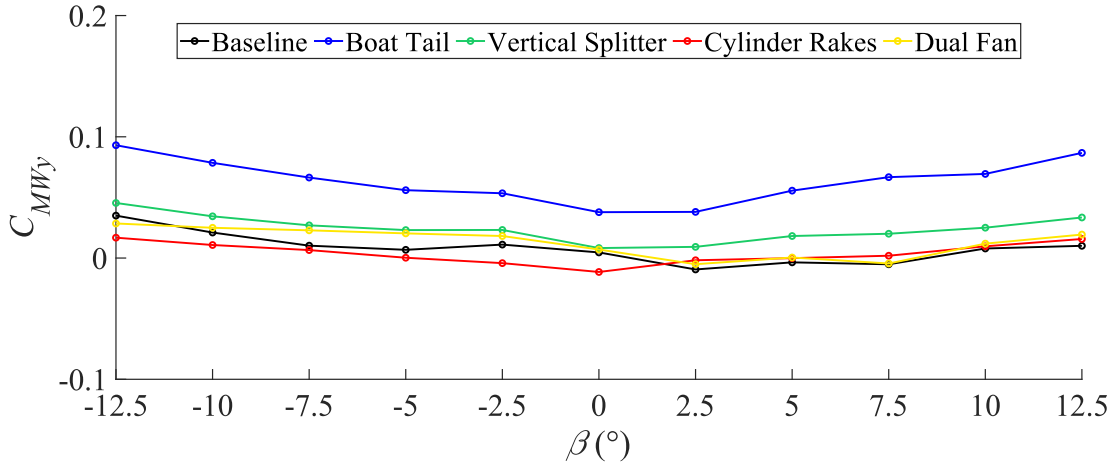

(b)

Figure 39: The pitch moment coefficients as a function of yaw angle for the (black) baseline, (blue) boat tail, (green) vertical splitter, (red) cylinder rake, and (yellow) dual fan configurations.

Lastly, the yaw moments (C_{MBz}, C_{MWz}) and the influences of the drag reduction devices can be seen in Figure 40. The curves again have nearly linear trends with yaw, with a nearly constant slope with when the yaw angle is $|\beta| > 2.5°$. The boat tail is again a slight exception with a nearly linear trend throughout the entire yaw range. Comparing the drag reduction devices, the boat tail performance contradicts previous trends, showing the worst performance relative to the baseline with a 41.7% increase in yaw moment over the baseline. The effective length of the body increases when the boat tail is added, and the length increase is not symmetric about the axis of rotation. These may be contributing factors to the boat tail yaw moment trend. The vertical splitter device

intern has the largest positive influence on yaw moment with a 24.6% reduction. The yaw moments for the two reference frames are identical since the z-axis was the axis of rotation between the reference frames. The averaged reductions in yaw moment for each case can be found Table 6.

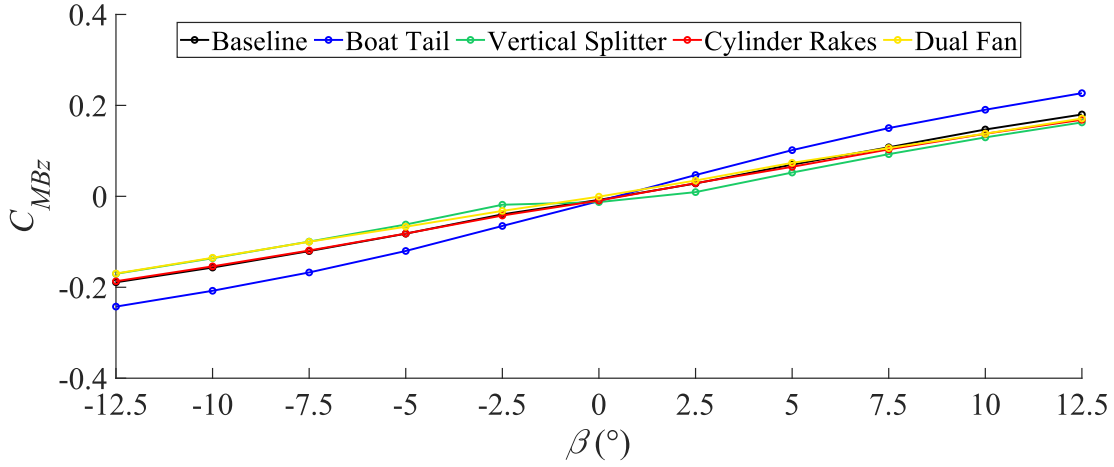

(a)

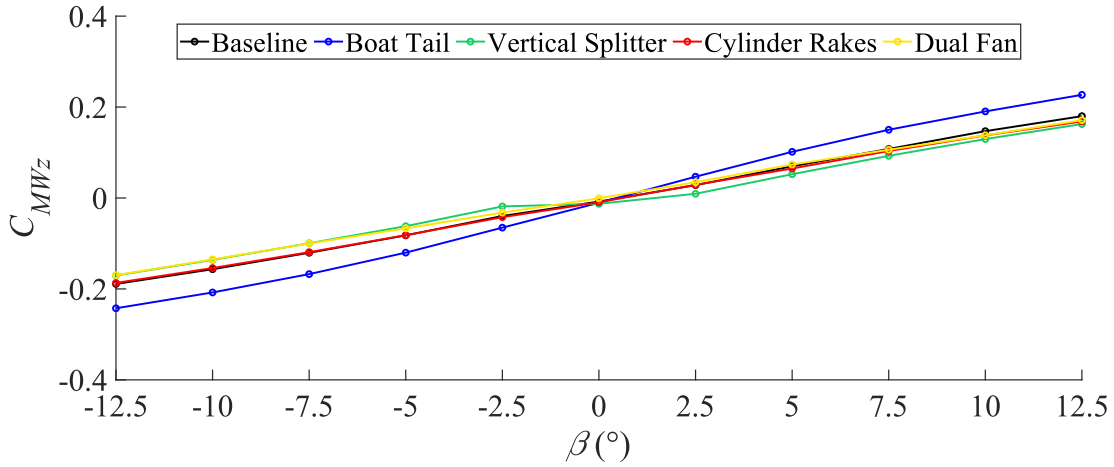

(b)

Figure 40: The yaw moment coefficients as a function of yaw angle for the (black) baseline, (blue) boat tail, (green) vertical splitter, (red) cylinder rake, and (yellow) dual fan configurations.

Table 6: The averaged percentage changes in yaw moment coefficient relative to the baseline for both body-indexed and wind-indexed reference frames at yaw ($|\beta| \geq 2.5°$).

	Boat Tail	Vertical Splitter	Cylinder Rakes	Dual Fan
% C_{MBz} Diff	-41.7%	24.6%	2.0%	6.3%
% C_{MWz} Diff	-41.7%	24.6%	2.0%	6.3%

Similar to the force coefficients, the reference frame of the moment coefficients can be used to evaluate the performance of the devices during a crossflow speed increase. The body-indexed moment coefficients during such an event can be determined by finding the equivalent yaw angle increase. The wind-indexed moment coefficients on the other hand would remain constant and are therefore a better measure of the device effects on aerodynamic moments. The exception to this rule would be for the yaw moment which is constant between reference frame chosen.

5.4 Conclusions

The forces and moments stemming from the aerodynamic properties of a road vehicle are fundamental to its resulting efficiency and stability when driving. Understanding the magnitudes of these forces and how they change with increasing aerodynamic yaw is critical in controlling for and ultimately improving a vehicle's response to the respective loads. To further this understanding, the aerodynamic forces and moments were measured for the square-back Ahmed body baseline across a yaw range of $-12.5° \leq \beta \leq 12.5°$ at $Re_H = 2.7\times10^5$. Additional aerodynamic loads were measured for four different passive wake control devices: a boat tail, a vertical splitter plate at the midspan of the rear face, cylindrical protrusions at the side edges of the rear face, and two fans placed at the upper corners of the rear face.

First the drag forces and side forces were compared for all devices. The drag coefficients and side force coefficients all increased with yaw, the side forces seeing the greater increases. Comparing drag reduction performances of the different configurations, the boat tail device proved to be most effective with an average drag reduction of 26.8% across the measured yaw range. A large divide was present between the performance of the boat tail and the other devices, which ranked: cylinder rakes, dual fans, and vertical splitter in the order of their effective reduction in drag. The magnitude of the drag reduction from baseline remained constant across the yaw range for all devices which implied that the relative effectiveness reduced with yaw angle. The side force coefficients were then compared; the ranking of the devices based on effective reduction was led again by the boat tail with an averaged body-indexed reduction of 12.3%. A large gap was found between it and the other devices. The side force coefficient magnitudes all increased linearly with

yaw angle. Based on the results, the boat tail device would give a clear improvement over the baseline geometry forces, meaning an increased efficiency could be realized if integrated into real road going vehicle geometries. The increase in drag at yaw was then further investigated and was attributed to an induced drag term acting on the body at yaw. It was determined that the induced drag was approximately proportional to the corresponding side force.

The aerodynamic roll moments were also measured, and the coefficients were compared with respect to both the yaw angle and the influence of the various passive devices. The roll moment was the most sensitive to changing yaw angle and the sensitivity was linear in nature. The boat tail again proved to be the most effective a reducing the roll moment with a ~12% reduction over the baseline. The vertical splitter increased the roll moment and the remaining two devices had minimal effects. The pitch moment was near zero and remained mostly constant with yaw angle, only having the boat tail configuration as a prominent outlier, which induced a positive pitching moment. Comparisons of the yaw moment resulted in the largest deviations between device performance and contrary to previous trends, the boat tail had the largest negative effect with an 41.7% increase in yaw moment relative to the baseline. The vertical splitter resulted in a 24.6% reduction which was the most effective out of the three remaining configurations by a large margin. The aerodynamic moments do not directly contribute to vehicle efficiency but would play a large role in vehicle stability. Depending on whether the yaw moment or roll moment is more important to the stability of a vehicle, the chosen drag reduction device could have a large effect. If stability is deemed more important than efficiency, then the optimal configuration may change.

Chapter 6: Conclusions

The scope of this thesis focused on aerodynamic properties of a square-back Ahmed body research model as a way to fundamentally characterize the flow phenomenon for similar shaped road vehicles. The primary focus of the study was the square-back Ahmed body aerodynamic characteristics at yaw which, are underrepresented in current research relative to the zero-yaw condition. This chapter will summarize the results of the two investigations completed; first for Chapter 4 which characterized the wake flow at yaw and then for Chapter 5 which assessed the aerodynamic forces and moments for the geometry at yaw. Recommendations for future work pertaining to the subject matter of this thesis will also be discussed.

6.1 Research Summary

The first research focus of this thesis was the characterization of a square-back Ahmed body wake at yaw. Understanding the fully 3-diemnsional wake structure at yaw gives a fundamental basis for many possible advancements in automotive and bluff body aerodynamics. An increased asymmetry with the yawed wake was discovered, coinciding with increased flow entrainment from the leeward side and overtop of the body. The velocity magnitudes within both of these flow features also increased with yaw angle. Several vortex structures were identified within the wake, the largest structure being a skewed vortex ring positioned downstream of the rear face, surrounded by four streamwise vortices. Spectral analysis of the wake dynamics showed that strength of the wake oscillations increased as yaw increased. The spanwise oscillation of the wake had the largest strength increase as yaw increased. Finally, proper orthogonal decomposition showed that the majority of coherent fluctuations in the yawed wake are concentrated on the windward side of the near wake.

The second research objective of this thesis was measuring and improving the aerodynamic performance of the square-back Ahmed body at yaw. Aerodynamic drag was shown to increase with yaw angle but the rate of increased slowed at larger angles. The side force was much more sensitive to yaw across the measured yaw range and the variations had linear trends from the zero-

yaw angle. While attempting to account for the additional drag at yaw, it was shown that the induced drag was directly proportional to the side force. The roll moment was the largest measured moment followed by the yaw moment. Both moments had near linear trends across the measured yaw range. Finally, four different passive control devices were tested, and the boat tail configuration was identified as the most effective. It netted significant improvements over the baseline configuration as well the other passive devices, highlighted by a ~27% drag reduction. The boat tail did however also lead to an increased yaw moment.

As a whole, the research and conclusions presented within this thesis address a key underlying goal: to improve the aerodynamics of road going vehicles. For this goal, an understanding of the fundamental aerodynamic characteristics at yaw is essential. An increased understanding helps identify aerodynamic properties that require improvement, but it also provides the information required to begin solving these problems. The research presented in Chapters 4 and 5 forms the foundation of knowledge for the characteristics of the square-backed bluff body at yaw. Chapter 4 detailed the yawed wake topology, yawed wake dynamics, and their development as yaw increased. This characterization revealed the aerodynamic properties that directly dictate the forces and moments acting on these vehicles. Chapter 5 then built on this basis, measuring the respective forces and moments to form a complete account of the aerodynamic characteristics at yaw. Finally, using the information provided in Chapter 4, some novel passive control configurations were introduced and tested. The results provide insight into where continued development may be most warranted, creating a springboard for future advances in road vehicle efficiency and stability in crosswinds.

6.2 Future Recommendations

The research presented within this thesis contains many novel observations. The 3D-PTV method used to collect the majority of the data is also only at the beginning stages of its implementation within the flow measurements field. The results therefore set a basis for many avenues of continued research wherefrom meaningful conclusions could still be found.

Much of the advanced analyses focusing on square-back bluff body wake flows have been limited to measurements within a 2D domain. Beginning with the data sets used within this thesis,

many more novel observations can be made with the 3D velocity field information. The zero-yaw wake can be phase averaged which would allow for the study of the more representative averaged flow fields, independent of the bi-stability phenomenon. This could be used to identify phase-dependent vortex structures which could be better contrasted to the yawed vortex structures from Section 4.4. The instantaneous measurements that were time-averaged could be further used to assess the time coherence of the time-averaged vortex structures. Instantaneous data could also be used to identify other instantaneous flow features or to better characterize the spatial distributions of the spectral peaks identified with the wake. The POD analysis could be further exploited by investigating the spectral properties of the temporal modes, and how the temporal evolutions of different modes relate. Such observations could help significantly with identifying the mechanisms underlying each mode. The POD modes could also be to create reduced order models which would help analyze the physical mechanisms of each mode. Finally, an analysis connecting the measurements of Chapters 4 and 5 could be possible by relating the measurable momentum deficit within the wake to the pressure drag of the wake. Care would have to be taken, however, to ensure the full extents of the wakes are measured. All of these analyses could be carried out for the both yawed flow fields and the zero-yaw flow. One recommendation by this author would be to study how the wake flows vary between square-back Ahmed body like geometries and sloped forebody geometries like the Windsor body. Understanding the differences would allow for more certainty in comparisons of the two geometries.

Continuing onto the passive aerodynamic load control, much is still possible on this front. Geometries presented here could be further optimized based on their viability and measured effectiveness. The boat-tail geometry for example could be analyzed by combining the measurement techniques of Chapters 4 and 5, allowing for identification of the drag reduction mechanisms of the geometry, followed by an informed optimization of the shape. Active control strategies can also be explored. The mean flow analysis of Chapter 4 characterized the dominant flow features along with their exact spatial distributions. The initial stages of defining an active control strategy could be greatly augmented by knowing where the most critical regions in the wake are. The active control could then be based on the POD analysis, using a reduced order model to track the wake state. One area of particular interest in flow control of the square-back geometry would be the comparison of the time-averaged structures within the wake and the coherent motions of the POD analysis as these were shown to differ greatly. It may prove beneficial to identify which

of these two flow features can be better utilized by flow control strategies. The primary end goal for all of these analyses would be to extrapolate the results to actual automotive bodies for real world improvements in aerodynamic efficiency, and vehicle stability.

Finally, as was stated, the 3D-PTV measurements themselves are also novel and have the potential to still be improved significantly. The modular system has the inherent advantage of almost unlimited expansion potential given enough resources. Improving the integration of the supply tubing and distributors into the structures could greatly reduce the time requirements and complexity of the setup stages. Expanded systems with more nozzles could then be used to achieve even larger measurement domains or higher seeding densities.

References

Ahmed, S. R., Ramm, G., and Faltin, G. 1984. “Some Salient Features of the Time-Averaged Ground Vehicle Wake.” SAE Technical Paper 840300. https://doi.org/10.4271/840300.

Bonnavion, G., and Cadot, O. 2019. “Boat-Tail Effects on the Global Wake Dynamics of a Flat-Backed Body with Rectangular Section.” Journal of Fluids and Structures 89: 61–71. https://doi.org/10.1016/j.jfluidstructs.2019.01.009.

Bonnavion, G., and Cadot, O. 2018. “Unstable Wake Dynamics of Rectangular Flat-Backed Bluff Bodies with Inclination and Ground Proximity.” Journal of Fluid Mechanics 854: 196–232. https://doi.org/10.1017/jfm.2018.630.

Cadot, O., Evrard, A., and Pastur, L. 2015. “Imperfect Supercritical Bifurcation in a Three-Dimensional Turbulent Wake.” Physical Review E - Statistical, Nonlinear, and Soft Matter Physics 91 (6). https://doi.org/10.1103/PhysRevE.91.063005.

Chometon, F., Strzelecki, A., Ferrand, V., Dechipre, H., Dufour, P. C., Gohlke, M., and Herbert, V.. 2005. “Experimental Study of Unsteady Wakes behind an Oscillating Car Model.” SAE SAE Transactions 114: 665-673. https://doi.org/10.4271/2005-01-0604.

Dalessio, L., Duncan, B., Chang, C., Gargoloff, J. I., and Tate, E. 2017. “Accurate Fuel Economy Prediction via a Realistic Wind Averaged Drag Coefficient.” SAE International Journal of Passenger Cars - Mechanical Systems 10 (1): 265-277. https://doi.org/10.4271/2017-01-1535.

Dalla Longa, L., Evstafyeva, O., and Morgans, A. S. 2019. “Simulations of the Bi-Modal Wake Past Three-Dimensional Blunt Bluff Bodies.” Journal of Fluid Mechanics 866: 791–809. https://doi.org/10.1017/jfm.2019.92.

Duell, E. G., and George, A. R. 1999. “Experimental Study of a Ground Vehicle Body Unsteady Near Wake.” SAE Technical Paper 1999-01-0812. https://doi.org/10.4271/1999-01-0812.

Ebrahimian, M., Sean Sanders, R., and Ghaemi, S. 2019. “Dynamics and Wall Collision of Inertial Particles in a Solid-Liquid Turbulent Channel Flow.” Journal of Fluid Mechanics 881: 872–905. https://doi.org/10.1017/jfm.2019.749.

Evrard, A., Cadot, O., Herbert, V., Ricot, D., Vigneron, R., and Délery, J. 2016. “Fluid Force and Symmetry Breaking Modes of a 3D Bluff Body with a Base Cavity.” Journal of Fluids and Structures 61: 99–114. https://doi.org/10.1016/j.jfluidstructs.2015.12.001.

Fan, Y., Xia, C., Chu, S., Yang, Z., and Cadot, O. 2020. “Experimental and Numerical Analysis of the Bi-Stable Turbulent Wake of a Rectangular Flat-Backed Bluff Body.” Physics of Fluids 32 (10). https://doi.org/10.1063/5.0019794.

Garcia de la Cruz, J., Brackston, R., and Morrison, J. 2017. “Adaptive Base-Flaps Under Variable Cross-Wind.” SAE Technical Paper 2017-01-7000. https://doi.org/10.4271/2017-01-7000.

Gibeau, B., and Ghaemi, S. 2018. “A Modular, 3D-Printed Helium-Filled Soap Bubble Generator for Large-Scale Volumetric Flow Measurements.” Experiments in Fluids 59, 178. https://doi.org/10.1007/s00348-018-2634-9.

Gibeau, B., Gingras, D., and Ghaemi, S. 2020. “Evaluation of a Full-Scale Helium-Filled Soap Bubble Generator.” Experiments in Fluids 61, 28. https://doi.org/10.1007/s00348-019-2853-8.

Gohlke, M., Beaudoin, J. F., Amielh, M., and Anselmet, F. 2007. “Experimental Analysis of Flow Structures and Forces on a 3D-Bluff-Body in Constant Cross-Wind.” Experiments in Fluids 43 (4): 579–94. https://doi.org/10.1007/s00348-007-0341-z.

Gohlke, M., Beaudoin, J. F., Amielh, M., and Anselmet, F. 2008. “Thorough Analysis of Vortical Structures in the Flow around a Yawed Bluff Body.” Journal of Turbulence 9: N15. https://doi.org/10.1080/14685240802010657.

Le Good, G., and Garry, K. 2004. “On the Use of Reference Models in Automotive Aerodynamics.” SAE Technical Paper 2004-01-1308. https://doi.org/10.4271/2004-01-1308.

Grandemange, M., Cadot, O., and Gohlke, M. 2012. “Reflectional Symmetry Breaking of the Separated Flow over Three-Dimensional Bluff Bodies.” Physical Review E - Statistical, Nonlinear, and Soft Matter Physics 86 (3). https://doi.org/10.1103/PhysRevE.86.035302.

Grandemange, M., Cadot, O., Courbois, A., Herbert, V., Ricot, D., Ruiz, T., and Vigneron, R. 2015. “A Study of Wake Effects on the Drag of Ahmed’s Squareback Model at the Industrial Scale.” Journal of Wind Engineering and Industrial Aerodynamics 145: 282–291. https://doi.org/10.1016/j.jweia.2015.03.004.

Grandemange, M., Gohlke, M., and Cadot, O. 2013a. “Bi-Stability in the Turbulent Wake Past Parallelepiped Bodies with Various Aspect Ratios and Wall Effects.” Physics of Fluids 25 (9). https://doi.org/10.1063/1.4820372.

Grandemange, M., Gohlke, M., and Cadot, O. 2013b. “Turbulent Wake Past a Three-Dimensional Blunt Body. Part 1. Global Modes and Bi-Stability.” Journal of Fluid Mechanics 722: 51–84. https://doi.org/10.1017/jfm.2013.83.

Grandemange, M., Gohlke, M., and Cadot, O. 2014. “Turbulent Wake Past a Three-Dimensional Blunt Body. Part 2. Experimental Sensitivity Analysis.” Journal of Fluid Mechanics 752 (5): 439–461. https://doi.org/10.1017/jfm.2014.345.

Heft, A., Indinger, T., and Adams, N. 2012. “Introduction of a New Realistic Generic Car Model for Aerodynamic Investigations.” SAE Technical Paper 2012-01-0168. https://doi.org/10.4271/2012-01-0168.

Heinzel, G., Rudiger, A., and Schilling, R. 2002. “Spectrum and Spectral Density Estimation by the Discrete Fourier Transform (DFT), Including a Comprehensive List of Window Functions and Some New Flat-Top Windows.,” MPG Publication Repositor 1–84.

Howell, J. 2015. “Aerodynamic Drag of Passenger Cars at Yaw.” SAE International Journal of Passenger Cars - Mechanical Systems 8 (1): 306-316. https://doi.org/10.4271/2015-01-1559.

Howell, J., and Le Good, G. 2008. “The Effect of Backlight Aspect Ratio on Vortex and Base Drag for a Simple Car-like Shape.” SAE Technical Paper 2008-01-0737. https://doi.org/10.4271/2008-01-0737.

Hunt, J. C. R., Wray, A. A., and Moin, P. 1988. “Eddies, Streams, and Convergence Zones in Turbulent Flows.” Center for Turbulence Research, Proceedings of the Summer Program, no. 1988: 193–208.

Jeong, J., and Hussain, F. 1995. “On the Identification of a Vortex.” Journal of Fluid Mechanics 285: 69–94. https://doi.org/10.1017/S0022112095000462.

Khalighi, B., Chen, K. H., and Iaccarino, G. 2012. “Unsteady Aerodynamic Flow Investigation around a Simplified Square-Back Road Vehicle with Drag Reduction Devices.” Journal of Fluids Engineering, 134 (6). https://doi.org/10.1115/1.4006643.

Khalighi, B., Zhang, S., Koromilas, C., Balkanyi, S. R., Bernal, L. P., Iaccarino, G., and Moin, P. 2001. "Experimental and Computational Study of Unsteady Wake Flow behind a Bluff Body with a Drag Reduction Device." SAE Technical Paper 2001-01-1042. https://doi.org/10.4271/2001-01-1042.

Krajnović, S., and Davidson, L. 2003. "Numerical Study of the Flow around a Bus-Shaped Body." Journal of Fluids Engineering, 125 (3): 500–509. https://doi.org/10.1115/1.1567305.

Li, R., Borée, J., Noack, B. R., Cordier, L., and Harambat, F. 2019. "Drag Reduction Mechanisms of a Car Model at Moderate Yaw by Bi-Frequency Forcing." Physical Review Fluids 4 (3): 034604. https://doi.org/10.1103/PhysRevFluids.4.034604

Lorite-Díez, M., Jiménez-González, J. I., Pastur, L., Cadot, O., and Martínez-Bazán, C. 2020. "Drag Reduction on a Three-Dimensional Blunt Body with Different Rear Cavities under Cross-Wind Conditions." Journal of Wind Engineering and Industrial Aerodynamics 200. https://doi.org/10.1016/j.jweia.2020.104145.

Lucas, J. M., Cadot, O., Herbert, V., Parpais, S., and Délery, J. 2017. "A Numerical Investigation of the Asymmetric Wake Mode of a Squareback Ahmed Body - Effect of a Base Cavity." Journal of Fluid Mechanics 831: 675–697. https://doi.org/10.1017/jfm.2017.654.

Luchtenburg, D. M., Noack B. R., and Schlegel, M. 2009. "An Introduction to the POD Galerkin Method for Fluid Flows with Analytical Examples and MATLAB Source Codes." Berlin Institute of Technology MB1, Muller-Breslau-Strabe, 11.

Lumley, J. L. 1967. "The Structure of Inhomogeneous Turbulent Flows." Atmospheric Turbulence & Wave Propagation, 166–178.

Mcauliffe, B. R. 2015. "Improving the Aerodynamic Efficiency of Heavy Duty Vehicles: Wind Tunnel Test Results of Trailer-Based Drag-Reduction Technologies." National Research Council of Canada. Aerospace. Aerodynamics Laboratory. https://doi.org/10.4224/21275397.

Mercker, E. 1986. "A Blockage Correction for Automotive Testing in a Wind Tunnel with Closed Test Section." Journal of Wind Engineering and Industrial Aerodynamics 22 (2–3): 149–167. https://doi.org/10.1016/0167-6105(86)90080-2.

National Research Council Canada. 2012. "Review of Aerodynamic Drag Reduction Devices for Heavy Trucks and Buses." Technical Report CSTT-HVC-TR-205.

Östh, J., and Krajnović, S. 2012. “The Flow around a Simplified Tractor-Trailer Model Studied by Large Eddy Simulation.” Journal of Wind Engineering and Industrial Aerodynamics 102: 36–47. https://doi.org/10.1016/j.jweia.2011.12.007.

Östh, J., Noack, B. R., Krajnović, S., Barros, D., and Borée, J. 2014. “On the Need for a Nonlinear Subscale Turbulence Term in POD Models as Exemplified for a High-Reynolds-Number Flow over an Ahmed Body.” Journal of Fluid Mechanics 747 (3): 518–544. https://doi.org/10.1017/jfm.2014.168.

Pavia, G., Passmore, M., and Sardu, C. 2018. “Evolution of the Bi - Stable Wake of a Square-Back Automotive Shape.” Experiments in Fluids 59, 20. https://doi.org/10.1007/s00348-017-2473-0.

Pavia, G., Passmore, M., Varney, M., and Hodgson, G. 2020. “Salient Three-Dimensional Features of the Turbulent Wake of a Simplified Square-Back Vehicle.” Journal of Fluid Mechanics 888. https://doi.org/10.1017/jfm.2020.71.

Perry, AK., Pavia, G., and Passmore, M. 2016. “Influence of Short Rear End Tapers on the Wake of a Simplified Square-Back Vehicle: Wake Topology and Rear Drag.” Experiments in Fluids 57, 169. https://doi.org/10.1007/s00348-016-2260-3.

Raffel, M., Willert, C., Scarano, F., Kähler, C., Wereley, S., and Kompenhans, J. 2018. Particle Image Velocimetry: A Practical Guide. Springer Berlin Heidelberg.

Rouméas, M., Gilliéron, P., and Kourta, A. 2009. “Analysis and Control of the Near-Wake Flow over a Square-Back Geometry.” Computers and Fluids 38 (1): 60–70. https://doi.org/10.1016/j.compfluid.2008.01.009.

Rowin, W. A., and Ghaemi, S. 2019. “Streamwise and Spanwise Slip over a Superhydrophobic Surface.” Journal of Fluid Mechanics 870: 1127–1157. https://doi.org/10.1017/jfm.2019.225.

United States Environmental Protection Agency. 2012. “2017 and Later Model Year Light-Duty Vehicle Greenhouse Gas Emissions and Corporate Average Fuel Economy Standards; Final Rule.” Federal Register 77 (199).

SAE International. 2012. “SAE Wind Tunnel Test Procedure for Trucks and Buses.” J1252.

Schanz, D., Gesemann, S., and Schröder, A. 2016. “Shake-The-Box: Lagrangian Particle Tracking at High Particle Image Densities.” Experiments in Fluids 5, 70. https://doi.org/10.1007/s00348-016-2157-1.

Schanz, D., Gesemann, S., Schröder, A., Wieneke, B., and Novara, M. 2013. "Non-Uniform Optical Transfer Functions in Particle Imaging: Calibration and Application to Tomographic Reconstruction." Measurement Science and Technology 24 (2). https://doi.org/10.1088/0957-0233/24/2/024009.

Schmidt, HJ., Woszidlo, R., Nayeri, C. N., and Paschereit, C. O. 2018. "The Effect of Flow Control on the Wake Dynamics of a Rectangular Bluff Body in Ground Proximity." Experiments in Fluids 59, 107. https://doi.org/10.1007/s00348-018-2560-x.

Sirovich, L. 1987. "Turbulence and the Dynamics of Coherent Structures Part I : Coherent Structures." Quarterly of Applied Mathematics 45 (3): 561–571. https://www.jstor.org/stable/43637457

Sujudi, D., and Haimes, R. 1995. "Identification of Swirling Flow in 3-D Vector Fields." 12th Computational Fluid Dynamics Conference, 792–799. https://doi.org/10.2514/6.1995-1715.

Volpe, R., Devinant, P., and Kourta, A. 2015. "Experimental Characterization of the Unsteady Natural Wake of the Full-Scale Square Back Ahmed Body: Flow Bi-Stability and Spectral Analysis." Experiments in Fluids 56, 99. https://doi.org/10.1007/s00348-015-1972-0.

Volpe, R., Valérie, F., Arthur, D. S., and Luis, L. M. 2014. "Forces and Flow Structures Evolution on a Car Body in a Sudden Crosswind." Journal of Wind Engineering and Industrial Aerodynamics 128: 114–25. https://doi.org/10.1016/j.jweia.2014.03.006.

Welch, P. 1967. "The Use of Fast Fourier Transform for the Estimation of Power Spectra: A Method Based on Time Averaging Over Short, Modified Periodograms" IEEE Transactions on Audio and Electroacoustics, 15 (2): 70-73. 10.1109/TAU.1967.1161901.

Wieneke, B. 2008. "Volume Self-Calibration for 3D Particle Image Velocimetry." Experiments in Fluids 45 (4): 549–56. https://doi.org/10.1007/s00348-008-0521-5.

Wieneke, B. 2013. "Iterative Reconstruction of Volumetric Particle Distribution." Measurement Science and Technology 24 (2). https://doi.org/10.1088/0957-0233/24/2/024008.

Zhu, HY., Wang, CY., Wang, HP., and Wang, JJ. 2017. "Tomographic PIV Investigation on 3D Wake Structures for Flow over a Wall-Mounted Short Cylinder." Journal of Fluid Mechanics 831: 743–778. https://doi.org/10.1017/jfm.2017.647.

Appendix A: Figure Reuse Permissions

The following Appendix contains the permissions necessary to reuse certain figures presented within Chapter 1.

Proof of permission to reuse Figure 3 follows.

SPRINGER NATURE

Thank you for your order!

Dear Mr. Adriaan Booysen,

Thank you for placing your order through Copyright Clearance Center's RightsLink® service.

Order Summary

Licensee:	Mr. Adriaan Booysen
Order Date:	Apr 19, 2021
Order Number:	5052830704402
Publication:	Experiments in Fluids
Title:	Experimental characterization of the unsteady natural wake of the full-scale square back Ahmed body: flow bi-stability and spectral analysis
Type of Use:	Thesis/Dissertation
Order Total:	0.00 CAD

View or print complete details of your order and the publisher's terms and conditions.

Sincerely,

Copyright Clearance Center

Tel: +1-855-239-3415 / +1-978-646-2777
customercare@copyright.com
https://myaccount.copyright.com

Copyright Clearance Center RightsLink®

Proof of permission to reuse Figure 4 follows.

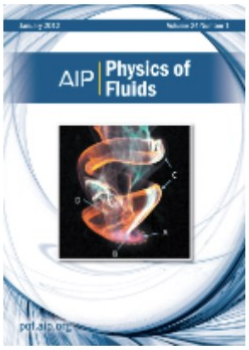

Thank you for your order!

Dear Mr. Adriaan Booysen,

Thank you for placing your order through Copyright Clearance Center's RightsLink® service.

Order Summary

Licensee:	Mr. Adriaan Booysen
Order Date:	Apr 29, 2021
Order Number:	5058410913117
Publication:	Physics of Fluids
Title:	Bi-stability in the turbulent wake past parallelepiped bodies with various aspect ratios and wall effects
Type of Use:	Thesis/Dissertation
Order Total:	0.00 CAD

View or print complete details of your order and the publisher's terms and conditions.

Sincerely,

Copyright Clearance Center

Tel: +1-855-239-3415 / +1-978-646-2777
customercare@copyright.com
https://myaccount.copyright.com

Copyright Clearance Center RightsLink®

Proof of permission to reuse Figure 6 follows.

Thank you for your order!

Dear Mr. Adriaan Booysen,

Thank you for placing your order through Copyright Clearance Center's RightsLink® service.

Order Summary

Licensee:	Mr. Adriaan Booysen
Order Date:	Apr 29, 2021
Order Number:	5058411368174
Publication:	Journal of Wind Engineering and Industrial Aerodynamics
Title:	Drag reduction on a three-dimensional blunt body with different rear cavities under cross-wind conditions
Type of Use:	reuse in a thesis/dissertation
Order Total:	0.00 CAD

View or print complete details of your order and the publisher's terms and conditions.

Sincerely,

Copyright Clearance Center

Tel: +1-855-239-3415 / +1-978-646-2777
customercare@copyright.com
https://myaccount.copyright.com

Copyright Clearance Center RightsLink®

Appendix B: Technical Drawings

The following appendix contains the drawing package for the half-scale Ahmed body used for the experiments conducted for this thesis. It also contains drawings of assembly dimensions for the HFSB system and the assembled nozzle. Lastly, it contains drawings for the passive control devices.

B1. Ahmed Body Drawing Package

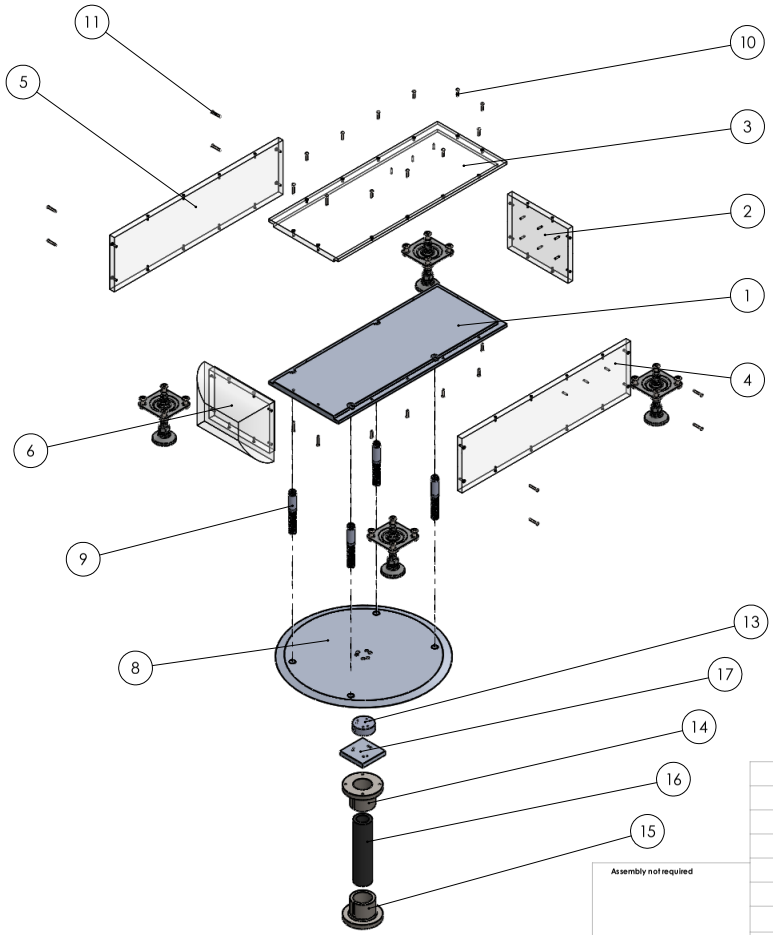

ITEM NO.	PART NUMBER	Material	QTY.
1	Bottom Plate - Ahmed Body	Aluminum	1
2	Rear Plate - Ahmed Body	Acrylic	1
3	Top Plate - Ahmed Body	Acrylic	1
4	Orifice Side Plate - Ahmed Body	Acylic	1
5	Side Plate - Ahmed Body	Acrylic	1
6	Nose Cone - Ahmed Body	Acrylic	1
7	Boundary Plate Sub Assembly		1
8	Load Sensor Plate - Ahmed Body	Aluminum	1
9	Wired Body Post - Ahmed Body		4
10	CR-FHMS 0.125-44x0.625x0.625-N		20
11	CR-FHMS 0.125-44x0.875x0.875-N		12
12	B18.6.7M - M3 x 0.5 x 5 Type I Cross Recessed FHMS --5N		6
13	Mini45		1
14	Load Cell Mount		1
15	Load Cell Mount2		1
16	Stinger_1.5in	Fan (2)	1
17	ConnectionPlate	6061 Alloy	1

UNLESS OTHERWISE SPECIFIED:
DIMENSIONS ARE IN INCHES
TOLERANCES:
FRACTIONAL ±
ANGULAR: MACH ± BEND ±
TWO PLACE DECIMAL ±
THREE PLACE DECIMAL ±
INTERPRET GEOMETRIC TOLERANCING PER:
MATERIAL
FINISH
NEXT ASSY | USED ON
APPLICATION | DO NOT SCALE DRAWING

	NAME	DATE
DRAWN		
CHECKED		
ENG APPR.		
MFG APPR.		
Q.A.		
COMMENTS:		

TITLE: Exploded View W/O Boundary Plate Sub Assembly

SIZE B | DWG. NO. Square Back Ahmed Body EXP | REV

SCALE: 1:20 | WEIGHT: | SHEET 1 OF 1

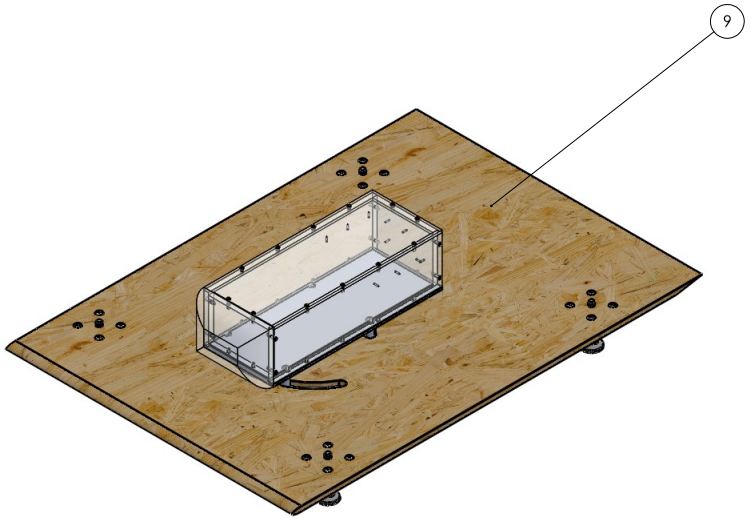

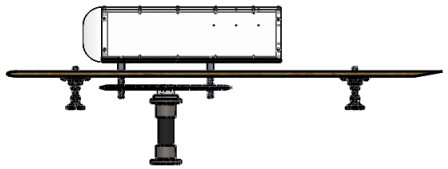

ITEM NO.	PART NUMBER	Material	QTY.
1	Bottom Plate - Ahmed Body	Aluminum	1
2	Rear Plate - Ahmed Body	Acrylic	1
3	Top Plate - Ahmed Body	Acrylic	1
4	Orifice Side Plate - Ahmed Body	Acylic	1
5	Side Plate - Ahmed Body	Acrylic	1
6	Nose Cone - Ahmed Body	Acrylic	1
7	Load Sensor Plate - Ahmed Body	Aluminum	1
8	Wired Body Post - Ahmed Body		4
9	Boundary Plate Sub Assembly		1
10	Mini45		1
11	Load Cell Mount		1
12	Load Cell Mount2		1
13	Stinger_1.5in	Fan (2)	1
14	ConnectionPlate	6061 Alloy	1
15	CR-FHMS 0.125-40x0.625x0.625-N		20
16	CR-FHMS 0.125-40x0.875x0.875-N		12
17	B18.6.7M - M3 x 0.5 x 13 Type I Cross Recessed FHMS --13N		6
18	B18.3.1M - 3 x 0.5 x 6 Hex SHCS --6NHX		6

UNLESS OTHERWISE SPECIFIED:
DIMENSIONS ARE IN INCHES
TOLERANCES:
FRACTIONAL ±
ANGULAR: MACH ± BEND ±
TWO PLACE DECIMAL ±
THREE PLACE DECIMAL ±
INTERPRET GEOMETRIC TOLERANCING PER:
MATERIAL
FINISH
NEXT ASSY | USED ON
APPLICATION | DO NOT SCALE DRAWING

	NAME	DATE
DRAWN		
CHECKED		
ENG APPR.		
MFG APPR.		
Q.A.		
COMMENTS:		

TITLE: Square BAck Ahmed Body with Boundary Plate Sub Assembly ISO

SIZE	DWG. NO.	REV
B	Square Back Ahmed Body ISO	
SCALE: 1:10	WEIGHT:	SHEET 1 OF 1

ITEM NO.	PART NUMBER	Material	QTY.
1	Boundary Layer Plate - Ahmed Body	Medium Density Fibreboard	1
2	6577K23		4
3	CR-FHM1 0.3125-24x0.875x0.875-N		16
4	HNUT 0.3125-24-D-N		16

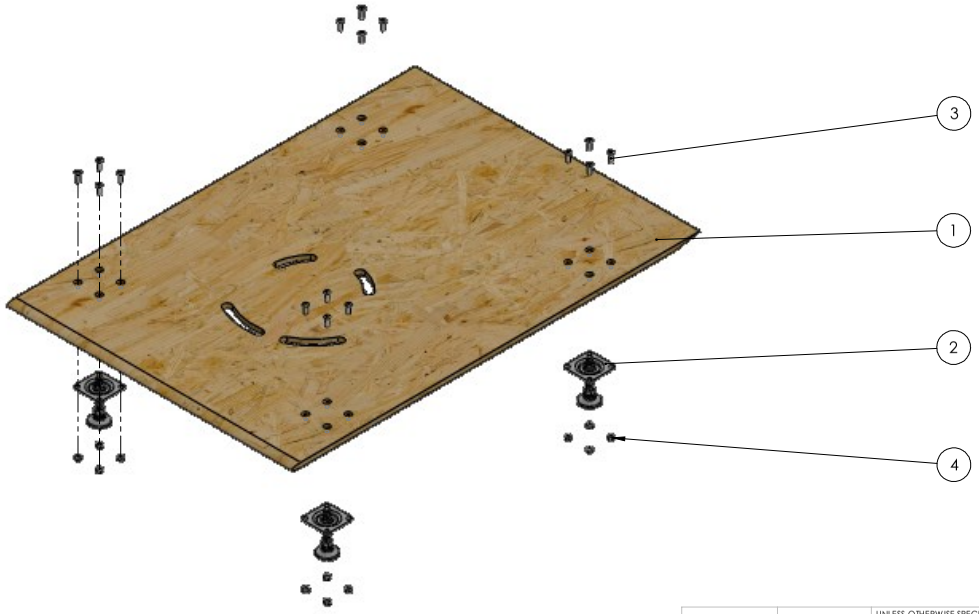

		UNLESS OTHERWISE SPECIFIED:		NAME	DATE
		DIMENSIONS ARE IN INCHES TOLERANCES: FRACTIONAL ± ANGULAR: MACH ± BEND ± TWO PLACE DECIMAL ± THREE PLACE DECIMAL ±	DRAWN		
			CHECKED		
			ENG APPR.		
			MFG APPR.		
		INTERPRET GEOMETRIC TOLERANCING PER:	Q.A.		
		MATERIAL	COMMENTS:		
NEXT ASSY	USED ON	FINISH			
APPLICATION		DO NOT SCALE DRAWING			

TITLE: Boundary Plate Sub Assembly ISO

SIZE	DWG. NO.	REV
B	Boundary Plate Sub Assembly	

SCALE: 1:20 WEIGHT: SHEET 1 OF 1

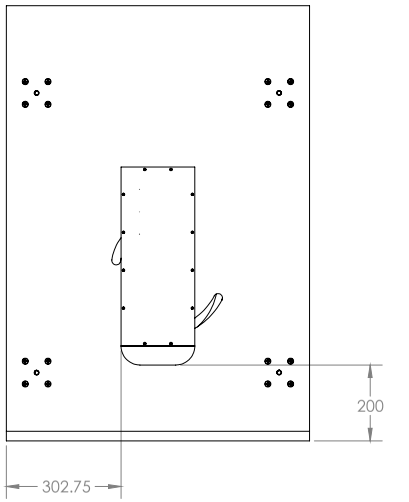

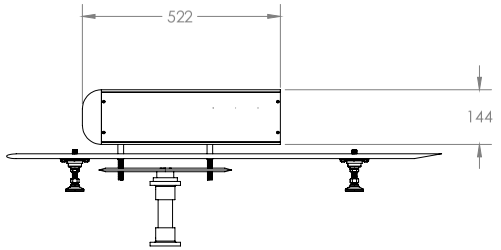

Assembly isn't required, drawings are supplementary and show dimensions of ahmed body

		UNLESS OTHERWISE SPECIFIED:		NAME	DATE
		DIMENSIONS ARE IN INCHES TOLERANCES: FRACTIONAL ± ANGULAR: MACH ± BEND ± TWO PLACE DECIMAL ± THREE PLACE DECIMAL ±	DRAWN		
			CHECKED		
			ENG APPR.		
			MFG APPR.		
		INTERPRET GEOMETRIC TOLERANCING PER:	Q.A.		
		MATERIAL	COMMENTS:		
NEXT ASSY	USED ON	FINISH			
APPLICATION		DO NOT SCALE DRAWING			

TITLE:
Square Back Ahymed Body
Assembly Dimensions

SIZE	DWG. NO.	REV
B	Square Back Ahmed Body	
SCALE: 1:20	WEIGHT:	SHEET 1 OF 1

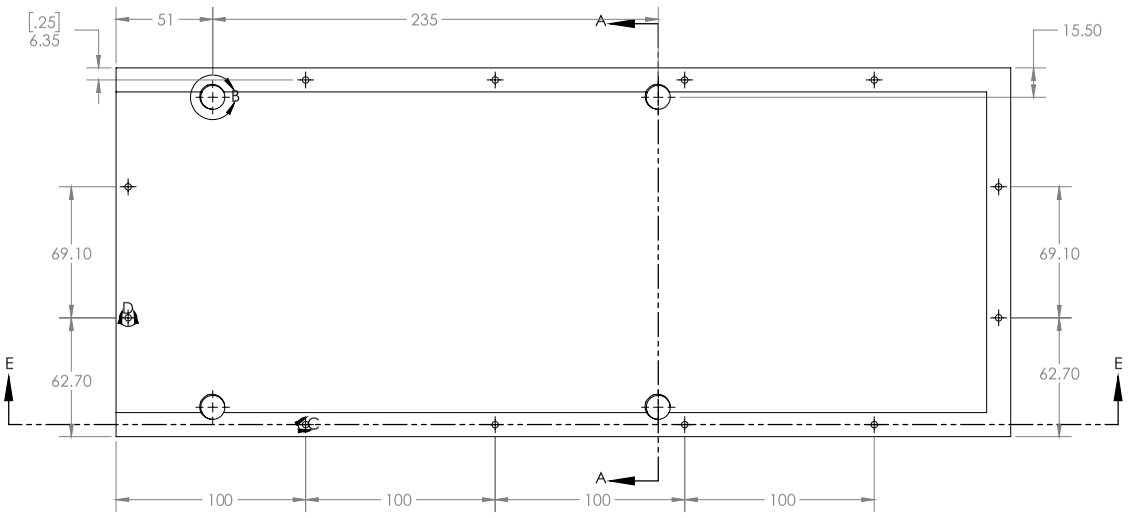

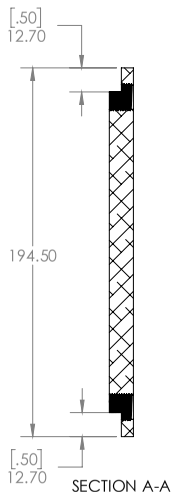

SECTION A-A

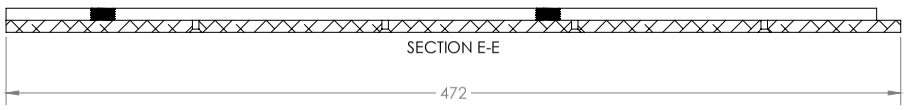

SECTION E-E

DETAIL B
SCALE 1 : 1

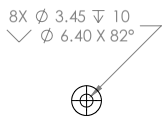

DETAIL C
SCALE 1 : 1

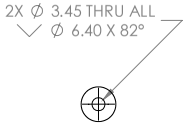

DETAIL D
SCALE 1 : 1

All holes were made in imperial sizes

Plate thickness is measured in imperial units

Detail B Hole is tapped with 1/2"-20 thread

		UNLESS OTHERWISE SPECIFIED:		NAME	DATE
		DIMENSIONS ARE IN INCHES TOLERANCES: FRACTIONAL ± ANGULAR: MACH ± BEND ± TWO PLACE DECIMAL ± THREE PLACE DECIMAL ±	DRAWN		
			CHECKED		
			ENG APPR.		
			MFG APPR.		
		INTERPRET GEOMETRIC TOLERANCING PER:	Q.A.		
		MATERIAL Aluminum (6061)	COMMENTS:		
NEXT ASSY	USED ON	FINISH			
APPLICATION		DO NOT SCALE DRAWING			

TITLE: Bottom Plate

SIZE	DWG. NO.	REV
B	Bottom Plate - Ahmed Body	

SCALE: 1:2 | WEIGHT: | SHEET 1 OF 1

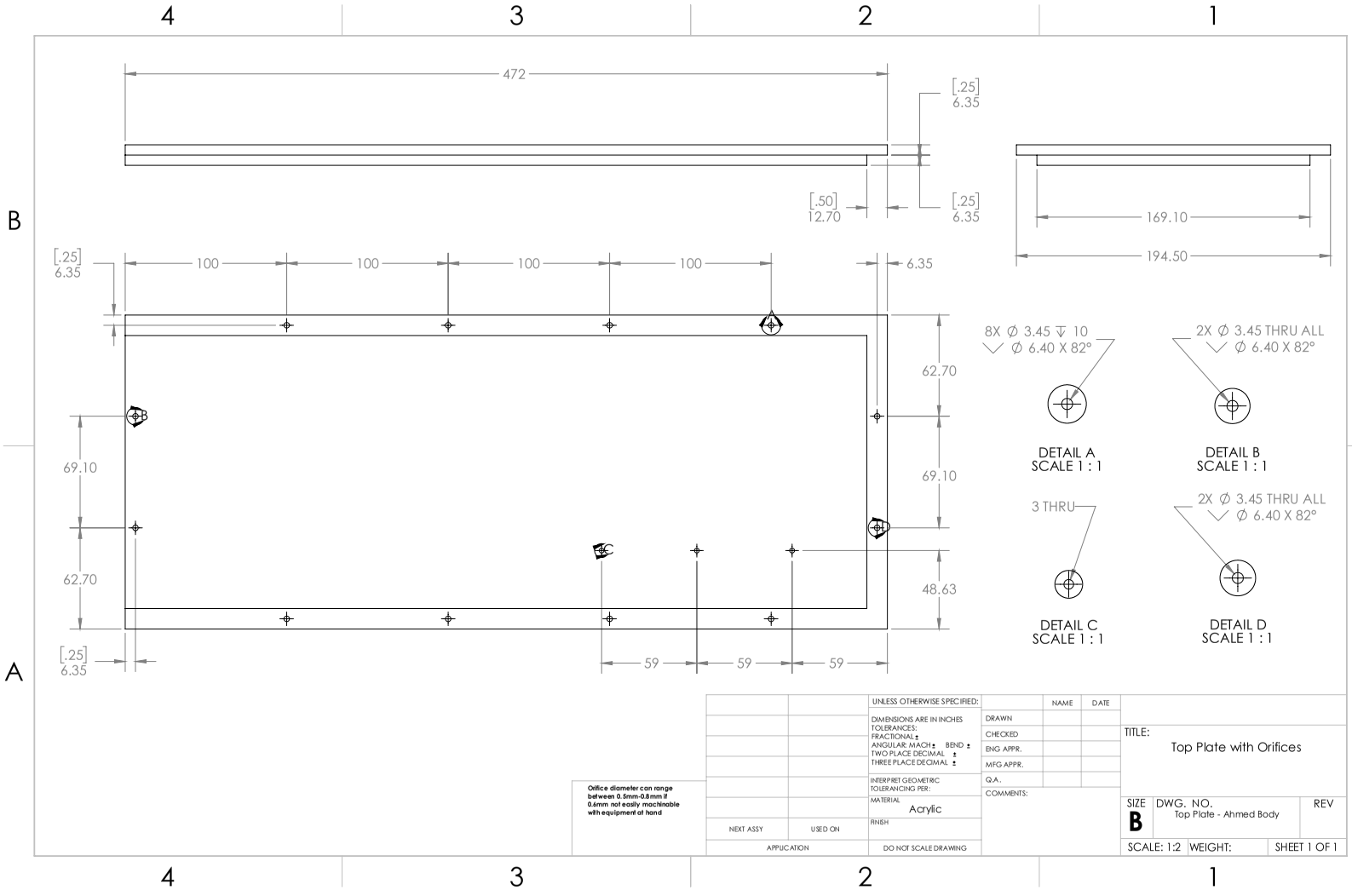
4
3
2
1
B
A
472
[.25]
6.35
[.50]
12.70
[.25]
6.35
169.10
194.50
[.25]
6.35
100
100
100
100
6.35
62.70
69.10
69.10
62.70
48.63
59
59
59
8X Ø 3.45 ↧ 10
Ø 6.40 X 82°
DETAIL A
SCALE 1 : 1
2X Ø 3.45 THRU ALL
Ø 6.40 X 82°
DETAIL B
SCALE 1 : 1
3 THRU
DETAIL C
SCALE 1 : 1
2X Ø 3.45 THRU ALL
Ø 6.40 X 82°
DETAIL D
SCALE 1 : 1
Orifice diameter can range between 0.5mm-0.8mm if 0.6mm not easily machinable with equipment at hand
UNLESS OTHERWISE SPECIFIED:
DIMENSIONS ARE IN INCHES
TOLERANCES:
FRACTIONAL ±
ANGULAR: MACH ± BEND ±
TWO PLACE DECIMAL ±
THREE PLACE DECIMAL ±
INTERPRET GEOMETRIC TOLERANCING PER:
MATERIAL
Acrylic
FINISH
NEXT ASSY
USED ON
APPLICATION
DO NOT SCALE DRAWING
NAME
DATE
DRAWN
CHECKED
ENG APPR.
MFG APPR.
Q.A.
COMMENTS:
TITLE:
Top Plate with Orifices
SIZE
B
DWG. NO.
Top Plate - Ahmed Body
REV
SCALE: 1:2
WEIGHT:
SHEET 1 OF 1

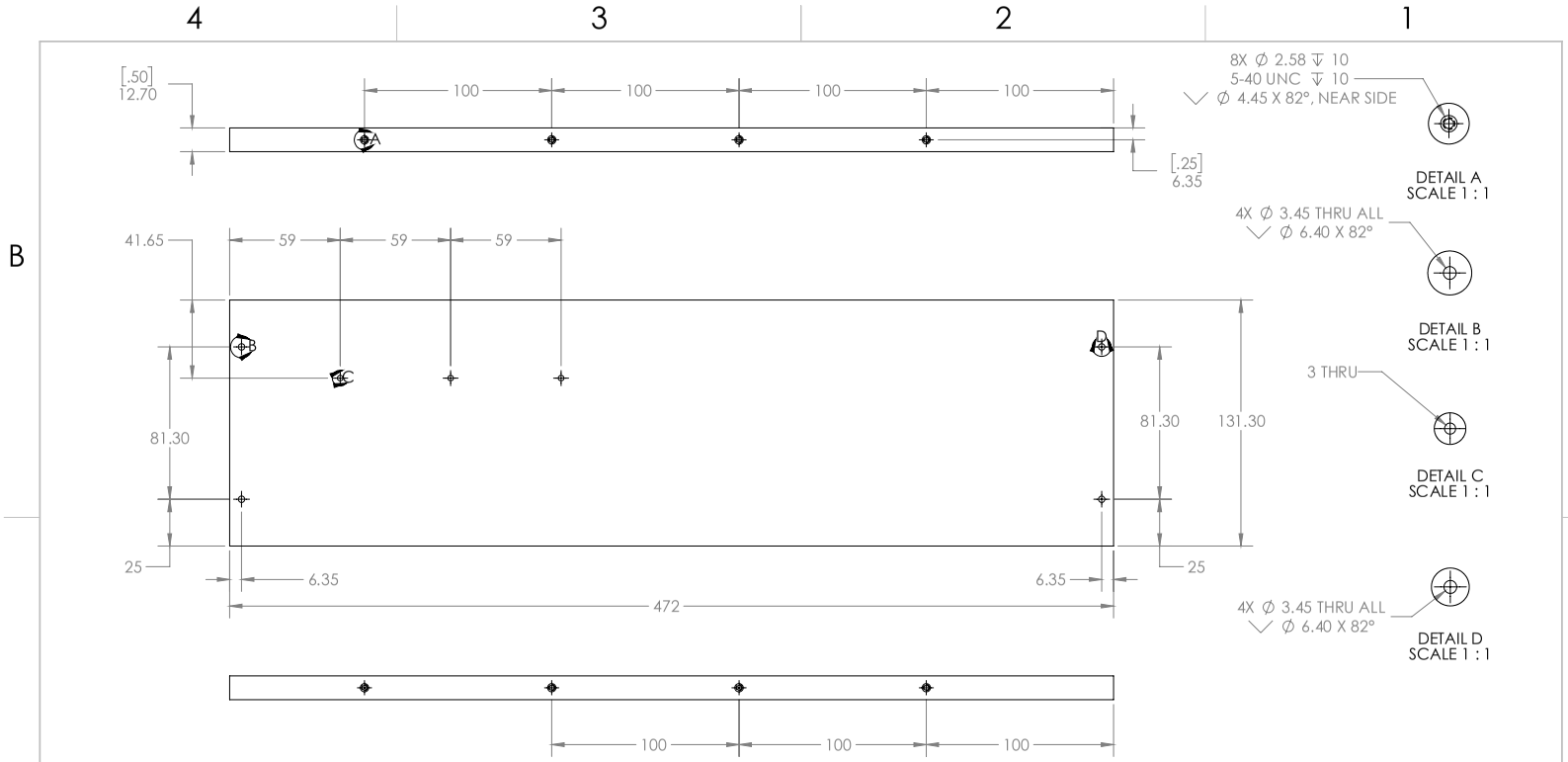

Orifice diameter can range between 0.5mm-0.8mm if 0.6mm not easily machinable with equipment at hand

				NAME	DATE
		UNLESS OTHERWISE SPECIFIED:			
		DIMENSIONS ARE IN INCHES TOLERANCES: FRACTIONAL ± ANGULAR: MACH ± BEND ± TWO PLACE DECIMAL ± THREE PLACE DECIMAL ±	DRAWN		
			CHECKED		
			ENG APPR.		
			MFG APPR.		
		INTERPRET GEOMETRIC TOLERANCING PER:	Q.A.		
		MATERIAL Acrylic	COMMENTS:		
NEXT ASSY	USED ON	FINISH			
APPLICATION		DO NOT SCALE DRAWING			

TITLE:
Side Plate with Microphone Orifices

SIZE	DWG. NO.	REV
B	Orifice Side Plate - Ahmed Body	
SCALE: 1:2	WEIGHT:	SHEET 1 OF 1

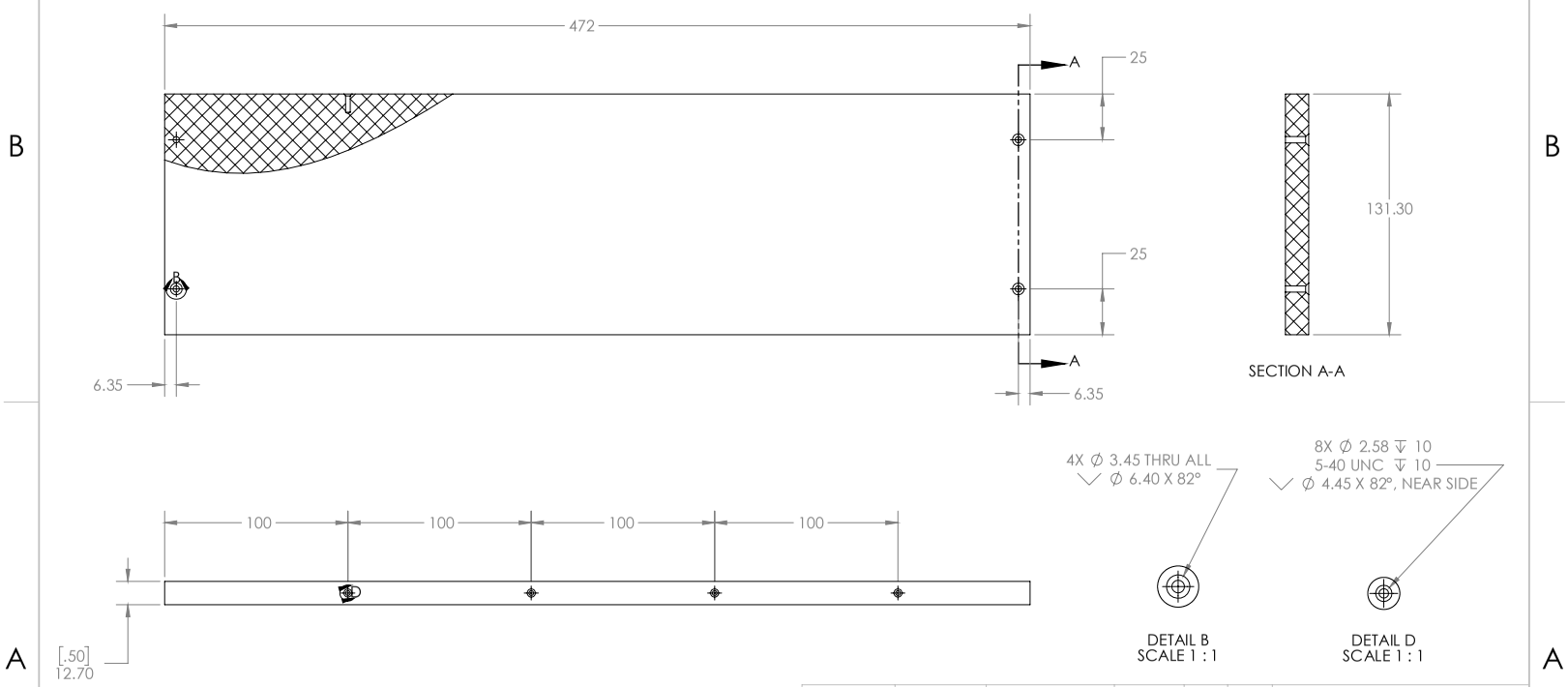

		UNLESS OTHERWISE SPECIFIED:		NAME	DATE
		DIMENSIONS ARE IN INCHES TOLERANCES: FRACTIONAL ± ANGULAR: MACH ± BEND ± TWO PLACE DECIMAL ± THREE PLACE DECIMAL ±	DRAWN		
			CHECKED		
			ENG APPR.		
			MFG APPR.		
		INTERPRET GEOMETRIC TOLERANCING PER:	Q.A.		
		MATERIAL Acrylic	COMMENTS:		
NEXT ASSY	USED ON	FINISH			
APPLICATION		DO NOT SCALE DRAWING			

TITLE: Side Plate w/o Orifices

SIZE	DWG. NO.	REV
B	Side Plate - Ahmed Body	

SCALE: 1:2 | WEIGHT: | SHEET 1 OF 1

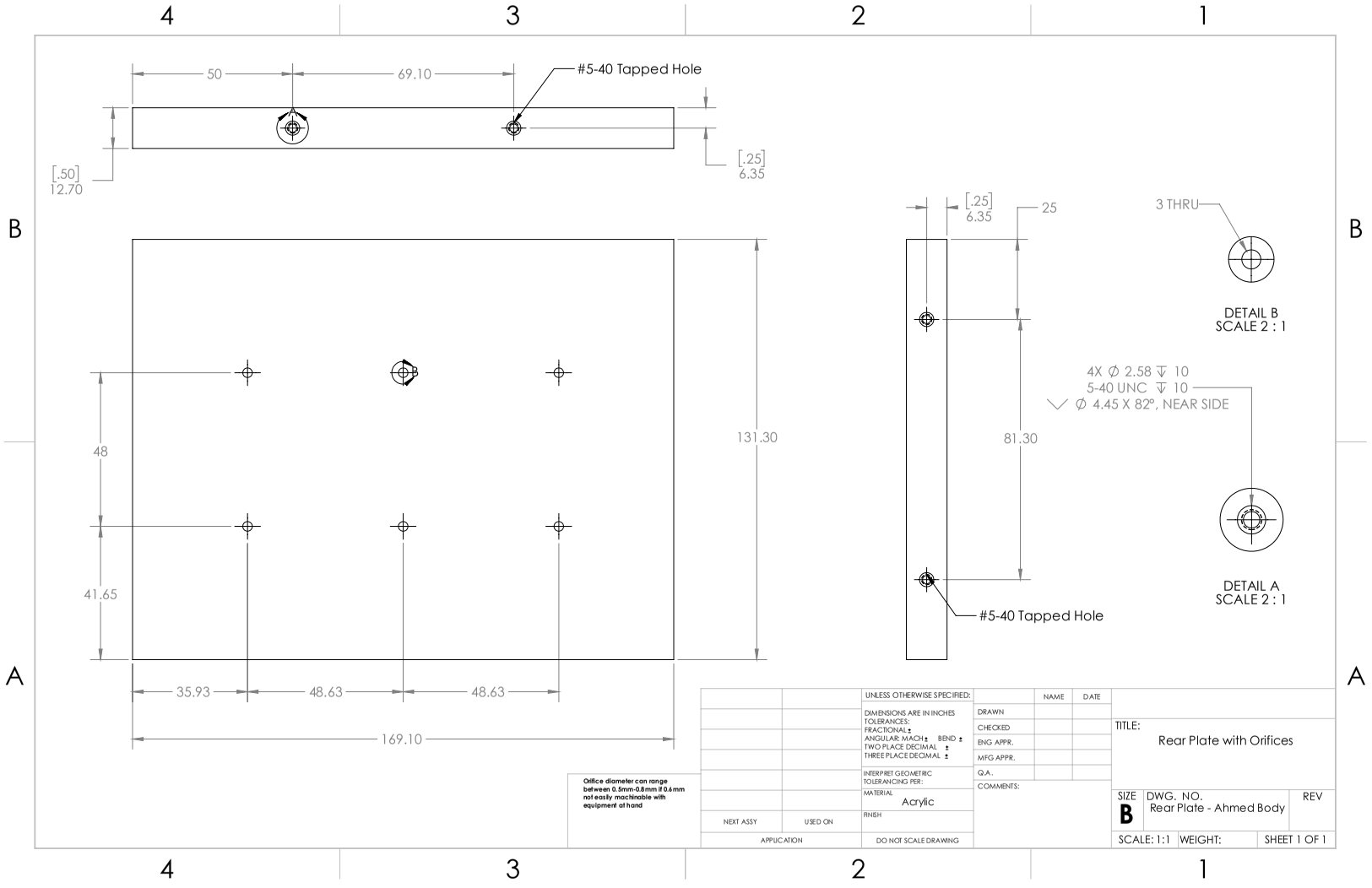
4
3
2
1
B
A
50
69.10
#5-40 Tapped Hole
[.50]
12.70
[.25]
6.35
48
41.65
131.30
35.93
48.63
48.63
169.10
[.25]
6.35
25
3 THRU
DETAIL B
SCALE 2 : 1
4X Ø 2.58 ↧ 10
5-40 UNC ↧ 10
⌵ Ø 4.45 X 82°, NEAR SIDE
81.30
DETAIL A
SCALE 2 : 1
#5-40 Tapped Hole
Orifice diameter can range between 0.5mm-0.8mm if 0.6mm not easily machinable with equipment at hand
UNLESS OTHERWISE SPECIFIED:
DIMENSIONS ARE IN INCHES
TOLERANCES:
FRACTIONAL ±
ANGULAR: MACH ± BEND ±
TWO PLACE DECIMAL ±
THREE PLACE DECIMAL ±
INTERPRET GEOMETRIC TOLERANCING PER:
MATERIAL
Acrylic
FINISH
NEXT ASSY
USED ON
APPLICATION
DO NOT SCALE DRAWING
NAME
DATE
DRAWN
CHECKED
ENG APPR.
MFG APPR.
Q.A.
COMMENTS:
TITLE:
Rear Plate with Orifices
SIZE
B
DWG. NO.
Rear Plate - Ahmed Body
REV
SCALE: 1:1
WEIGHT:
SHEET 1 OF 1

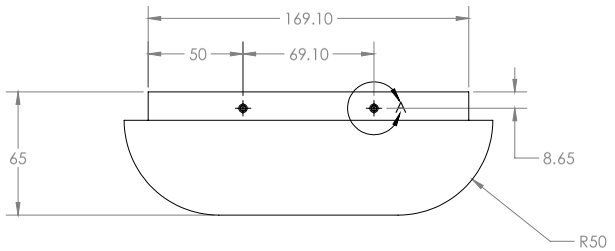

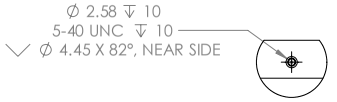

DETAIL A
SCALE 2 : 3

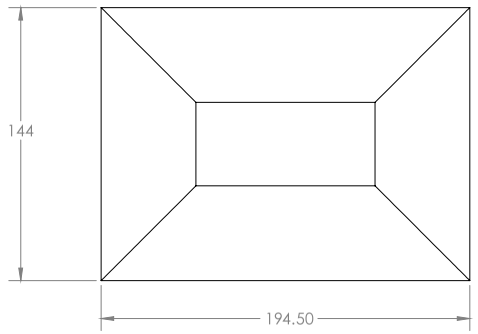

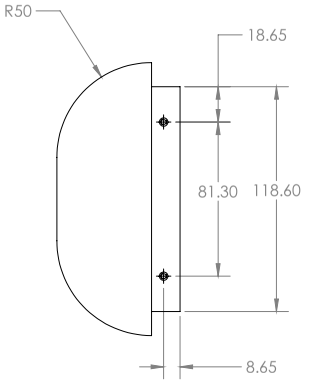

		UNLESS OTHERWISE SPECIFIED:		NAME	DATE
		DIMENSIONS ARE IN INCHES TOLERANCES: FRACTIONAL ± ANGULAR: MACH ± BEND ± TWO PLACE DECIMAL ± THREE PLACE DECIMAL ±	DRAWN		
			CHECKED		
			ENG APPR.		
			MFG APPR.		
		INTERPRET GEOMETRIC TOLERANCING PER:	Q.A.		
		MATERIAL Acrylic	COMMENTS:		
NEXT ASSY	USED ON	FINISH			
APPLICATION		DO NOT SCALE DRAWING			

TITLE: Nose Cone

SIZE	DWG. NO.	REV
B	Nose Cone - Ahmed Body	
SCALE: 1:3	WEIGHT:	SHEET 1 OF 1

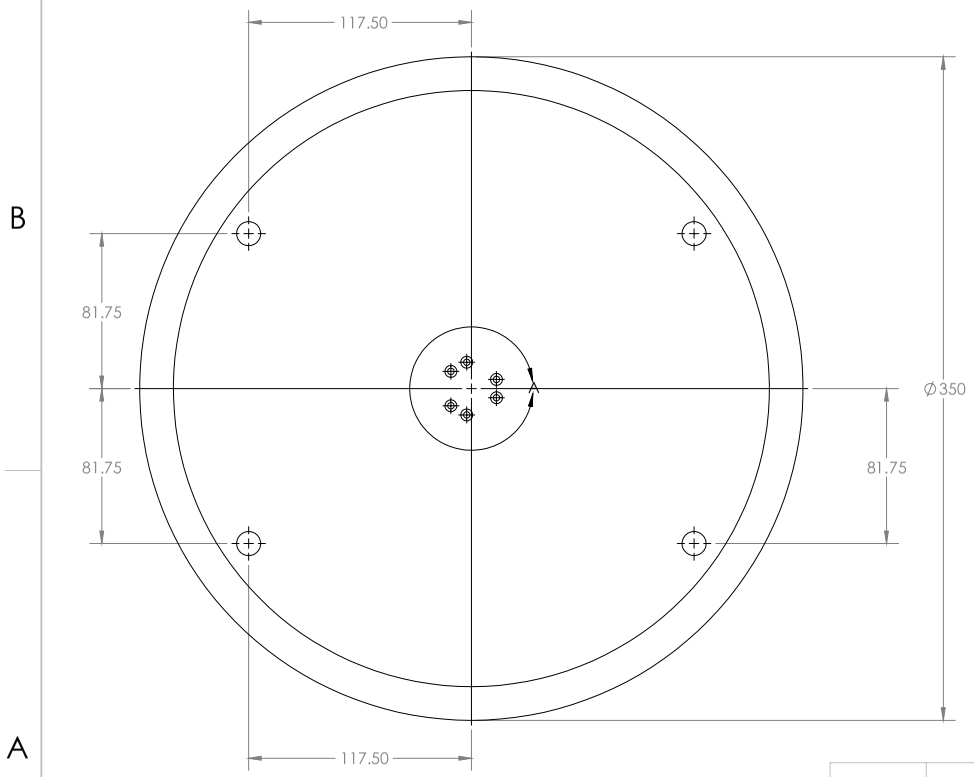

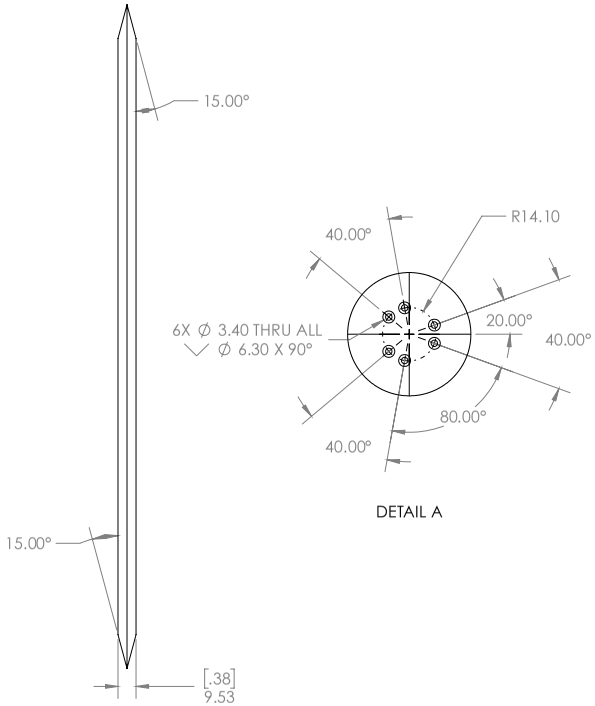

DETAIL A

		UNLESS OTHERWISE SPECIFIED:		NAME	DATE
		DIMENSIONS ARE IN INCHES TOLERANCES: FRACTIONAL ± ANGULAR: MACH ± BEND ± TWO PLACE DECIMAL ± THREE PLACE DECIMAL ±	DRAWN		
			CHECKED		
			ENG APPR.		
			MFG APPR.		
		INTERPRET GEOMETRIC TOLERANCING PER:	Q.A.		
		MATERIAL Aluminum (6061)	COMMENTS:		
NEXT ASSY	USED ON	FINISH			
APPLICATION		DO NOT SCALE DRAWING			

TITLE: Load Sensor Plate

SIZE	DWG. NO.	REV
B	Load Sensor Plate - Ahmed Body	

SCALE: 1:2 | WEIGHT: | SHEET 1 OF 1

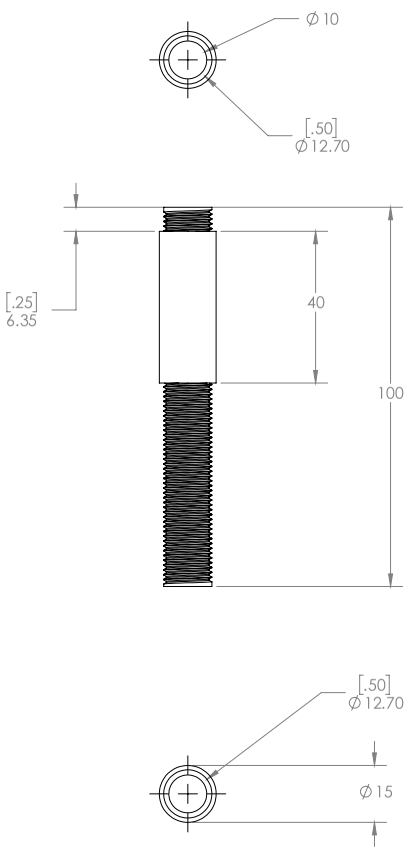

Material not specified, as long as tolerances allow for assembly and structural rigidity material is arbitrary

Internal hole diameter is also loose depending on machining cost

Thread is 1/2"-20

		UNLESS OTHERWISE SPECIFIED:		NAME	DATE
		DIMENSIONS ARE IN INCHES TOLERANCES: FRACTIONAL ± ANGULAR: MACH ± BEND ± TWO PLACE DECIMAL ± THREE PLACE DECIMAL ±	DRAWN		
			CHECKED		
			ENG APPR.		
			MFG APPR.		
		INTERPRET GEOMETRIC TOLERANCING PER:	Q.A.		
		MATERIAL	COMMENTS:		
NEXT ASSY	USED ON	FINISH			
APPLICATION		DO NOT SCALE DRAWING			

TITLE: Wired Body Post

SIZE	DWG. NO.	REV
B	Wired Body Post - Ahmed Body	
SCALE: 1:1	WEIGHT:	SHEET 1 OF 1

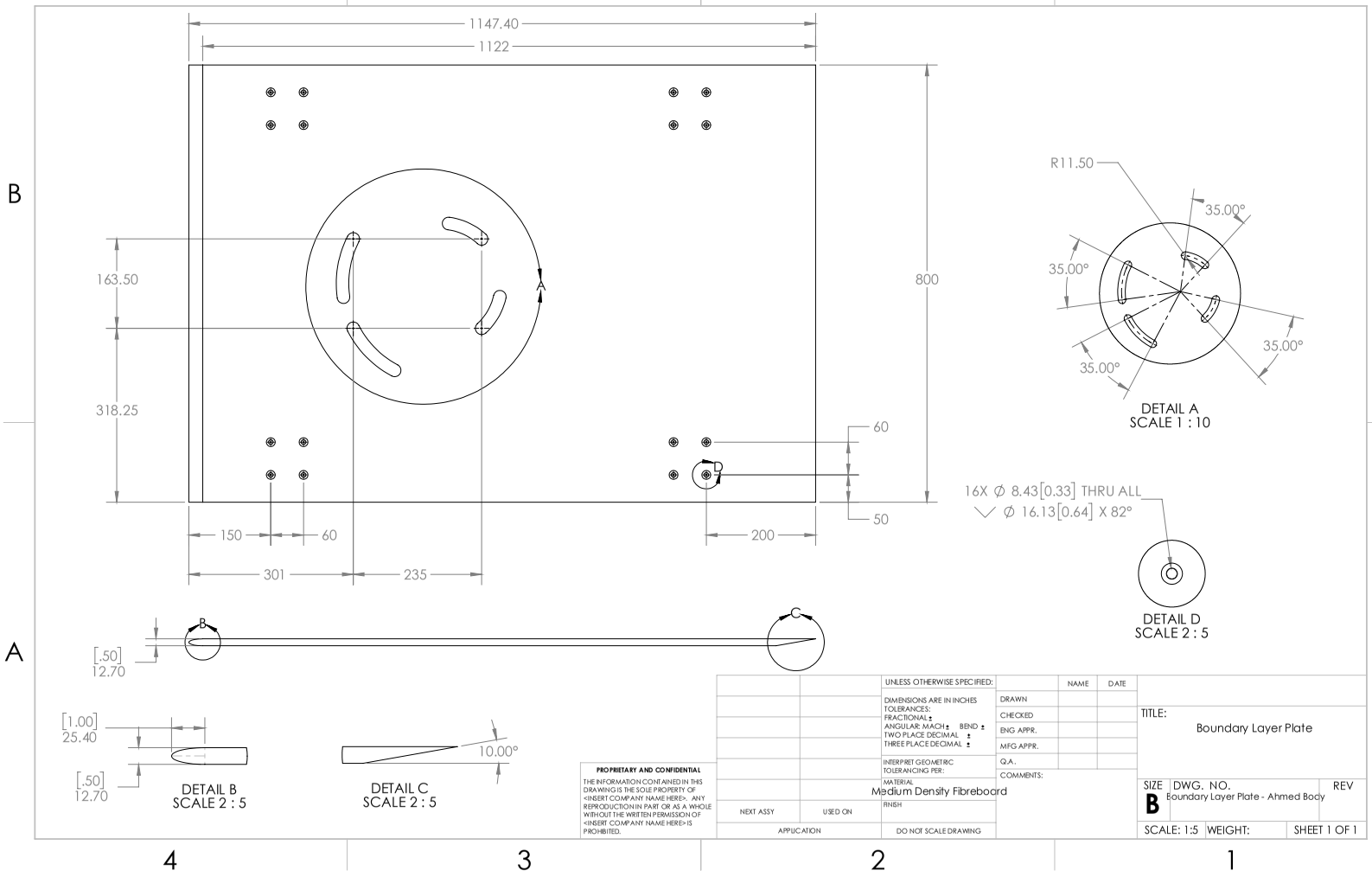
4
3
2
1
B
A
1147.40
1122
800
163.50
318.25
150
60
301
235
200
60
50
R11.50
35.00°
35.00°
35.00°
35.00°
DETAIL A
SCALE 1 : 10
16X ∅ 8.43[0.33] THRU ALL
⌵ ∅ 16.13[0.64] X 82°
DETAIL D
SCALE 2 : 5
[.50]
12.70
[1.00]
25.40
[.50]
12.70
DETAIL B
SCALE 2 : 5
10.00°
DETAIL C
SCALE 2 : 5
PROPRIETARY AND CONFIDENTIAL
THE INFORMATION CONTAINED IN THIS DRAWING IS THE SOLE PROPERTY OF <INSERT COMPANY NAME HERE>. ANY REPRODUCTION IN PART OR AS A WHOLE WITHOUT THE WRITTEN PERMISSION OF <INSERT COMPANY NAME HERE> IS PROHIBITED.
UNLESS OTHERWISE SPECIFIED:
DIMENSIONS ARE IN INCHES
TOLERANCES:
FRACTIONAL ±
ANGULAR: MACH ± BEND ±
TWO PLACE DECIMAL ±
THREE PLACE DECIMAL ±
INTERPRET GEOMETRIC TOLERANCING PER:
MATERIAL
Medium Density Fibreboard
FINISH
NEXT ASSY
USED ON
APPLICATION
DO NOT SCALE DRAWING
NAME
DATE
DRAWN
CHECKED
ENG APPR.
MFG APPR.
Q.A.
COMMENTS:
TITLE:
Boundary Layer Plate
SIZE
B
DWG. NO.
Boundary Layer Plate - Ahmed Body
REV
SCALE: 1:5
WEIGHT:
SHEET 1 OF 1

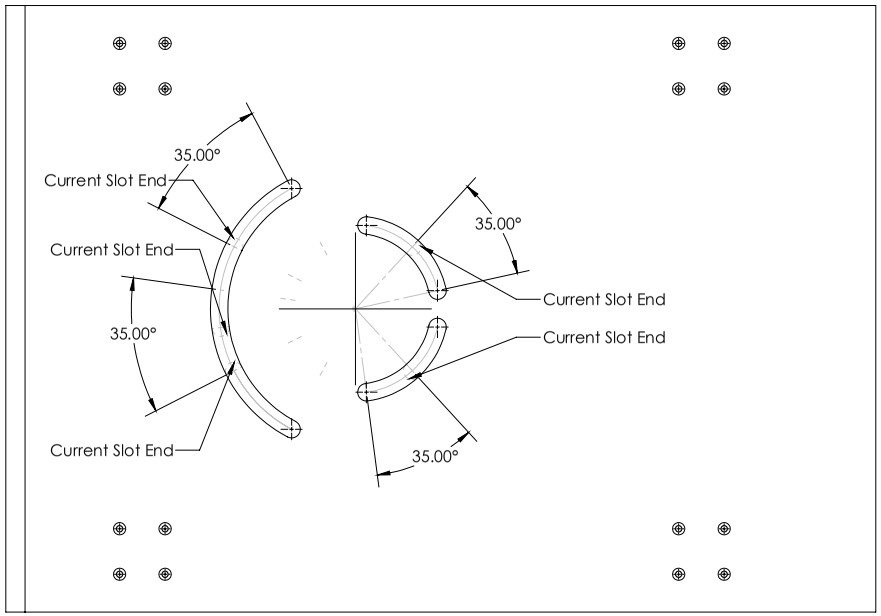

Enlarge slots in opposite direction by the same amount. Premade template for slots will be provided.

		UNLESS OTHERWISE SPECIFIED:		NAME	DATE
		DIMENSIONS ARE IN INCHES TOLERANCES: FRACTIONAL ± ANGULAR: MACH ± BEND ± TWO PLACE DECIMAL ± THREE PLACE DECIMAL ±	DRAWN		
			CHECKED		
			ENG APPR.		
			MFG APPR.		
		INTERPRET GEOMETRIC TOLERANCING PER:	Q.A.		
		MATERIAL Medium Density Fibreboard	COMMENTS:		
NEXT ASSY	USED ON	FINISH			
APPLICATION		DO NOT SCALE DRAWING			

TITLE:
Boundary Layer Plate
V2- Ahmed Body

SIZE	DWG. NO.	REV
B		
SCALE: 1:10	WEIGHT:	SHEET 1 OF 1

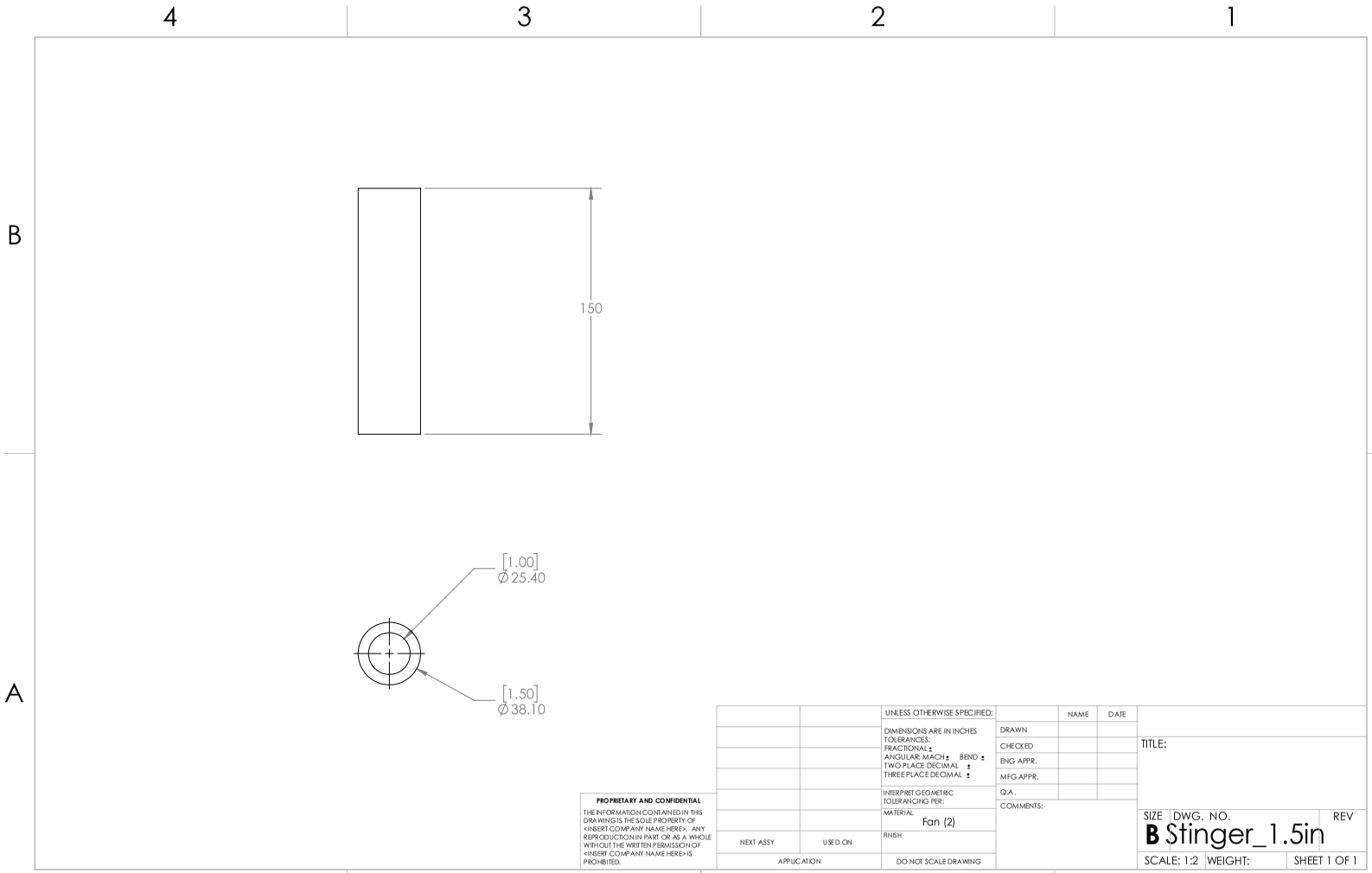
4
3
2
1
B
A
150
[1.00]
Ø25.40
[1.50]
Ø38.10
PROPRIETARY AND CONFIDENTIAL
THE INFORMATION CONTAINED IN THIS DRAWING IS THE SOLE PROPERTY OF <INSERT COMPANY NAME HERE>. ANY REPRODUCTION IN PART OR AS A WHOLE WITHOUT THE WRITTEN PERMISSION OF <INSERT COMPANY NAME HERE> IS PROHIBITED.
UNLESS OTHERWISE SPECIFIED:
DIMENSIONS ARE IN INCHES
TOLERANCES:
FRACTIONAL ±
ANGULAR: MACH ± BEND ±
TWO PLACE DECIMAL ±
THREE PLACE DECIMAL ±
INTERPRET GEOMETRIC TOLERANCING PER:
MATERIAL
Fan (2)
FINISH
NEXT ASSY
USED ON
APPLICATION
DO NOT SCALE DRAWING
NAME
DATE
DRAWN
CHECKED
ENG APPR.
MFG APPR.
Q.A.
COMMENTS:
TITLE:
SIZE
DWG. NO.
REV
B Stinger_1.5in
SCALE: 1:2
WEIGHT:
SHEET 1 OF 1

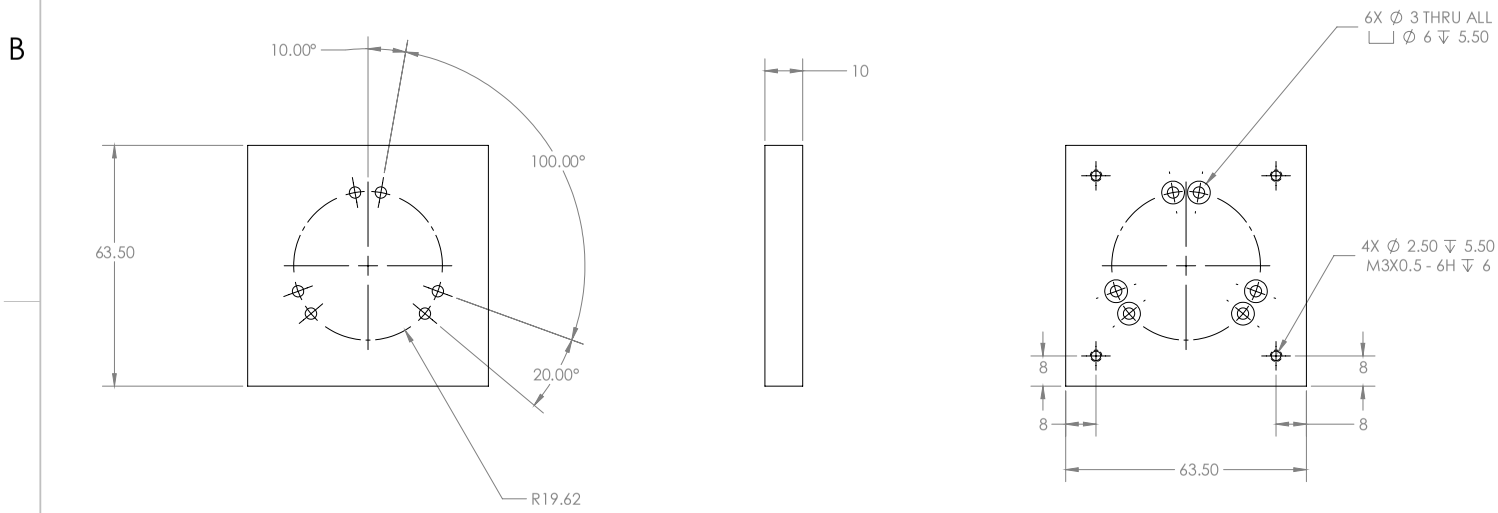

		UNLESS OTHERWISE SPECIFIED:		NAME	DATE
		DIMENSIONS ARE IN INCHES TOLERANCES: FRACTIONAL ± ANGULAR: MACH ± BEND ± TWO PLACE DECIMAL ± THREE PLACE DECIMAL ±	DRAWN		
			CHECKED		
			ENG APPR.		
			MFG APPR.		
		INTERPRET GEOMETRIC TOLERANCING PER:	Q.A.		
		MATERIAL 6061 Alloy	COMMENTS:		
NEXT ASSY	USED ON	FINISH			
APPLICATION		DO NOT SCALE DRAWING			

TITLE: Load Cell Connection Plate

SIZE	DWG. NO.	REV
B	ConnectionPlate	

SCALE: 1:1 | WEIGHT: | SHEET 1 OF 1

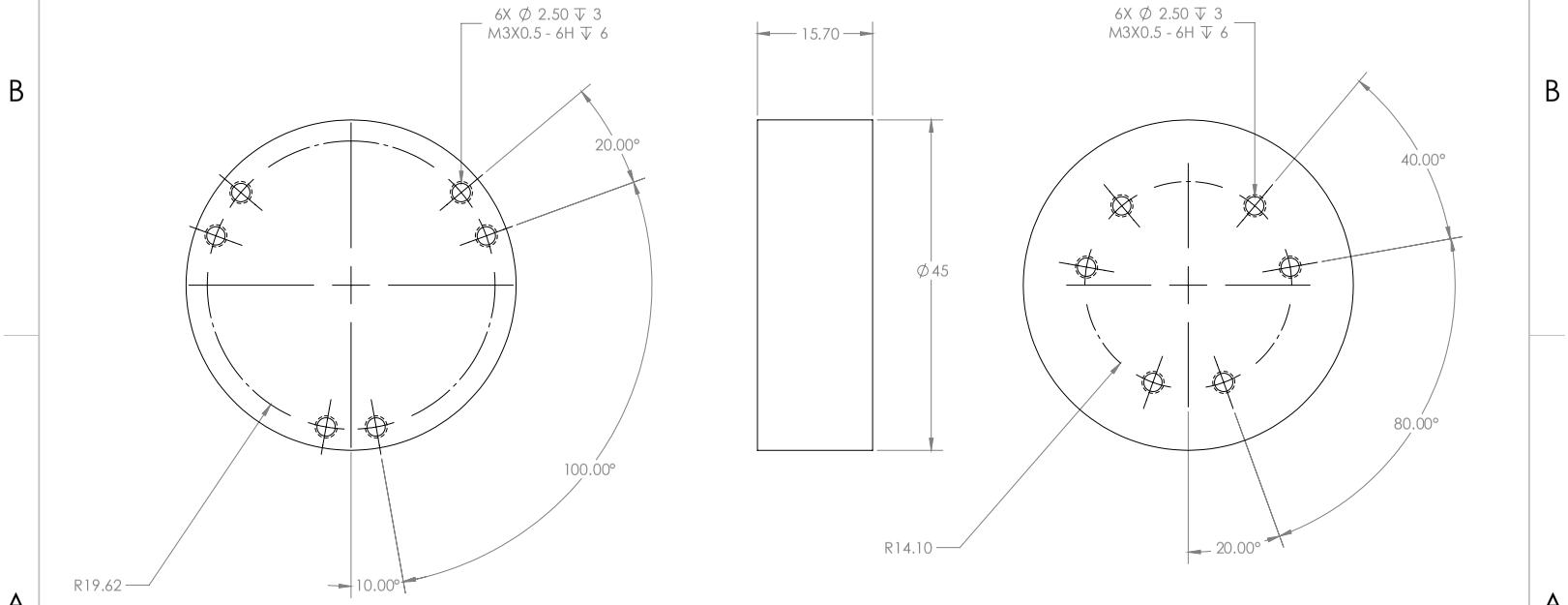

				NAME	DATE
		UNLESS OTHERWISE SPECIFIED:	DRAWN		
		DIMENSIONS ARE IN INCHES TOLERANCES: FRACTIONAL ± ANGULAR: MACH ± BEND ± TWO PLACE DECIMAL ± THREE PLACE DECIMAL ±	CHECKED		
			ENG APPR.		
			MFG APPR.		
		INTERPRET GEOMETRIC TOLERANCING PER:	Q.A.		
		MATERIAL Aluminum	COMMENTS:		
NEXT ASSY	USED ON	FINISH			
APPLICATION		DO NOT SCALE DRAWING			

TITLE: Mini 45 Loadcell

SIZE	DWG. NO.	REV
B	Mini45	

SCALE: 2:1	WEIGHT:	SHEET 1 OF 1

B2. Assembly Dimensions

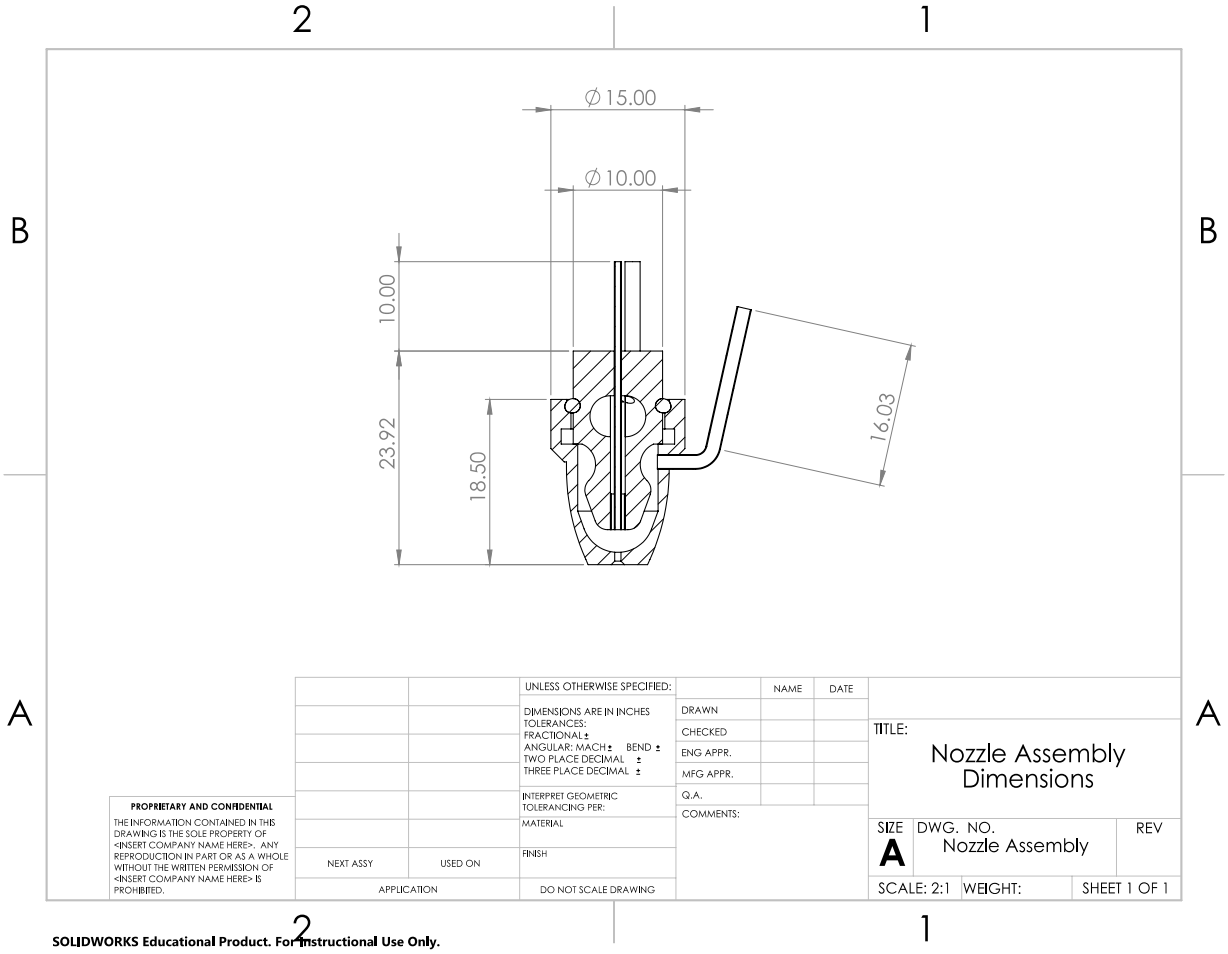

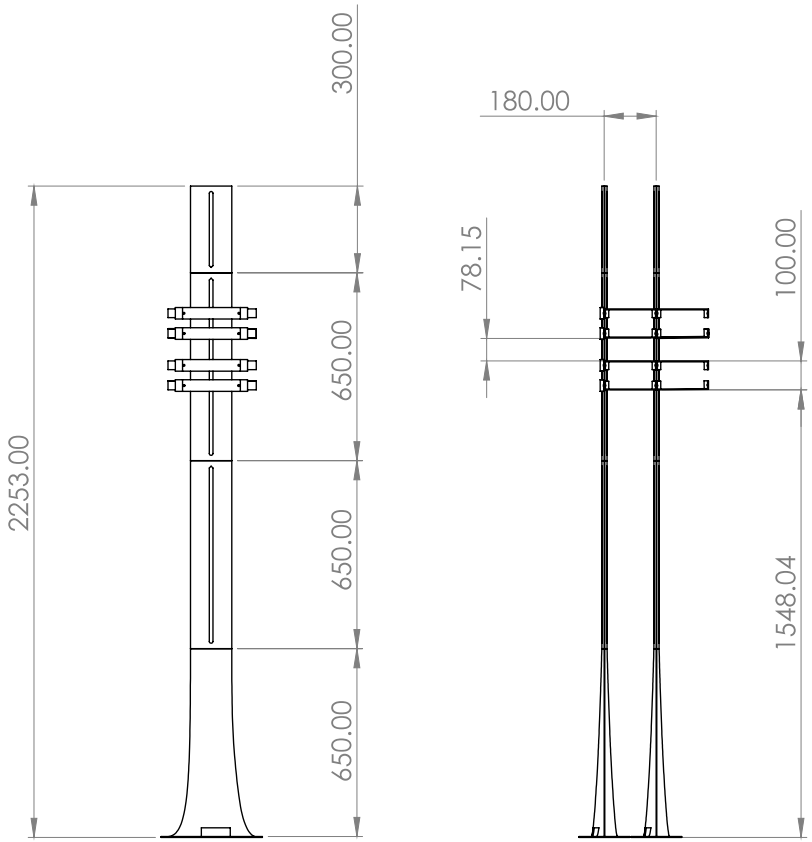

		DIMENSIONS ARE IN INCHES TOLERANCES: FRACTIONAL ± ANGULAR: MACH ± BEND ± TWO PLACE DECIMAL ± THREE PLACE DECIMAL ±		NAME	DATE
			DRAWN		
			CHECKED		
			ENG APPR.		
			MFG APPR.		
		MATERIAL	Q.A.		
			COMMENTS:		
NEXT ASSY	USED ON	FINISH			
APPLICATION		DO NOT SCALE DRAWING			

PROPRIETARY AND CONFIDENTIAL

THE INFORMATION CONTAINED IN THIS DRAWING IS THE SOLE PROPERTY OF <COMPANY NAME >. ANY REPRODUCTION IN PART OR AS A WHOLE WITHOUT THE WRITTEN PERMISSION OF <COMPANY NAME> IS PROHIBITED.

Stand Assembly Dimensions

SIZE	DWG. NO.	REV.
A	Stand Assembly	
SCALE:1:20	WEIGHT:	SHEET 1 OF 1

B3. Passive Control Device Drawings

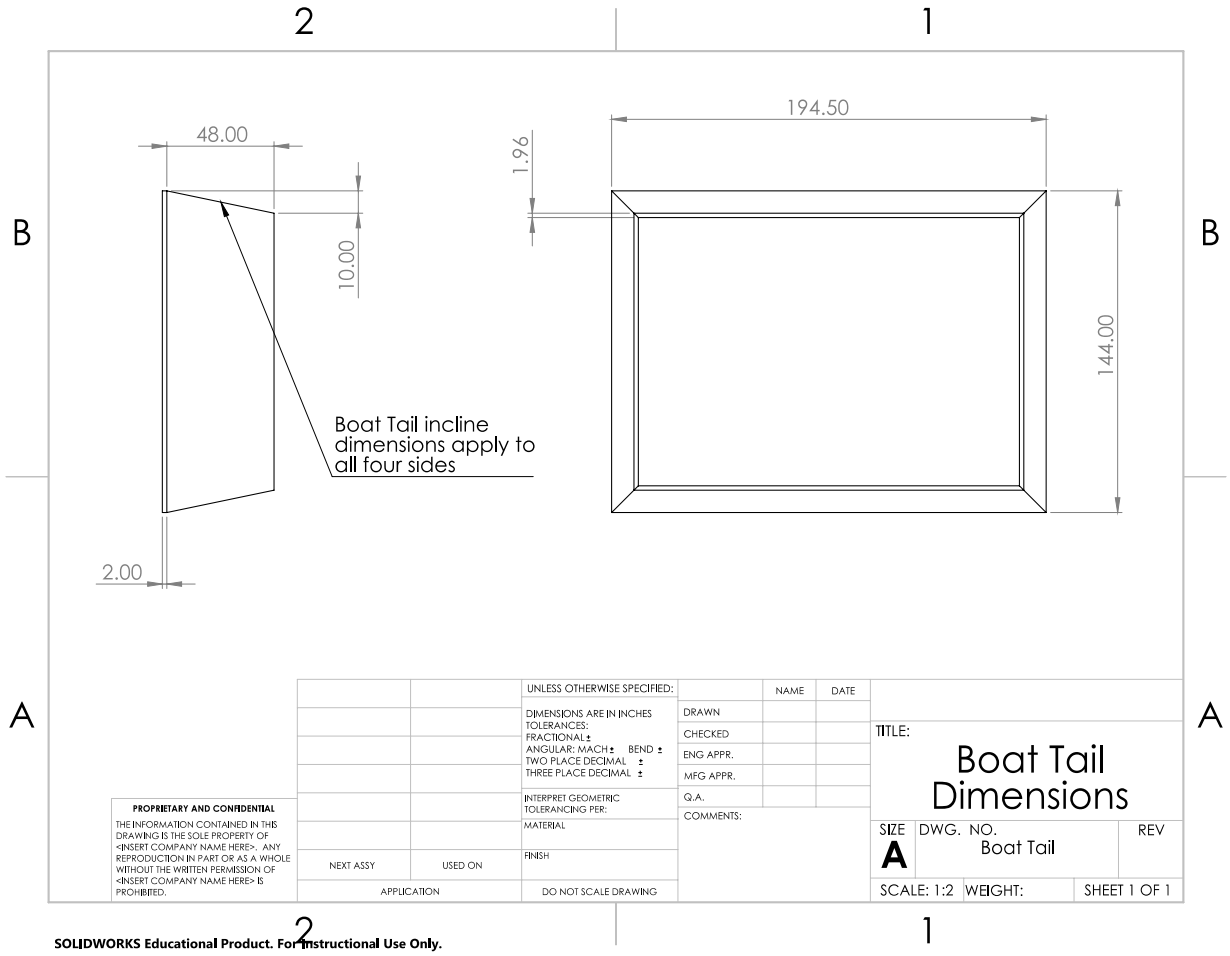

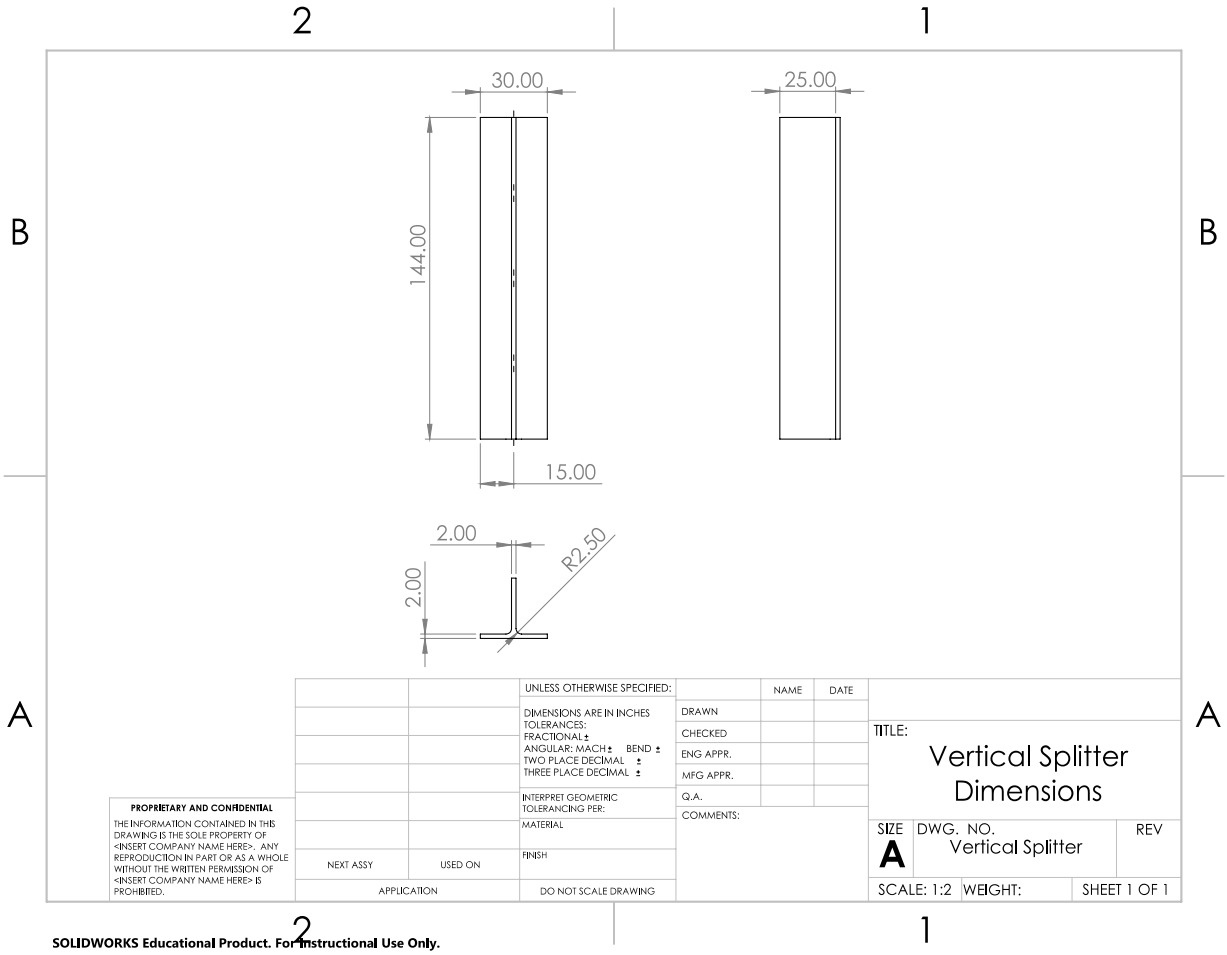

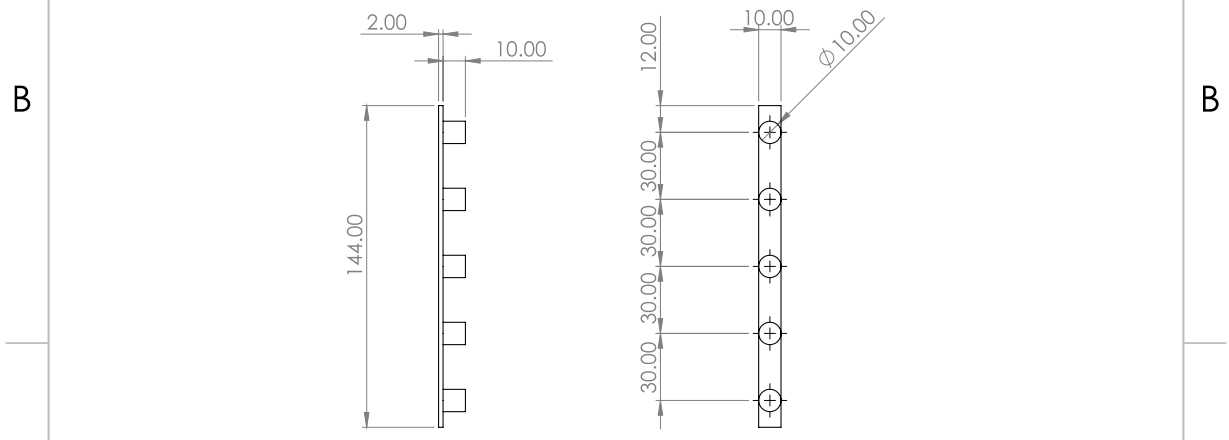

		UNLESS OTHERWISE SPECIFIED:		NAME	DATE
		DIMENSIONS ARE IN INCHES TOLERANCES: FRACTIONAL ± ANGULAR: MACH ± BEND ± TWO PLACE DECIMAL ± THREE PLACE DECIMAL ±	DRAWN		
			CHECKED		
			ENG APPR.		
			MFG APPR.		
		INTERPRET GEOMETRIC TOLERANCING PER:	Q.A.		
		MATERIAL	COMMENTS:		
NEXT ASSY	USED ON	FINISH			
APPLICATION		DO NOT SCALE DRAWING			

PROPRIETARY AND CONFIDENTIAL

THE INFORMATION CONTAINED IN THIS DRAWING IS THE SOLE PROPERTY OF <INSERT COMPANY NAME HERE>. ANY REPRODUCTION IN PART OR AS A WHOLE WITHOUT THE WRITTEN PERMISSION OF <INSERT COMPANY NAME HERE> IS PROHIBITED.

TITLE: Cylinder Rake Dimensions

SIZE	DWG. NO.	REV
A	Cylinder Device	

SCALE: 1:2 | WEIGHT: | SHEET 1 OF 1